Thermal and hydrodynamic effects of nanosecond discharges in air and application to plasma-assisted combustion

Da Xu

THÈSE

Présentée par

Da XU

Pour l'obtention du

GRADE DE DOCTEUR

Formation doctorale: Énergétique
Laboratoire d'accueil: Laboratoire d'Energétique Moléculaire et Macroscopique, Combustion (EM2C) du CNRS et de l'Ecole Centrale Paris

Thermal and Hydrodynamic Effects of Nanosecond Discharges in Air and Application to Plasma-Assisted Combustion

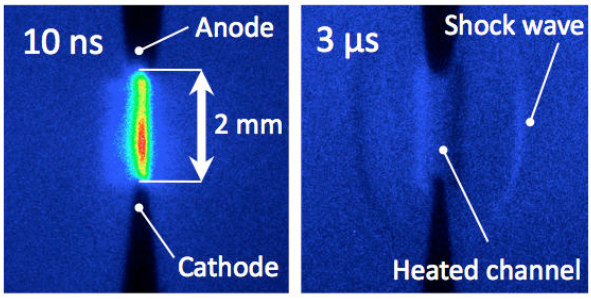

Thèse soutenue le 19 décembre 2013

Jury :

M	Christophe	LAUX	Ecole Centrale Paris, *Professeur*	Directeur de thèse
Mme	Deanna	LACOSTE	EM2C - CNRS, *Ingénieur de Recherche*	Co-Directrice
Mme	Armelle	CESSOU	CORIA - CNRS, *Directrice de Recherche*	Rapporteur
M	Sergey	PANCHESHNYI	ABB Switzerland, *Directeur de Recherche*	Rapporteur
M	Marc	BELLENOUE	ENSMA, *Professeur*	Examinateur
M	Gilles	BRUNEAUX	IFPEN, *Ingénieur de Recherche*	Examinateur
M	Paul-Quentin	ELIAS	ONERA, *Ingénieur de Recherche*	Examinateur
M	Yiguang	JU	Princeton University, *Professeur*	Examinateur

Laboratoire d'Energétique Moléculaire et Macroscopique, Combustion (EM2C)
UPR 288, CNRS et Ecole Centrale Paris
Tél: +33 (0)1 41 13 10 31
Télécopie: +33 (0)1 47 02 80 35

Ecole Centrale des Arts et Manufactures
Grand Etablissement sous tutelle
du Ministère de l'Education Nationale
Grande Voie des Vignes
92295 CHATENAY-MALABRY Cedex
Tél: +33 (0)1 41 13 10 00
Télex: 634 991 F EC PARIS

Abstract

Nanosecond repetitively pulsed (NRP) discharges are being increasingly used in various applications, in particular in plasma-assisted combustion and aerodynamic flow control, because they produce highly reactive atmospheric pressure plasmas with low energy consumption. Coupled with the chemical activations, thermal and hydrodynamic expansions usually occur. For instance, NRP discharges created in a high reduced electric field, are reported to heat the gas rapidly (< 100 ns) through the dissociative quenching of electronic states of N_2 by molecular oxygen. The resulting fast chemical, thermal, and hydrodynamic effects are of great interest for these applications, and are therefore the object of this thesis.

In the first part of the thesis, we present quantitative schlieren measurements and numerical analyses of the thermal and hydrodynamic effects of a NRP discharge in atmospheric pressure air at 300 and 1000 K. The electrical energy of each pulse is of the order of 1 mJ. We analyze single-shot schlieren images recorded from 50 nanoseconds to 3 microseconds after the discharge. The time-resolved images show the shock-wave propagation and the expansion of the heated gas channel. Gas density profiles simulated in 1-D cylindrical coordinates are used to reconstruct numerical schlieren images for comparison with experimental ones. We propose an original method to determine the initial gas temperature and the fraction of energy transferred into fast gas heating, using a comparison of the contrast profiles obtained from experimental and numerical schlieren images. Other basic parameters, i.e. the density, temperature and pressure evolutions following a NRP discharge, can then be obtained from the 1D model. The results show that a significant fraction of the electric energy is converted into gas heating within a few tens of ns. The values range from about 25% at a reduced electric field of 164 Td to about 75% at 270 Td, in agreement with theoretical values reported in the literature.

Second, we provide a database to test the kinetic modeling of lean mixture ignition by NRP discharges. To this end, we use a lean propane/air mixture at pressure up to 10 bar and equivalence ratio 0.7. We characterize the initial spark radius, the ignition kernel development as a function of pressure (up to 10 bar) and the pulse energy (1-6 mJ per pule). A parametric study is then conducted to determine the effects of the Pulse Repetition Frequency (PRF) and the Number of Pulses (NoP) on lean mixture ignition. The results show that applying NRP discharges with higher PRF or greater NoP reduces the minimum ignition energy (MIE) and the ignition delay. Comparisons with a conventional igniter show that better results are obtained with NRP discharges in terms of flame propagation speed, in particular at high pressure, due to the increased wrinkling of the flame front that is induced by NRP discharges.

Finally, we investigate the dynamic response of a flame to actuation by NRP discharges. The flame is produced in a 12-kW bluff-body stabilized burner called the

Mini-PAC burner. The equivalence ratio of premixed propane/air is fixed at 0.8. The NRP discharges are placed in the recirculation zone created by the bluff-body. The results show a significant reduction in lift-off height after applying the NRP discharges. This transition occurs within 5 ms of plasma initiation. Taking into account the thermal, chemical and hydrodynamic effects of NRP discharges, an explanation for the reduction in lift-off height and the associated time scale is proposed. The dominant chemical effect is attributed to the entrainment of OH radicals produced by the NPR discharges toward the shear layer of incoming fresh gases. Thus, NRP discharges provide a promising way to control combustion instabilities, thanks to their ability to rapidly modify the anchoring of a flame, i.e. within a few ms after discharge initiation. This opens up new applications in the control of combustion instabilities. The next step would be to confirm these results for higher Reynolds number flows and high-pressure combustion.

Remerciements

Je tiens tout d'abord à remercier Prof. Christophe Laux, pour ses qualités de pédagogie, d'écoute et sa grande personnalité scientifique. Il a été mon tuteur pendant mes études d'ingénieur, et mon directeur de thèse pendant ces trois dernières années, et sera toujours un mentor, un père pour moi dans la vie. Je remercie également ma co-directrice de thèse, Deanna Lacoste, pour son conseil, son expertise en techniques expérimentales, et pour son amitié, sans lesquelles ce travail n'aurait pu être possible.

Je remercie les membres du jury de thèse: Prof. Marc Bellenoue, qui a présidé ce jury, Drs. Armelle Cessou et Sergey Pancheshnyi, pour les rapports de thèse, et également Prof. Yiguang Ju et Dr. Gilles Bruneaux pour avoir accepté d'être membres du jury. Un énorme merci à Dr. Paul-Quentin Elias, pour avoir suivi ce travail et pour son aide sur le montage expérimental de schlieren.

J'ai apprécié la convivialité et l'amitié de toutes les personnes du laboratoire EM2C. Particulièrement Dr. Daniel Durox pour son expertise d'alignement de schlieren, Diane Rusterholtz-Duval pour son expertise en mesures électriques, son extrême patience et son amitié, Florent Sainct pour son aide et son humour, Anne Bourdon pour son amitié, Yannic Le Teno et Erika Jean-Bart pour leur aide précieuse... Je voudrais également remercier les personnes à l'extérieur du laboratoire, Dr. Mikhail Shneider pour son code de calcul hydrodynamique et nos nombreux échanges, Dr. Guillaume Pilla pour m'avoir accueilli à l'IFP-Energies Nouvelles dans le cadre du projet ANR. Je dois un grand merci à Pascal Bernaud, Barbara Simon et Marc Zolver, qui m'ont beaucoup aidé à obtenir un financement pour cette thèse.

Enfin, je ne saurai exprimer assez de gratitude à mes parents pour leur soutien et leur encouragement permanent tout au long de ces années, et puis à ma femme pour son sacrifice et son constant soutien pendant ces trois années.

Cette thèse a été financée par une bourse doctorale de la Commission européenne "Erasmus Mundus Tandem Programme" et par l'Agence Nationale de la Recherche dans le cadre des projets PREPA (n°ANR-09-BLAN-0043), PLASMAFLAME (n°ANR-11-BS09-025-01) et FAMAC (n°ANR-12-VPTT-0002). De plus, une bourse complémentaire de Centrale Recherche S.A., gérée par Campus France, est également appréciée.

Table of Contents

Chapter 1 Introduction

1.1 Motivations

The reduction of pollutant emissions, in particular nitrogen oxides (NOx), has become a major issue in the design of aeronautical engines, industrial burners or automotive engines. Faced today with increasingly stringent emission regulations, manufacturers have to continually develop and optimize the combustion technology. One path to reduce NOx emissions is to reduce the temperature of the flame, because NOx emissions increase exponentially with the temperature. Reduction of the flame temperature can be achieved by decreasing the fuel-air ratio, and thus lean combustion strategies are used to reduce these pollutants [1]. However, lean flames tend to be unstable or difficult to ignite.

In the automotive manufacturing industry, several new lean combustion engine concepts have been explored in recent years to achieve the ultimate goal of pollution reduction. For gasoline engines, developments have focused on 1) lean premixed combustion, and 2) dilution of stoichiometric mixtures by exhausted gas recirculation (EGR). These technologies are capable of achieving very low NOx emissions. However the use of lean premixed mixtures and/or high level of EGR tends to be limited by poor combustion stability and slow reaction rates (reduced flame speed), resulting in incomplete combustion. The difficulty consists in ensuring reliable spark ignition and flame propagation in lean mixtures.

To go beyond these limitations, the use of an innovative plasma technology might provide the breakthrough needed to ensure the performance of such spark-ignited lean combustion systems. Pulsed, repetitive, nanosecond discharges may have the potential to improve the performance of such combustion systems. It has already been reported that nanosecond discharges enable the stabilization of lean flames with a plasma power less than 1% of the power released by the flame [2], and efficiently ignite lean mixtures up to 2.5 bar [3], thanks to combined thermal and chemical effects.

Another example is the stabilization of subsonic flames for aerospace or gas turbine combustion chambers, as will be discussed in Section 2.4.2. In addition, the use of plasma may be of significant benefit for the ignition and stabilization of flames in supersonic combustors. At high Mach number (typically Mach 2 at 400-1000 K and 0.5-2 bar), the residence time in the combustion chamber is about several μs, less than the auto-ignition delay time of a hydrocarbon/air mixture (on the order of tens of ms at 600-1200 K and 1 bar [4]). The use of plasma is reported to reduce the ignition delay time to tens of μs thanks to the dissociation of the molecules which produces abundant active radicals (O, H) [4].

For all these applications, it has been successfully demonstrated in the past ten years that the use of plasma is a promising way to aid the combustion. In the mean time, great efforts have been made to understand the key mechanisms of plasma-assisted combustion. Depending on the type of discharge used to create plasma, the flame can be influenced by several possible mechanisms of a thermal, chemical or hydrodynamic nature. The chemical and thermal mechanisms of plasma actuation are largely governed by the reduced electric field, E/N, where E is the electric field and N the total gas density. We currently know that:

- At low reduced electric fields (E/N < 100 Td, 1 Td = 10^{-17} Vcm^2 at 300 K), the deposited energy of the discharge is mainly spent on rotational and vibrational states of neutral particles. Under such conditions, the flame is enhanced mainly through O_3 or electronically excited oxygen $O_2(a^1\Delta_g)$ [5].
- At high reduced electric fields (E/N > 100 Td), the discharge energy is mainly spent on electronic excitation, direct electron impact dissociation and ionization. Abundant atomic oxygen can thus be produced through direct dissociation and dissociative quenching of electronically exited states of N_2, and this has been demonstrated experimentally [6-8]. Under such conditions, atomic oxygen plays a key role in combustion enhancement.

Despite the successful experimental demonstrations and kinetic analyses, a detailed understanding of the fundamental mechanisms of plasma-assisted ignition/combustion is still lacking. The remaining questions are, in particular:

- Although the chemical effects of the discharges have been extensively investigated, other combined effects, e.g. thermal and hydrodynamic effects, have not been examined in detail. These mechanisms are strongly coupled with the kinetic reactions. For instance, the dissociation of O_2 molecules via the dissociative quenching of $N_2(B)$ and $N_2(C)$ produces ultrafast heating in less than 50 ns. This heating can be of significant importance for plasma-assisted ignition/combustion.
- The kinetic mechanisms of ignition by non-equilibrium plasma discharges at high pressure are poorly known. Moreover, there is a lack of experimental data on plasma-assisted ignition at high pressure to test kinetic models.
- All previous investigations were made under stationary conditions only. The dynamic response of a flame to plasma actuation is therefore largely unknown.

These questions motivate the present work, in which we first quantified the fast thermal and hydrodynamic effects of nanosecond discharges in air. We used an NRP discharge, which is one of the most energy-efficient ways to produce non-equilibrium air plasmas. In NRP sparks (E/N~200 Td), a significant fraction of energy is deposited into ultrafast heating through the dissociative quenching reactions. Second, we applied the NRP discharges to lean mixture ignition at room temperature and up to 10-bar pressure. Finally, we applied NRP discharges to control flame dynamics, taking advantage of their ability to actuate the flame in a very short time scale.

The objectives of the thesis can be summarized as follows:

- To understand the fast thermal and hydrodynamic effects of NRP discharges in air. To this end, we will quantify the principal parameters, e.g. the initial temperature, the fraction of energy transferred into fast heating, and the density, temperature and pressure evolution following an NRP discharge.
- To better understand the ignition process by NRP discharges, as well as to provide a database for ignition simulations at pressures up to 10 bar. This consists in quantifying the initial NRP spark radius, the ignition kernel development and the flame development.
- To quantify the dynamic response of a flame to NRP discharges' actuation. This may provide a promising way to control combustion instabilities.

1.2 Scope of the thesis

In this thesis, the plasma is created by voltage pulses of amplitude 10 kV, duration 10 ns, applied at a frequency 1-80 kHz between two pin electrodes separated by 0.6, 2, 4 or 5 mm depending on the various experiments conducted. The electric energy of each pulse is of the order of 1 mJ.

In Chapter 2, we provide a review of Nanosecond Repetitively Pulsed (NRP) discharges in air and of the schlieren technique used in this thesis to diagnose NRP discharges. Then, we provide an overview of plasma-assisted combustion with a particular focus on NRP discharges.

In Chapter 3, we present the experimental setups used in this study and the general principles of the experimental techniques. The three experimental facilities used in this work are described.

In Chapter 4, we present quantitative schlieren measurements and numerical analyses of the thermal and hydrodynamic effects of an NRP discharge in atmospheric pressure air at 300 and 1000 K. We recorded single-shot schlieren images starting from 50 nanoseconds to 3 microseconds after the discharge. These experimental schlieren images are analyzed and are compared with numerically generated schlieren images to determine basic parameters such as the initial temperature and the fraction of energy transferred into fast heating.

In Chapter 5, we present detailed investigations of the ignition kernel development as a function of pressure (up to 10 bar) and pulse energy (1-6 mJ per pule). In this study, we used NRP discharges to ignite a lean propane/air mixture of pressure up to 10 bar and equivalence ratio 0.7. Comparisons with a conventional igniter are given.

In Chapter 6, we present an investigation of the dynamic response to NRP discharges of a weakly turbulent premixed flame. The flame was produced in an existing 12-kW bluff-body stabilized burner called the "Mini-PAC" burner. The equivalence ratio of premixed propane/air was fixed at 0.8. Under such conditions, we used CH* chemiluminescence imaging, OH Planar laser-induced fluorescence imaging and optical emission spectroscopy to study the response of the flame after applying the

NRP discharges.

Overall, we studied the dynamics of the NRP discharges with a focus on the thermal and hydrodynamic effects which are important for flame ignition and propagation. We then applied NRP discharges to ignite lean mixtures and to actuate lean flames.

Chapter 2 Background

2.1 Introduction

In this chapter, we first provide a basic knowledge of Nanosecond Repetitively Pulsed (NRP) discharges in air (Section 2.2). Second, since we will develop a schlieren technique to diagnose NRP discharges, this technique applied to plasma discharge study is reviewed (Section 2.3). Finally, we provide an overview of plasma-assisted combustion with a particular focus on NRP discharges (Section 2.4).

2.2 Nanosecond repetitively pulsed (NRP) discharges

2.2.1 Principles, advantages, limitations and applications

Although naturally occurring plasmas are rare on Earth (e.g. a lightning strike or an aurora), people create plasmas to illuminate in neon signs, fluorescent bulbs and television screens, to weld steel structures, and to spark ignite fuel/air mixture in car engines or industrial combustors. Some of these applications require low temperature plasmas, which are commonly referred to as non-thermal plasmas or "cold" plasmas. In these non-thermal plasmas, electrons are "hot", with a temperature of typically several thousand of degrees, whereas ions and neutrals are at a much lower temperature (often close to room temperature. Other applications make use of thermal plasmas, which have electrons, ions and neutrons all in thermal equilibrium with each other (i.e. they are at the same temperature).

Electrical breakdown normally leads to the formation of a spark or an arc discharge, which usually generates a thermal plasma, and thus the gas is heated to a high temperature. This is often a waste of energy for many applications. To improve the energy efficiency of spark discharges, one common way is to control the breakdown process [9-11] by reducing the pulse duration to a few nanoseconds. These so-called nanosecond discharges help prevent the streamer-to-arc transition because the energy is deposited over a duration shorter than the characteristic time for the transition to arc.

Recent technological developments have made it possible to employ nanosecond discharges that are pulsed repetitively at a high frequency (typically greater than 10 kHz). One advantage is that the plasma species produced can then accumulate (10 kHz corresponds to a relaxation time of 100 μs). Such discharges are named Nanosecond Repetitively Pulsed (NRP) discharges. Figure 2.1 shows recent progress in the development of solid state generators according to FID GmbH. This fast development of pulser technology has led to an increase in our ability to generate nonequilibrium plasmas.

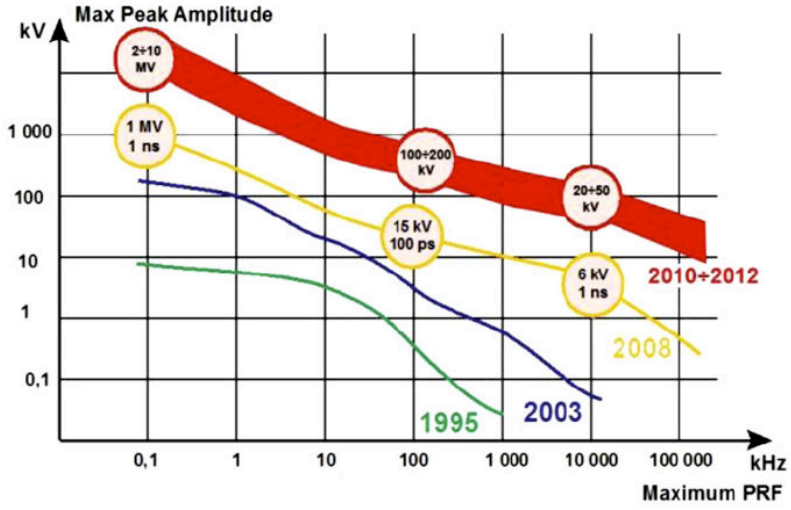

Figure 2.1 Evolution of the voltage and the PRF of NRP discharges. Taken from [12].

The advantage of NRP discharges, which distinguish themselves from single nanosecond pulsed discharges, is the synergetic effect of multiples pulses. It is reported that through the use of high Plasma Repetition Frequency (PRF), active species accumulate and the energy efficiency of ionization increases [13]. In air plasmas, the energy efficiency of discharges can be increased if one can operate at high E/N values without creating an arc. The arc can be avoided if the pulse is sufficiently short, typically of order of nanosecond duration. The increase in energy efficiency can be understood by considering the graph shown in Figure 2.2. At high E/N (typically above 100 Td in air), the fraction of energy deposited into ionization processes increases greatly relative to the fraction of energy deposited into the vibrational excitation of nitrogen molecules.

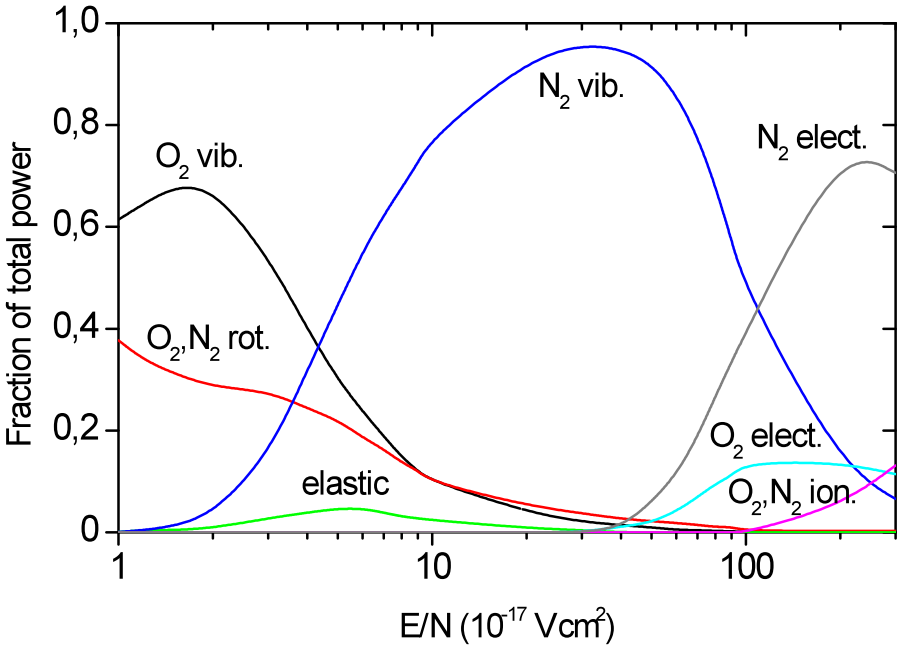

Figure 2.2 Power dissipated into various excitation channels for ambient air. (after Aleksandrov et al [14] and Nighan [15])

Thus, one key advantage of NRP discharges is their high energy efficiency, and thus low power consumption, to produce highly reactive atmospheric pressure air plasmas. For instance, in term of the energy efficiency of producing a high level concentration of radicals for igniting high-speed mixtures, using the conventional DC arc discharge or RF discharge consumes as high as 1 MJ/kg. In contrast, using electron beam or NRP discharges can reduce the energy consumption to only 0.05 MJ/kg [16].

There are usually three regimes of NRP discharges obtained when increasing the voltage applied between the electrodes. These regimes, which are called NRP corona, glow and spark [17] are characterized by different levels of deposited energy, conduction current and gas heating [18, 19]. The NRP corona regime is of less interest because it neither heats the gas nor produces many active species. The NRP glow discharge produces a much larger amount of active species without significantly heating the gas, thus is of great interest for temperature-sensitive applications such as surface treatment or biomedical applications. Its drawbacks are the comparatively low energy per pulse and the difficulty to obtain it in ambient air, although recent work has shown that it can be obtained in ambient air with specific discharge characteristics and electrode geometry [19]. In contrast, NRP spark discharges produce not only abundant active species but also significant heat release, which is particularly interesting for applications in plasma-assisted combustion or flow control. Therefore, in this thesis, we focus our investigations on NRP discharges of the spark type.

Because of their ability to deposit energy with intense power (a typical energy deposition of 1 mJ during 20 ns results in an instantaneous power of 50 kW, which is 500 times higher than for conventional arc discharges), and thus to produce heat and active radicals efficiently, nanosecond discharges or NRP discharges have been increasingly used for various applications, such as plasma-assisted ignition and combustion, nanomaterials synthesis, air pollution control, biomedicine and biochemistry, and aerodynamic flow control [20-25].

However, NRP discharges still have some limitations. First, the often-used pin-pin configuration creates discharges of fairly small dimensions (typically a few cubic millimeters at atmospheric pressure), and therefore is not suitable for the treatment of large volumes of gases. More sophisticated configurations such as electrode arrays should be considered for those applications. Second, high-voltage pulses with short duration generate electromagnetic radiation, which, if not eliminated, may interfere with nearby electronic devices. This second limitation can be circumvented in practical applications through the use of grounding or electrical insulation.

2.2.2 NRP spark discharges in air

Chemical activations

The idea of nanosecond discharges is not new. The nanosecond-pulsed breakdown has been studied for decades, with the last dedicated overview of this field by Korolev et al [26]. Recently, NRP discharges in atmospheric pressure air have been studied experimentally [18, 19] and numerically [27, 28]. A recent review of NRP discharges

can be found in [13].

Great progress has been made in the understanding of the chemical effects of NRP discharges. Among other processes, the rapid dissociation of oxygen molecules (by up to 50% [29]) by NRP discharges has attracted great attention, because atomic oxygen plays an important role in hydrocarbon oxidation processes in combustion, as well as in other applications (e.g. biological decontamination). It has been evidenced that the production of abundant O mainly results from an ultrafast mechanism [29, 30], which corresponds to the following two-step process (see for example Popov [31]):

$$N_2(X) + e^- \rightarrow N_2(A, B, C, a'...) + e^-$$

$$N_2(A, B, C, a', ...) + O_2 \rightarrow N_2(X) + O + O + \text{heat}$$

In the first step, which occurs during the high voltage pulse, nitrogen molecules are excited by electron impact to electronic states such as $A^3\Sigma$, $B^3\Pi$, $C^3\Pi$, $a'^1\Sigma$,... Next, these excited electronic states of N_2 undergo quenching by oxygen molecules, producing atomic oxygen and heat release. The dissociative quenching reactions of N_2 A, B and C occur immediately after the pulse, and proceed very quickly with characteristic times of 108, 0.9, and 0.6 ns respectively (at atmospheric pressure and room temperature). This ultrafast production of O was experimentally verified by Stancu et al [6], who made time-resolved measurements of the densities of O and $N_2(A,B,C)$ using Two-photon Absorption Laser-Induced Fluorescence (TALIF), Optical Emission Spectroscopy (OES) and Cavity Ring-Down Spectroscopy (CRDS). Ultrafast heating was measured by Pai [18] and verified by Rusterholtz [19, 29], who determined the temperature increase from OES measurements of rotational lines of the N_2 first and second positive systems.

Figure 2.3 presents a comparison of experimental and numerical results of the temperature and atomic oxygen evolution. The simulations, which take into account the dissociation of O_2 molecules via dissociative quenching, are in good agreement with the observed temperature and oxygen density profiles. They also show that the dissociation of O_2 molecules occurs mostly via the dissociative quenching of $N_2(B)$ and $N_2(C)$. Moreover, Popov [30] estimates that in this case about 35% of O is produced via direct electron-impact dissociation during the pulse.

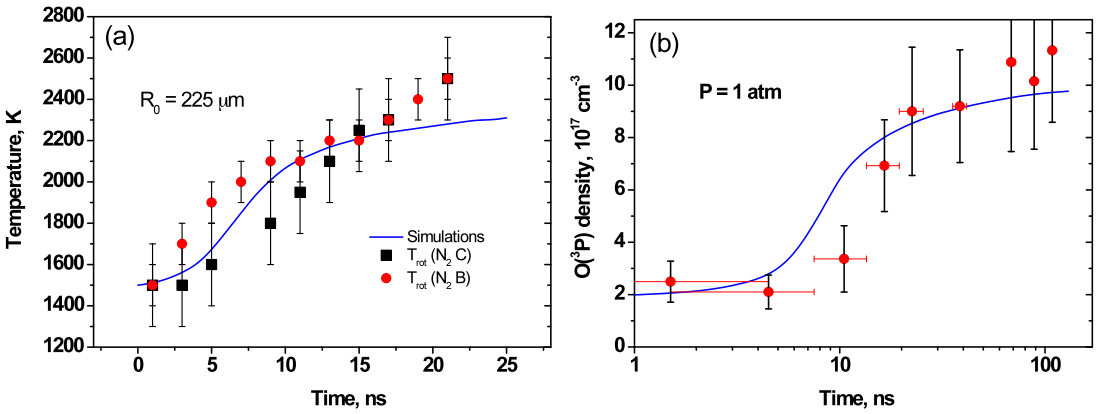

Figure 2.3 Comparison of measured (squares) and simulated (line) temporal evolution of (a) the gas temperature (b) the ground state atomic oxygen density. The experiments were performed by Rusterholtz et al [29]. The simulations were performed by Popov [30]. Taken from Rusterholtz et al [29].

The rapid production of O, through dissociative quenching or direct electron-impact dissociation, should have significant impact on the chain reaction of hydrocarbon oxidization, thus resulting in the production of OH. Note also that the fast dissociation of O_2 via dissociative quenching was also demonstrated by Lo et al [32].

Thermal and hydrodynamic effects

NRP sparks can dissociate a large fraction of oxygen molecules and heat the gas by about 1000 K within a few tens of nanoseconds following each pulse. Accompanying the fast temperature increase, the pressure increases suddenly and pressure waves may emerge from the discharge region and propagate through the surrounding air. The gas density *N* changes slightly within the first 50 ns, for example by about 10% when 50% of oxygen dissociates. Then, when the pressure returns to atmospheric behind the shock wave, the density decreases significantly because of the heating and the hydrodynamic expansion. The ultrafast mechanism described above is reported as strongly dependent on the reduced electric field (E/N) [33]. Thus, it is important to know the evolution of the hydrodynamic parameters (such as density, temperature and pressure) following an NRP discharge.

Many authors [10, 34-38] have investigated the hydrodynamics of sparks in air or fuel-air mixtures, using sparks of longer duration (> 0.5 μs) and greater energy input (> 10 mJ), and they have typically limited their measurements to temporal windows starting from several microseconds following the spark. Reinmann et al [39] extended the investigated time region to as early as 200 ns following the spark. Their simulations, assuming that the heated gas channel had an initial temperature of tens of thousands of Kelvin, successfully described the shock-wave position, the particle number densities and the temperature.

To date, however, the hydrodynamics of NRP sparks have not been examined. The small plasma dimensions, short lifetimes of the shock waves (typically less than a few microseconds), and the weakness of the shock waves produced by NRP discharges with

energy per pulse of about 1 mJ in heated air, make the investigation challenging. Moreover, the classical blast-wave theory [40, 41], which is usually employed to describe strong shock behaviors, does not hold for NRP sparks. The blast-wave theory assumes that: 1) the energy is released in an infinitesimal volume, and 2) the pressure behind the shock wave is much greater than the ambient pressure. In contrast, for NRP sparks, first, the characteristic radius of the shock wave is comparable to the initial heated channel radius. And second, as will be seen later, the pressure behind the shock wave is only about twice the ambient pressure. Thus this theory is not applicable.

Experimental techniques based on light deflection, such as the schlieren technique, have been extensively used by previous authors to visualize the shock wave and heated gas channel generated by spark discharges. In the next section, we present a review of the schlieren technique applied to spark discharges.

2.3 Application of the schlieren technique to spark discharges

The schlieren technique is a commonly used method for the analysis of transparent fields having a cylindrical or spherical distribution of refraction index. Qualitative schlieren imaging applied to spark discharges dates back to a century ago when this technique was developed. Among the numerous studies published, we have chosen to review quantitative schlieren analyses of the spark channel, and some semi-quantitative schlieren measurements of the expansion rate of the shock waves and the heated gas channel produced by sparks.

Four decades ago, Freeman et al [38] measured the radius of the cylindrical shock wave generated by a spark as a function of time, using a schlieren system equipped with a rotating camera. The experiments were done in rare gases and air, for a spark of duration 10 μs, voltage above 26 kV, current above 200 A, and pulse energy about 0.5 J. The measured shock wave expansion was fairly well predicted by the blast-wave theory. They found that the shock wave appeared at about 0.5 μs in air. This delay was greater in rare gases. However, due to the old technology of streak cameras 40 years ago, the hydrodynamic expansion at the very early times ($t < 0.5$ μs) was not very clear.

Haley et al [34] took successive laser schlieren photographs of the expanding flows caused by a spark in atmospheric air or combustible mixture. The spark had a duration of 1 μs, an energy of 30 mJ, and a gap distance of 4 mm. They observed a turbulent vortex after the departure of the shock wave. They argued that those turbulent wake flows were generated by the transition of the initially cylindrical shock wave to a spherical configuration, as supported by the blast-wave theory. They also showed that the turbulence generated was responsible for the increase of combustion rate.

Other authors [10, 35, 37] studied the spark ignition kernel expansion in combustible mixtures, using qualitative or semi-quantitative schlieren imaging. Arpaci [42] reviewed these studies on ignition kernel development and used a similitude method to predict the evolution of the ignition kernel radius.

Quantitative schlieren analyses of arc discharge emerged in the 1970s.

Kogelschatz and Schneider [43] deduced a mathematical formula to easily calculate the deflection angle from a refractive index distribution with cylindrical symmetry. Later, Ono et al [44] used the Kogelschatz and Schneider formula to generate numerical schlieren images from assumed density profiles. With the advent of numerical simulations enabling the determination of density profiles, it became then possible to generate numerical schlieren images that can be directly compared with experimental schlieren images to infer the temperature and density, through an iterative trial-and-error method.

The numerical schlieren method was presented and discussed in the 1980s [45, 46], although the key formulations were pretty much similar to that deduced by Kogelschatz and Schneider.

Apart from the classical schlieren setup, some authors [47] [48] used a narrow laser beam to probe discrete points within the heated channel diameter. Using the measured deflection of the laser beam, it is then possible to calculate the density and the temperature. However, these authors mentioned that the channel diameter should be significantly larger than the probing laser beam. Thus this technique is not well suited for the NRP discharges studied in this thesis because the diameter of our NRP discharges on the order of 0.5 mm, is very close to that of a conventional laser beam.

To conclude this section, quantitative schlieren methods can be applied to investigate the hydrodynamic expansion of NRP discharges. In this thesis, we developed such a technique, which will be presented in Chapter 3. Especially, gas dynamic simulations can be used to generate numerical schlieren images from the computed density profiles in order to determine the key hydrodynamic parameters (temperature, density, and pressure) through a trial-and-error method. This method will be presented in Chapter 4.

2.4 Nanosecond discharges applied to plasma-assisted combustion

One important application of nanosecond discharges is plasma-assisted combustion. Although the principle of spark ignition and auto-ignition has been known and used in the automotive and aerospace industries for a long time, there are different applications where the use of novel plasma discharge systems may be of significant benefit. We can mention in particular ignition in sub and supersonic flows, combustion enhancement and stabilization, ignition of lean or diluted mixtures, etc.

Over the past decade, many experiments and kinetic simulations have demonstrated that plasma discharges can significantly enhance combustion processes, with plasma powers that are much lower than the power released by the flame. The last dedicated review of this field was made by Starikovskiy and Aleksandrov [12], who reviewed practical demonstrations of the effectiveness of plasma-assisted combustion and described the current understanding of the non-equilibrium excitation of combustible mixtures by electrical discharges. In this section, we present some of the remarkable experimental and numerical studies with a particular focus on NRP

discharges.

2.4.1 Plasma-assisted ignition

For spark ignition of hydrocarbon mixtures, it is generally considered that the localized deposition of thermal energy (heat) and chemical energy (molecular dissociation, excitation, and ionization) is very beneficial to initiate the ignition process. Although thermal ignition theories are in fair agreement with experimental values of minimum ignition energies and quenching distances, they do not predict correctly the ignition delay [49] because spark ignition involves a wide range of phenomena, not only thermal. To date no complete ignition theory has been established and the respective roles of thermal and chemical effects are not clear. Westbrook [50] proposed that a temperature of 900 K should be achieved to initiate the chain reaction process for hydrocarbon mixtures. This implied that an ignition system should either provide gas temperatures in excess of 900 K, or produce a sufficient amount of active species as possible, or both. To this end, the NRP discharge described in Section 2.2 can be a highly realistic candidate.

Pancheshnyi et al [3] conducted an experimental study on the ignition of lean propane-air mixtures by a train of 10 nanosecond pulses at pressures up to 2.5 bar. An example of light emission during the ignition and flame propagation is presented in Figure 2.4 by a sequence of images taken with a high speed CCD camera, with an exposure time of 33 μs and a frame rate of 1.5 ms^{-1}. It was shown that by using NRP discharges, the ignition delay was significantly reduced over that with a conventional ignition system. It was also shown that the gas temperature increased up to 3000 K after gas breakdown, and numerous active species (N, N^+, O, O^+) were observed just after the 10-pulse train (300 μs).

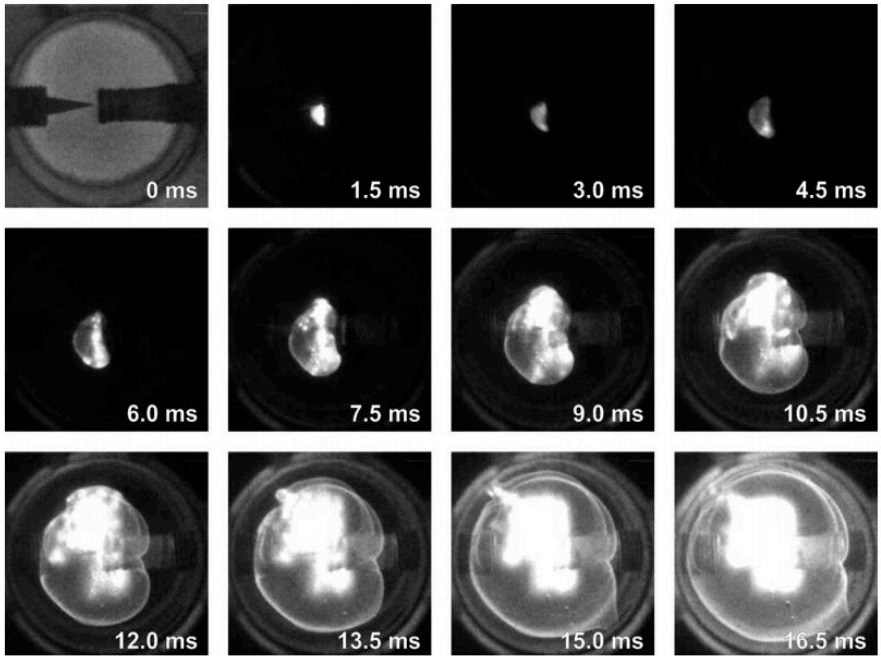

Figure 2.4 Flame propagation in a lean (ϕ=0.7) propane-air mixture ignited at 2 bar by a

train of 10 high voltage pulses spaced by 33 µs. The inter electrode gap distance is 1.5 mm and the energy per pulse is 1 mJ. Taken from [3].

Kosarev et al [51] studied experimentally and numerically the kinetics of ignition in C_nH_{2n+2}:O_2 diluted in argon for n=2-5 by a high-voltage nanosecond discharge. The mixtures were heated by a shock wave with a temperature of about 1400-2000 K in the shock-wave front. The auto-ignition delay times were measured with and without the presence of nanosecond discharges. It was shown that the application of the gas discharge led to an order of magnitude decrease in the ignition delay time. The analysis of simulation results showed that the plasma favors the ignition mainly due to O atoms produced by the discharge. In this analysis, however, gas heating effects were not considered.

Yin et al [52] measured the evolutions of the absolute OH concentration and temperature during ignition of H_2-air mixtures by NRP discharges. They observed both a significant OH density and temperature rise at the end of the pulse burst, corresponding to a decrease of the autoignition delay time. Kinetic simulations demonstrated that, first, H and O atoms were generated by NRP discharges through electron-impact dissociation and dissociative quenching of electronically excited N_2. Next, OH accumulated through chain reactions: $H+O_2 \rightarrow O+OH$ and $O+H_2 \rightarrow H+OH$. Therefore, O atoms play an important role in the initiation of combustion.

In the field of supersonic ignition, Leonov et al [53] reviewed experiments in plasma-assisted ignition/combustion of high-speed flows. In that paper, electrical discharges are considered as one of the most promising technologies for scramjet engine ignition, thanks to fast local heating and active species generation. In their experiments, they used multi-electrode arc discharges in the flow separation zone above a wall cavity. They observed that the discharges not only led to a temperature rise by 3000 K and consequently a pressure increase in the cavity, but also generated abundant atomic oxygen, which is important for the combustion chemistry. Under these combined effects, the hydrogen injected in the high speed flow was ignited.

2.4.2 Flame enhancement

NRP discharges have been shown to significantly reduce the lean blow-off limit of diffusion flames [7, 54, 55], stabilize and reduce the lean extinction limit of premixed flames [2, 56-58], and accelerate flame propagation [5].

In Ref [56], a NRP discharge produced by electric pulses of 10 kV during 10 ns at a frequency of up to 30 kHz has been used to stabilize a 12-kW lean turbulent premixed propane/air flame (Re_D = 30 000) at atmospheric pressure. It was shown that, when placed in the recirculation zone of the flow (Figure 2.5a), the plasma significantly increases the heat release, thus allowing to stabilize the flame under lean conditions where it would not exist without plasma. Stabilization was obtained with a very low level of plasma power of about 75 W, or 0.6% of the power released by the flame. In addition, they found that at high flow rates, where the flame should normally blow out,

the NRP discharges allowed the existence of an intermittent V-shaped flame with significant heat release, and at even higher flow rates the existence of a small dome-shaped flame confined near the electrodes that can serve as a pilot flame to reignite the combustor.

In Figure 2.5b, the domain of stability of the V-shaped flame without plasma is shown by region 1. Region 2 represents the extended domain of stability of the V-shaped flame when the plasma is applied. Region 3 corresponds to a regime of intermittent flame, still with a relatively high level of heat release. Region 4 corresponds to the domain of the pilot flame. The lean blow-off limit was thus significantly reduced, for instance, from Φ=0.75 to lower than 0.65, at a flow rate of 10 m^3/h.

Optical emission spectroscopy measurements were performed to determine the temperature of the plasma-enhanced flame, the electron number density, and to identify the active species produced by the plasma. It was found that NRP discharges produce O, H, and OH.

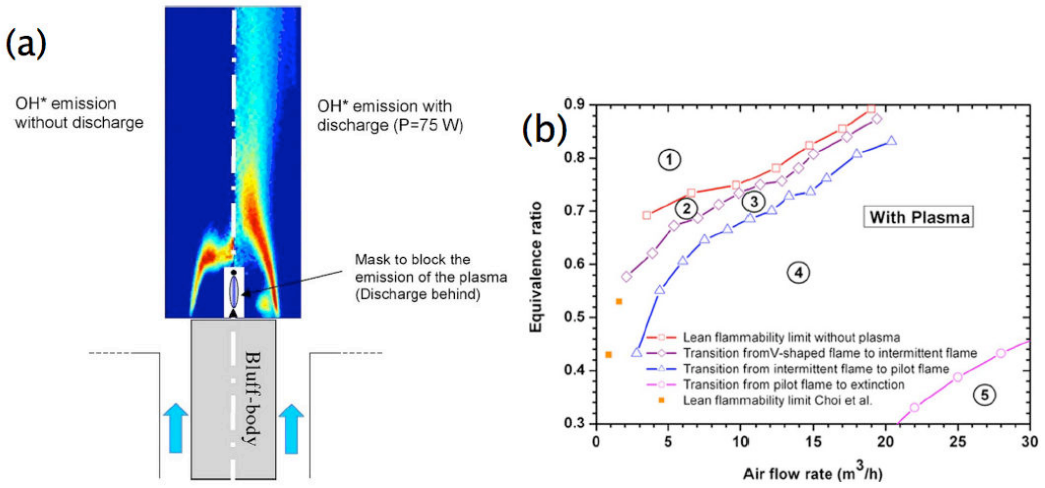

Figure 2.5 (a) Comparison of OH emission with and without discharge (b) burner regimes with plasma. Taken from [56].

Additional experiments were conducted at the EM2C laboratory to extend the studies of bluff-body stabilized flames presented in the previous section. In one study, swirled stabilized flames were investigated using the two-stage swirled injector shown in Figure 2.6 [58]. The NRP discharge was generated between a wire anode placed 1 cm downstream of the outlet of the primary stage mixing zone, and the nozzle was used as the cathode. The pulses were up to 30 kV in amplitude, 10 ns in duration, and the PRF was 30 kHz.

Initially, a stable flame was obtained by injecting propane and air through the primary stage at a fuel equivalence ratio Φ_p = 2.4, and additional air was injected through the secondary stage at a flow rate four times higher than that of the primary stage. The global equivalence ratio in the combustion chamber was thus Φ_g = 0.47. Then, for a constant airflow rate, the global equivalence ratio was decreased until flame

extinction, with and without discharge. The lean extinction limit without discharge was reached for $\Phi_g = 0.41$. With plasma, it was lowered down to $\Phi_g = 0.11$ (with $\Phi_p = 0{:}57$). Thus a considerable extension of the lean extinction limit was obtained, with a discharge power of about 350 W, i.e. 0.7% of the flame power P = 53 kW.

Similar effects were also obtained with a 200-kW turbulent aerodynamic injector working with kerosene/air at 3 bar [59]. In this case, the lean extinction limit was decreased from $\Phi = 0.44$ to $\Phi = 0.21$ using a similar NRP discharge with about 1% of the flame power.

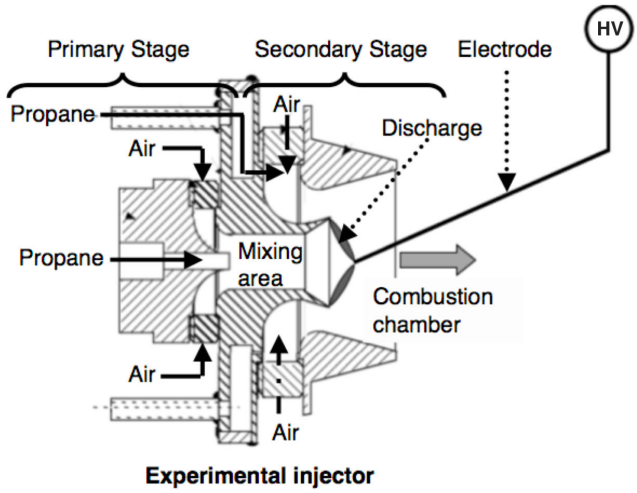

Figure 2.6 Schematic of the two-stage burner and electrode locations.

These studies have shown a significant effect of the plasma on the flame behavior through chemical and thermal activation. These two mechanisms are strongly coupled, and their respective effects on the flame properties have not been clarified yet. Through numerous studies, atomic oxygen has been identified as one of the most important chemical products of the discharge. Chemical models involving atomic oxygen addition have then been proposed for comparison with the experimental data.

Sun et al [7] studied the chemical effects of NRP discharges on the extinction of partially premixed CH_4-air flame in a counterflow configuration at 300 K and 60 Torr. They showed that NRP discharges dramatically accelerate CH_4 oxidation. Their kinetic simulations showed that this was mainly due to the O generation by the NRP discharges.

Ombrello et al [5] studied the chemical effects of O_3 produced by NRP discharges on a laminar flame propagation at 1 bar. They showed an 8% enhancement of the flame propagation speed for a measured O_3 concentration of 1260 ppm. Kinetic simulations showed that the O_3 decomposition and reaction with H produced O and OH, respectively. The O reacted with C_3H_8 and produced additional OH. The subsequent reactions of OH with the fuel fragments, such as CH_2O, provided heat release and enhancement of the flame propagation speed.

2.4.3 Control of combustion dynamics

Very recently, NRP discharges found application in the control of combustion

dynamics.

Combustion instability is a key issue for lean premixed combustion in gas turbines [60]. Instabilities generally occur when the unsteady heat release rate couples with the acoustic modes of the combustor, resulting in detrimental outcomes ranging from unacceptable noise and increased heat transfer to structural failure. This effectively results in a limited operating range [61] with drawbacks in power and efficiency. For these reasons, combustion instabilities are generally undesirable and to be avoided at all cost.

One approach to mitigate these instabilities is based on active control of the system dynamics [62, 63]. However, despite numerous successful demonstrations, the application of these methods in full-scale engines remains scarce. Restrictions in available actuator technology have been identified as one of the key issues responsible for this [63].

NRP discharges have favorable properties with respect to combustion instability control. In addition to low power consumption and a strong effect on the flame, NRP discharges can be modulated at high frequencies because there are no mechanically moving parts. This property is also promising in terms of robustness of the actuator system. Using this type of plasma as an actuator for feedback control applications in combustion systems therefore appears to be a promising approach.

First and foremost, the dynamic response of the flame to the plasma actuation needs to be understood. Indeed, if the flame response is not fast enough, then NRP actuations at high frequencies will have no effects on the flame dynamics. In previous studies, except for ignition studies that aimed to determine the induction time, all previous investigations were made only under stationary conditions. The dynamic response of a flame to NRP discharges is therefore largely unknown. While it is sufficient to study stationary effects in order to assess the capability of NRP discharges to augment static stability limits, alternate applications such as combustion instability control require, in addition, an understanding of the transient processes associated with the interaction of the plasma and the flame. This motivates our studies of the transient behavior of flames after the application of NRP discharges.

2.5 Conclusions

In this chapter, we first provided an overview of Nanosecond Repetitively Pulsed (NRP) discharges in air (Section 2.2). Second, the schlieren technique used to diagnose NRP discharges was reviewed (Section 2.3). Finally, we gave an overview of plasma-assisted combustion applications with a focus on NRP discharges (Section 2.4).

Previous studies have shown that NRP discharges have both thermal and chemical effects, which can be responsible for plasma-enhanced ignition/combustion. The production of atomic oxygen through the dissociative quenching of electronically excited N_2 has been identified as a major factor for flame enhancement, however, the production of O is accompanied by ultrafast heating of the gas. This ultrafast heating

produces thermal and hydrodynamic effects that may also have a significant influence on the flow and on chemical reactions. These effects are largely unknown and need quantification. To this end, the schlieren technique has been identified as a well-suited method for both qualitative and quantitative investigation of the thermal and hydrodynamic effects of NRP discharges.

Chapter 3 Experimental setup

3.1 Introduction

In this chapter, we present the experimental setups used in this study and the general concept of the experimental techniques. Several experiments were performed in three different facilities presented in Section 3.2:

1) the nanosecond discharges in air were generated in a preheated environment (Section 3.2.1).

2) the plasma-assisted ignition experiments were performed in a constant volume chamber (Section 3.2.2).

3) the plasma-assisted combustion dynamics experiments were conducted in the Mini-PAC burner (Section 3.2.3).

Then, in Section 3.3, we present the electric energy measurement method for the above three experiments. Finally, in subsequent sections, we detail the optical diagnostic techniques used in this thesis, including the schlieren technique to visualize the thermal and hydrodynamic expansion of NRP discharges in air or in combustible mixtures, the Planar Laser-Induced Fluorescence (PLIF) technique to detect the OH radicals in flames, the CH* and OH* chemiluminescence imaging to locate the flame front, and finally the Optical Emission Spectroscopy (OES) technique to determine the temperature of the gas.

3.2 Experimental facilities

In this section, we provide descriptions of the three experimental facilities used in the thesis. Three nanosecond pulse generators available in the laboratory were selected to meet the needs of the three experiments. In the preheated air experiment, we focus on the thermal and hydrodynamic effects of NRP discharges, and since the air is preheated, the breakdown voltage is low, thus a 5-kV pulser (FID-1) with moderate power was sufficient to do the job. For ignition studies, a more powerful pulser with 10-kV amplitude (FID-4) was used for low-pressure cases (1-2 bar). For high pressures (3-10 bar), a 15-kV pulser (FID-2) was used. Finally, the pulser (FID-2), which has the widest range of pulse repetition frequencies (PRF), was chosen for the task of plasma-assisted combustion dynamics, to be able to show the influence of the pulse repetition frequency (PRF) on the flame. A summary of the characteristics of the three pulse generators is given in Table 3.1.

Table 3.1 Characteristics of the three pulsers used in the thesis.

Generator designation	**FID-1**	**FID-2**	**FID-3**	**FID-4**
Commercial name	FPG 10-30MS	FPG 30-100MC4K	Not used	FPG 10-30NM10
Impedance	~ 75 ohm	~ 300 ohm		~ 150 ohm
Frequency range	1-30 kHz	1-100 kHz		1-30 kHz
Voltage range	0-10 kV	0-30 kV		0-12 kV
Maximum voltage into a matched impedance	5 kV	15 kV		10 kV
Pulse width at 90% of amplitude	~ 10 ns	~10 ns		~10 ns

3.2.1 NPR discharges in preheated air

The air-plasma generation system (Figure 3.1) has been initially developed by Pai [18] to produce NRP discharges in preheated air at atmospheric pressure. This system and its devices are described in detail by Pai [18] and Rusterholtz [19].

Air heater

The air flow was preheated to up to1000 K by a resistive heater (Osram Sylvania 8 kW Hot Air System). A Sierra Instrument Smart Trak digital mass flow meter calibrated for air was used to regulate laboratory grade air from 5 atm to 1 atm. Its flow rate can be adjusted from 0 to 30 NL/min. The air then flowed into the resistive heater where it passed through a ceramic heating coil. The metal tube flowed air vertically from the bottom to the top. The temperature of the heated air was controlled in closed loop with the temperature measured by an internal thermocouple located 2.5 cm before the heater exit. The exit internal diameter was 1.5 cm and its external diameter 2.5 cm. The temperature 2 cm downstream of the heater exit had been shown to remain stable within 50°C over several hours of run time [18].

Electrode assembly

The NRP discharge setup is sketched in Figure 3.1. The NRP discharges were generated between two refractory steel pin electrodes separated by an adjustable gap distance of 2-4 mm. The pins had a diameter of 2 mm with sharpened tips and were placed in a vertical pin-pin configuration with the anode above the grounded cathode. The electrode assembly is mounted on two orthogonal micrometric translation stages allowing horizontal movement. Another vertical translation stage permits to move the anode from the cathode so that the gap distance is adjustable.

The cathode was placed as close as possible to the air flow exit so that the NRP discharges were created in a preheated (300-1000 K) atmospheric pressure air environment. The room temperature or preheated air flow was introduced from the cathode side, flowing parallel to the pins at 0.5-2.6 ms^{-1}.

Pulse generator

In this experiment, the pulse generator is a FID Technology FPG 10-30MS pulse generator, called "FID-1" for convenience. This pulser produces high voltage pulses of

10 ns duration, 1-30 kHz pulse repetition frequencies (PRF) and up to 5-10 kV amplitude (see Table 3.1). The output characteristics of this pulse generator were discussed in detail by Pai [18].

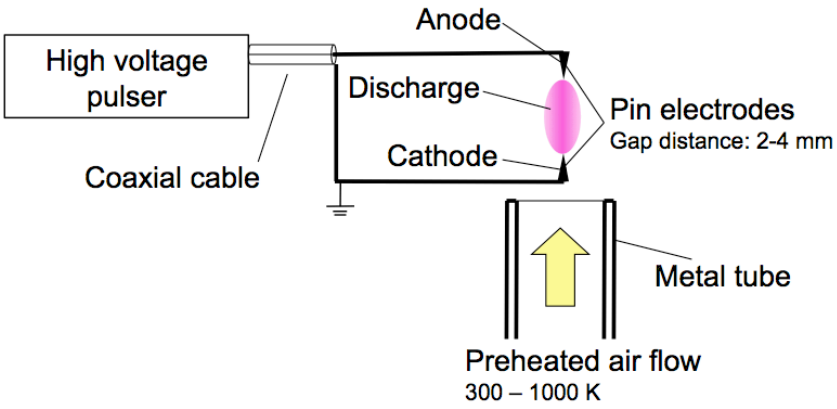

Figure 3.1 Schematic of the setup for the study of NRP discharges in preheated air.

3.2.2 Combustion chamber for plasma-assisted ignition

Cylindrical constant volume vessel

The schematic of the combustion chamber and its electric circuit are presented in Figure 3.2. The chamber used is a cylindrical pressure vessel of internal diameter 5 cm and internal length 5 cm, thus the volume of the chamber is about 100 cm^3. The test chamber is constructed from stainless steel with two sapphire windows of usable diameter 5 cm.

A propane-air mixture with equivalence ratio $\phi = 0.7$ was prepared in a 10-bar gas cylinder prior to the test. The gas cylinder was equipped with a gas regulator connected to the combustion chamber. The pressure in the combustion chamber was monitored with an MKS Baratron pressure gauge. Before each run, a vacuum pump (Pfeiffer DUO-2.5) pumped out the gas in the combustion chamber to a vacuum of pressure less than 1 mbar. Then the chamber was filled with the propane-air premix to the desired test pressure (between 1-10 bar). To precisely regulate the pressure, any excess gas was evacuated by an exhaust valve on the top of the chamber. Filling and regulating were controlled manually at very low flow rate, and we then waited at least 1 minute before the experiment to ensure that the gas in the combustion chamber was quiescent at the time of ignition.

A quartz pressure transducer (AVL 8QP500c) was used to measure the pressure rise during combustion. The pressure transducer had a measuring range up to 150 bar and a sensitivity of 11.43 pC/bar. The signal was then amplified by a charge amplifier (KISTLER type 5018) and was finally recorded with a 1-GHz LeCroy Wavepro7100 oscilloscope.

Electrode assembly

The NRP discharges were generated between two pin electrodes separated by a

gap distance of 0.6 mm. The pins had a diameter of 2 mm with sharpened tips and were placed in a horizontal, opposed, co-linear configuration to form a spark gap in the center of the combustion chamber. The electrodes were isolated from the metallic chamber using Teflon holders.

Pulse generator

In this experiment, two pulse generators were used (see Table 3.1). The FID-4 was selected to characterize the plasma kernel at 1-2 bar. This pulser produces high voltage pulses of 10 ns duration, 1-10 kHz pulse repetition frequencies (PRF) and up to 10 kV amplitude. FID-2 was used to study the effects of NRP discharges on lean mixture ignition at elevated pressures (up to 10 bar). The output characteristics of the generators will be discussed in Section 3.3.

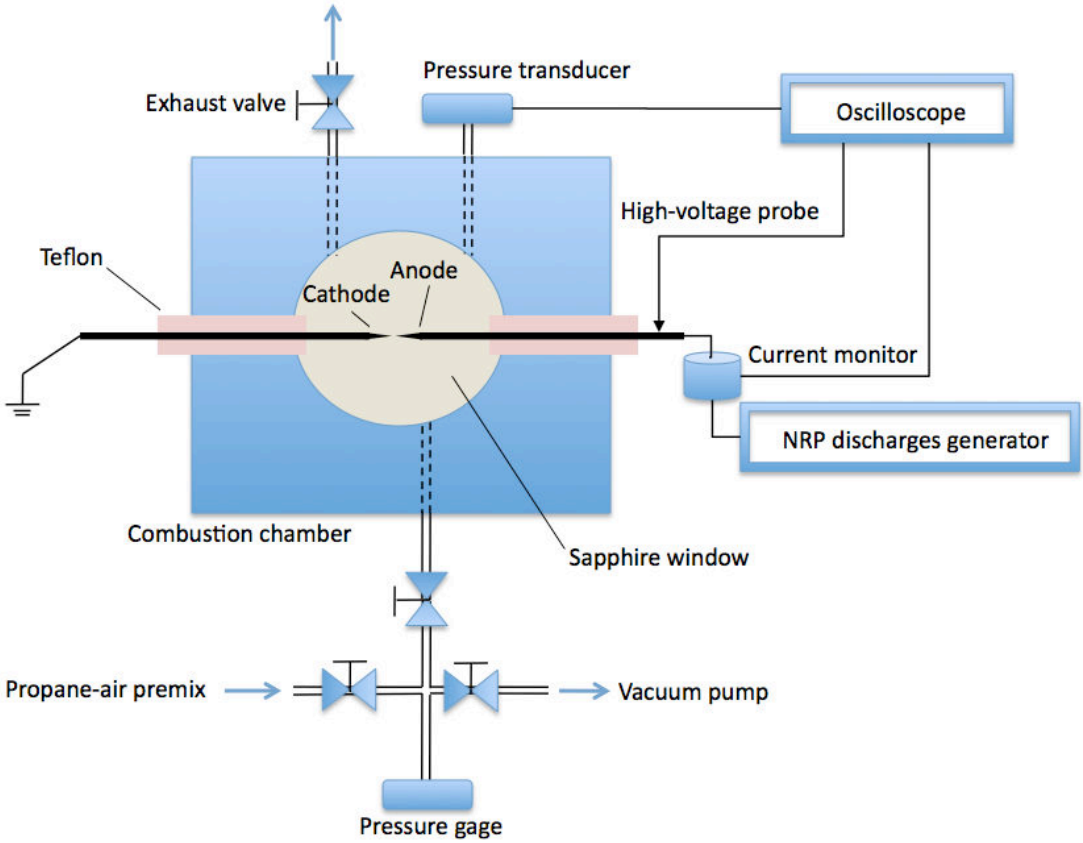

Figure 3.2 Side-view schematic of the combustion chamber and its electrical circuit.

3.2.3 Mini-PAC burner for plasma-assisted combustion dynamics

The plasma-assisted combustion dynamics experiments presented in this thesis were conducted with the premixed burner described by Pilla [2]. We used this burner to produce a fully developed flame stabilized on a bluff body.

Mini-PAC burner

The burner had been originally built to study the plasma-assisted stabilization of

lean-premixed flames. In this burner, the flame is stabilized by a bluff-body, as shown in Figure 3.3. The flow rates of air and propane, controlled by digital mass-flow meters (BRONKHORST F-202AC-FAC-44-V and F-201AC-AAA-33-V respectively), were set to 2.5 Nm^3/h and 8.2×10^{-2} Nm^3/h, respectively. The equivalence ratio was 0.8 and the heat release rate of the flame was about 1.9 kW. The internal diameter of the burner outlet is 16 mm. Premixed conditions were achieved 40 cm upstream of the burner outlet. A cylindrical bluff-body with diameter 10 mm, made of aluminum, was placed at the burner exit to stabilize a classical V-shaped, well-developed premixed flame. The axial flow velocity was about 10 m/s. With these settings, combustion takes place in a stable regime, with a fully developed flame. The Reynolds number, based on the diameter of the burner outlet and the bulk gas velocity, was about 3×10^3, thus the flow was just above the turbulence threshold.

Electrode assembly

The NRP discharge setup is sketched in Figure 3.3. The 1-mm-high cone at the center of the bluff-body was used as a cathode. The purpose of this cone is to stabilize the discharge spatially when optical diagnostics are conducted. The anode is a refractory steel pin electrode placed 5 mm above the cathode, in the recirculation zone of the flow.

Pulse generator

In this experiment, the pulse generator was the FID Technologies FPG 30-100MC4k pulser, designated as "FID-2", which produces high voltage pulses of 10-ns duration, 1-50 kHz pulse repetition frequency (PRF) and about 7-kV amplitude. The pulses were sent through coaxial cables connected to the electrodes. We chose FID-2 in this experiment because of its capability to operate in a wider range of PRF (1-80 kHz) than our other pulsers (1-30 kHz).

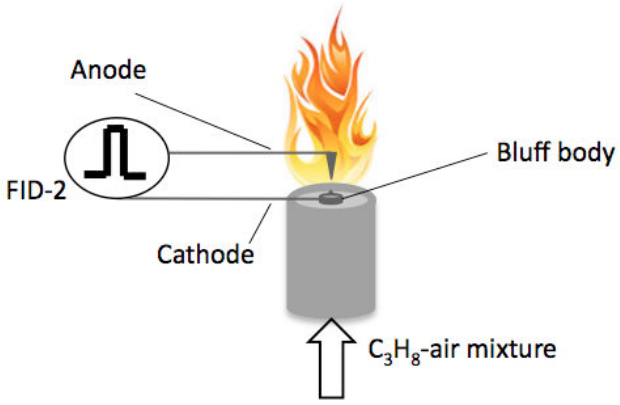

Figure 3.3 Schematic of the premixed burner "Mini-PAC" and its electrical circuit.

3.3 Electric energy measurement

3.3.1 Voltage and current measurement

The instantaneous discharge power was obtained by multiplying the voltage and current waveforms using the relation:

$$P(t) = V(t) \cdot I(t) \tag{3.1}$$

Integration of the power over the pulse duration then gives the electric energy deposited in the plasma:

$$W = \int_{\tau} P(t)dt \tag{3.2}$$

The voltage across the electrodes was measured with a 100-MHz bandwidth high-voltage probe (LeCroy PPE20kV). The current was measured with a Pearson coil current monitor (Model 6585) followed by a low-voltage attenuator (Barth Model 2-20) with 20dB attenuation and 0-20 GHz bandwidth. Both signals were recorded simultaneously with a 1-GHz LeCroy Wavepro7100 oscilloscope. The temporal synchronization of the voltage and current signals will be described in Section 3.3.2.

Figure 3.4 shows a schematic diagram of the electrical measurement setup. The voltage probe tip was attached to the anode, and the ground clip was attached to the grounded cathode. The current monitor was placed on the anode side, with the anode wire passing through the hole in the monitor. The wire was insulated from the inner case and the outer shield of the current monitor was grounded through its mounting holes.

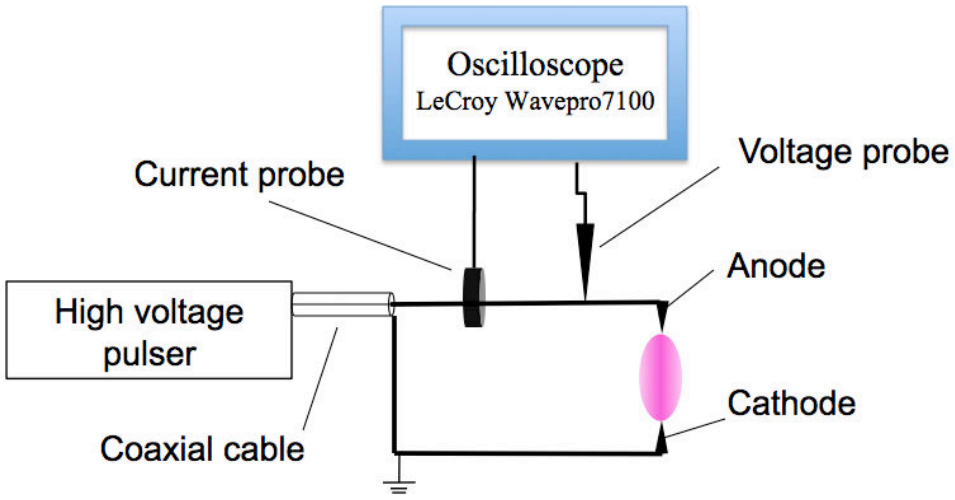

Figure 3.4 Schematic diagram of the generic electrical measurement setup.

The high-voltage performance of the Lecroy PPE20kV was previous validated [2]. It was proven to be able to measure the 5-ns rise time and the 10-kV amplitude of the high-voltage pulse.

For the current signals studied in the thesis, there are several criteria for choosing the adequate current monitor [64]. First, the rise time of the pulse to be recorded should be longer than the minimum rise time of the current monitor, otherwise the pulse signal cannot be correctly detected. Second, the maximum current of the pulse should be less than the rating of the current monitor to avoid damage to the coil. Third, the power of the signal should be lower than the rating of the current monitor. The Pearson Electronics company uses the product of the peak current (amps) and the maximum

pulse length (seconds) to estimate the power. Finally, the frequency of the signals should be in the range of the frequency domain viewed by the current monitor.

According to the above criteria, Table 3.2 shows a comparison between the characteristics of Pearson 6585 and the signal to be viewed in this thesis. It can be seen that the Pearson 6585 is adequate to measure current in the range of the thesis.

Table 3.2 Comparison of characteristics of Pearson 6585 and signal to be viewed.

	Pearson 6585 specifications	Signal to be viewed in this thesis
Maximum peak current	500 A	~ 100 A
Maximum I×t	0.002 A s	~ 0.000002 A S
Min. rise time	1.5 ns	> 5 ns
Frequency range	400 Hz[a] - 200 MHz[b]	1 MHz[c] - 50 MHz[d]

[a] This value corresponds to the low frequency 3dB cut-off

[b] This value corresponds to the high frequency 3dB cut-off

[c] This value corresponds to the estimated lowest frequency component of the signal (i.e. when wavelength ~ 1 μs)

[d] This value corresponds to the estimated highest frequency component of the signal (i.e. when wavelength ~ 20 ns)

3.3.2 Synchronization

The voltage and current signals were recorded simultaneously for the same single event but they were not naturally synchronized. On the one hand, the cables have different lengths so that the propagation time for voltage and current signals are different. On the other hand, the time responses of voltage and current monitors are not the same. Thus we should first synchronize the signals.

The synchronization was done with a low voltage applied on the electrodes so that there was no discharge. In this case, the electrodes gap can be considered as a pure capacitance, so the measured current is purely a capacitive displacement current, which can be calculated from the voltage waveform:

$$I_{disp} = C\frac{dV}{dt} \tag{3.3}$$

Here C is the capacitance of the electrode gap. Figure 3.5 presents the measured total current and calculated displacement current. The capacitance of the electrodes gap was deduced by matching the amplitudes of the measured and calculated current waveforms. In this example, we find C = 12 pF. The time delay between the measured and calculated current waveforms was measured at the 50% of the rising edge. The resulting time delay is measured at 2.4 ns. Then, we applied this time delay to all measured current waveforms in the same experimental conditions, so that the voltage and current signals were synchronized (see Figure 3.6).

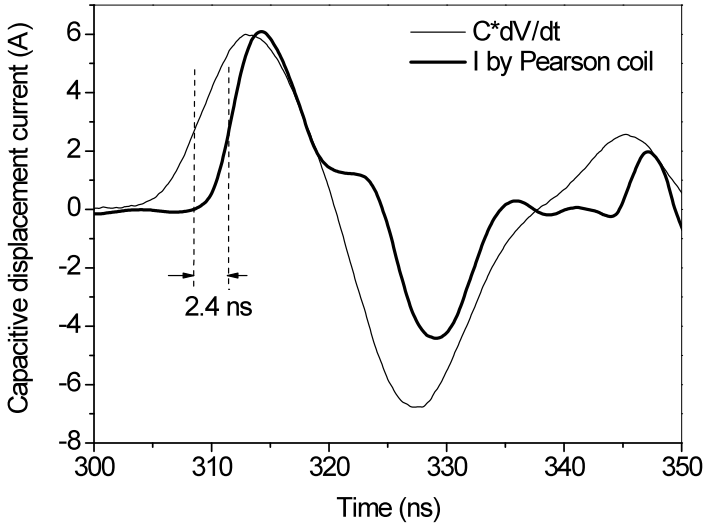

Figure 3.5 Determination of time delay between measured current and derivative of measured voltage without synchronization. FID-4, d=1.5 mm, PRF=30 kHz, 1-bar air, T=300 K.

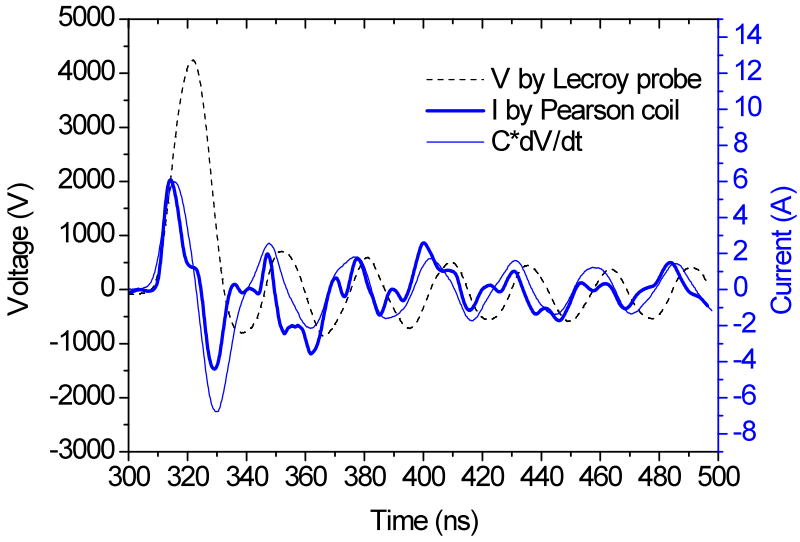

Figure 3.6 Measured voltage, measured current, and calculated current after synchronization. FID-4, d=1.5 mm, PRF=30 kHz, 1-bar air, T=300 K.

3.3.3 Output characteristics of the FID pulse generators

In this section, we examine the effects of the external load on the output characteristics of the FID pulse generators. It has been shown previously by Pai [18] that if the external load is too small, the FID pulse generator can no longer produce a rectangular pulse. Thus it is important to characterize the range of external loads for correct operation.

In fact, the FID pulse generators capable of producing high-PRF, high-voltage pulses rely on a high-power Drift Step Recovery Diode (DSRD). Like other semiconductors, the DSRD has two on-off operation modes: a "forward bias" mode when the diode behaves as a conductor, and a "reverse bias" mode when the diode

behaves as a capacitor with a very small capacitance (~ pF), known as current cut-off. When the diode switches from forward conduction to reverse cut-off, it takes some time, called the "reverse recovery time". For the DSRD, the reverse recovery time is extremely short, on the order of a nanosecond. When the operation mode changes, the current is cut off abruptly, and a high-voltage pulse can appear due to the self-inductance of the circuit.

To change the operation mode of the DSRD, one should apply a pulsed current signal around zero. The company FID uses the oscillation generated by the RLC circuit to do this task. However, if the external load resistance is too small, the oscillation of the RCL circuit is damped. As a result, the DSRD operation mode cannot be switched off correctly. For this reason, it is essential to avoid operating with a small external load. More details on the operation of the FID pulse generator can be found in Ref [18].

Here we consider the FID generator as a "black box" and characterize its output as a function of its external load resistance. We connected 1 or 3 W low-inductance metal -film resistors (Vishay BC Components PR01 and PR03) to the generator's external load (see Figure 3.7). Since all FID pulse generators share the same DSRD technology, which generator used is of less importance. Here, the FID-4 is used to illustrate the principles.

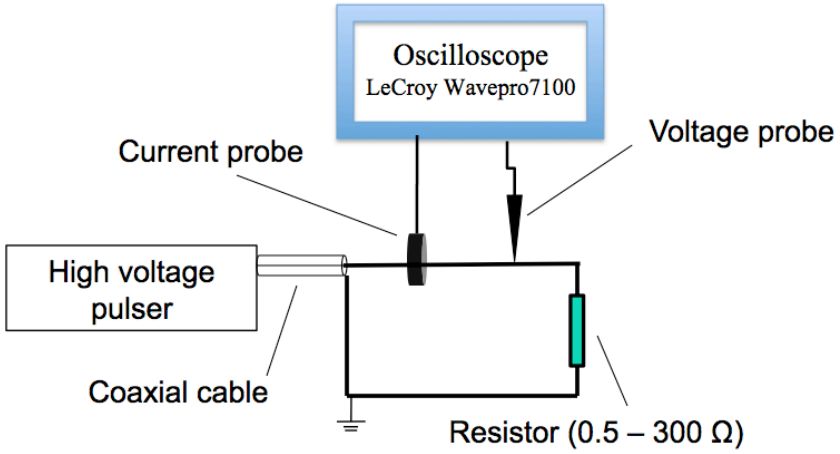

Figure 3.7 Diagram of the pulse generator system connected with external load resistor from 0.5 to 300 Ω.

The measured voltages across the resistors are shown in Figure 3.8. The measured currents are shown in Figure 3.9. We can see from Figure 3.8 that, except for the extreme case with very small R_{load}=0.5 Ω, the peak output voltage increases with increasing external load resistance. The general tendency of peak voltage variations can be explained by the transmission line model. For an ideal pulse generator, the pulse waveform V_S propagates down a transmission line and reflects at the load. The voltage at the load V_L is:

$$V_L = \frac{2Z_L}{Z_L + Z_0} V_S \tag{3.4}$$

where Z_L is the load impedance ($Z_L=R_{load}$), Z_0=150 Ω is the matching impedance of FID-4 (see Table 3.1), and V_S is the voltage provided by the pulse generator. Thus, for a given V_S, V_L increases with the load impedance. The maximum value of V_L, for an infinite load impedance (open circuit) is equal to 2 V_S. V_L is only equal to V_S when the load impedance matches the pulser load.

However, the transmission line model cannot explain the degradation of the voltage pulses when R_{load}<100 Ω. In Figure 3.8, for the 50-Ω case, the pulse waveform becomes wider. For the 10-Ω or 5-Ω cases, the pulse waveforms are completely deformed. For the 0.5-Ω case, an unexpected high-voltage pulse is seen.

Pulse degradation can also be seen on the measured currents. In Figure 3.9, for the 300-Ω and 100-Ω cases, the currents return to zero within 20 ns after the high-voltage pulse. For the 50-Ω case, the current pulse is elongated slightly in time. For the 10-Ω, 5-Ω, and 0.5-Ω, the current waveforms decay in a much longer time (>100 ns). Obviously, the FID generator fails to produce nanosecond pulses for external load resistances less than 50 Ω.

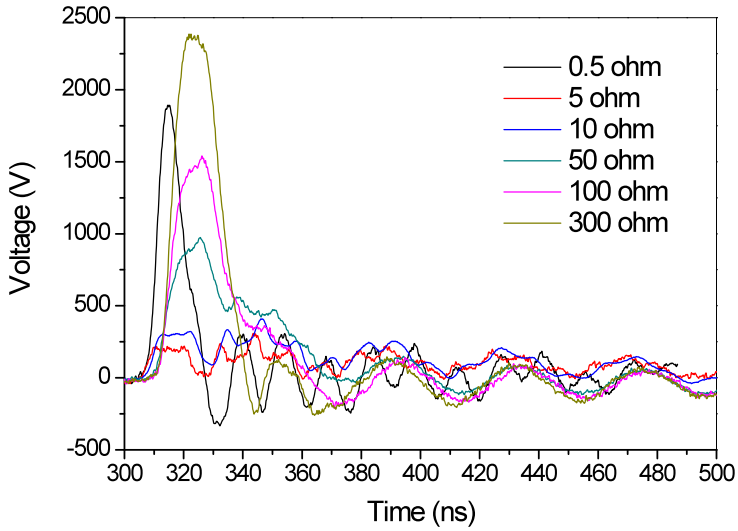

Figure 3.8 Measured FID-4 generator output voltage waveforms for external load resistances 0.5-300 Ω. The generator's output amplitude is tuned to the minimum value.

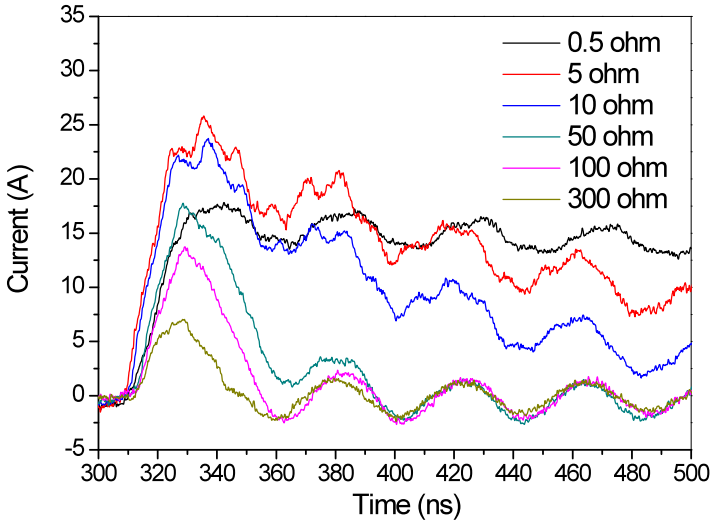

Figure 3.9 Measured FID-4 generator output current waveforms for external load resistance 0.5-300 Ω. The generator's output amplitude is tuned to the minimum value.

The experimental results obtained with FID-4 generator shows that the external load resistance has important effects on the output characteristics. The pulse generator operates in an optimal mode when R_{load} is around the matching resistance, and it enters a sub-optimal mode when R_{load} is about 50 Ω. For R_{load}<50 Ω, it cannot anymore produce correctly high-voltage nanosecond pulses.

Finally, from the energy point of view, the theoretical pulse power can be deduced using the transmission line model:

$$P = \frac{V_L^2}{R_{load}} = \frac{\left(\frac{2R_{load}}{R_{load}+Z_0}\right)^2 V_S^2}{R_{load}} = \frac{4R_{load}}{\left(R_{load}+Z_0\right)^2} V_S^2 \tag{3.5}$$

Thus the pulse energy is proportional to:

$$E \propto \frac{4R_{load}}{\left(R_{load}+Z_0\right)^2} \tag{3.6}$$

Figure 3.10 shows a comparison of the measured pulse energy with the theoretical transmission line model. In the theoretical model, the pulse energy would be the maximum in the matched case (R_{load}=150 Ω), however, the pulse energy continues to increase when R_{load}<50 Ω. This is because both the voltage and current pulses were deformed and elongated in time. Figure 3.11 presents the pulse energy deposition as a function of time, calculated form the voltage and current waveforms:

$$W = \int_0^t V(t) \cdot I(t) dt \tag{3.7}$$

We can see that for the cases R_{load}<50 Ω, the pulse generator continues to output energy, due to pulse deformation.

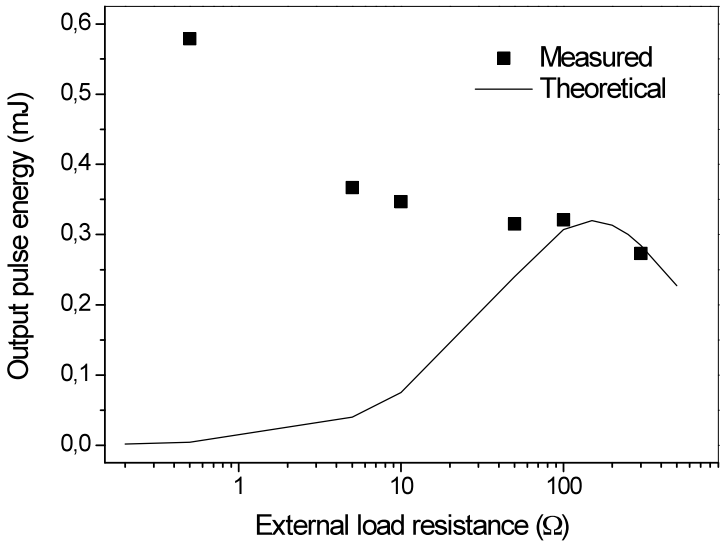

Figure 3.10 Measured (symbols) and theoretical (line) output energy as a function of the external load resistance.

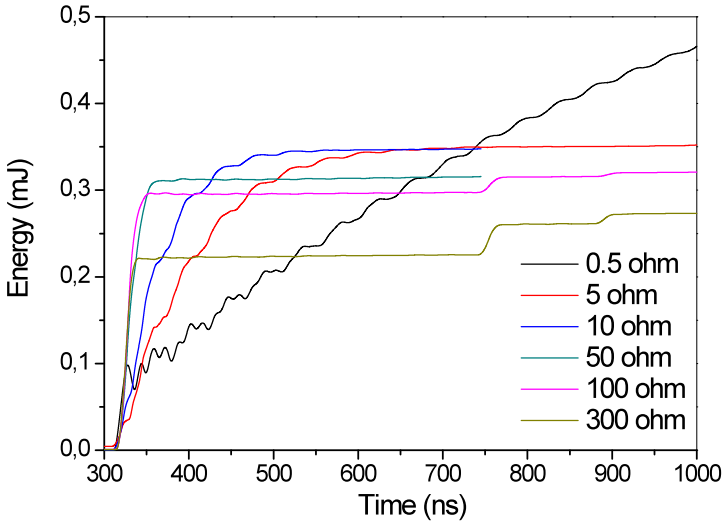

Figure 3.11 Measured output energy as a function of time for different external load resistances.

In conclusion to the above analysis, it is important to check the external load resistance. In the case when the external load is a plasma formed across a small gap distance (< 2 mm in some of our ignition experiments), the plasma resistance falls to a very small value during the pulse, and the FID generator may not produce a clean pulse. In this case, we simply add a 50-Ω low-inductance resistor in series to keep the generator in an optimal operation mode. Adding higher resistance increases the loss of energy in the resistor, thus 50-Ω seems to be the best compromise.

3.3.4 Examples of energy measurement

Here we give some examples of measured voltage and current waveforms, as well

as of calculated pulse energy. We define time "0" as the time corresponding to the time at which the voltage reaches half of its maximum amplitude (RHM or Risetime Half Maximum). The current waveforms presented are all conduction currents unless otherwise specified. The conduction current is defined as:

$$I_{cond} = I_{total} - I_{disp}, \quad with \quad I_{disp} = C\frac{dV}{dt} \tag{3.8}$$

Preheated air

In this experiment, the NRP discharges were fired at a PRF=1-10 kHz. The gap distances were 2-4 mm. The plasma impedance was enough for the pulse generator to operate correctly, so we connected the generator to the electrodes through the coaxial cable (without the extra 50-Ω resistor). The pulse waveforms were clean, which can be seen from Figure 3.12. In this example, the pulse energy was 1.6 mJ.

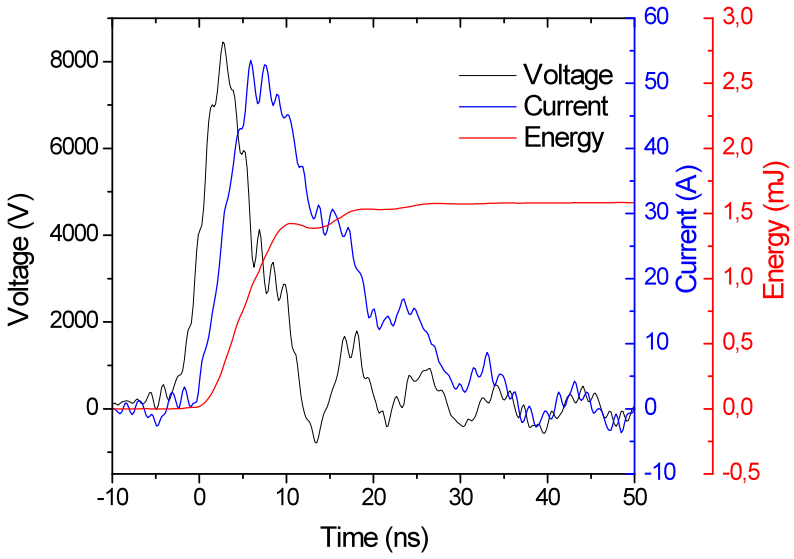

Figure 3.12 Measured voltage, current waveforms and calculated energy of NRP discharges in preheated air. FID-1, d=4 mm, PRF=10 kHz, 1-bar air, T=1000 K.

Ignition

For ignition applications, only a train of NRP pulses was used. In the experiments, due to the small gap distance, a 50-Ω resistor had to be added to make the generator operate correctly. We measured the voltage applied on the electrodes and the current flowing through them. We found that the first output pulse of the generator is different from the pulses after. Figure 3.13 shows that the peak voltage of the first pulse is about 10 kV, while Figure 3.14 shows that the peak voltage of the second pulse is only half this value, about 5 kV. This is because the first pulse pre-ionizes the air in the gap, which creates more favorable conditions for breakdown by the second pulse. In other words, the air plasma impedance during the second pulse is smaller than that during the first pulse. According to the transmission line model, the peak output voltage decreases. In this example, the first pulse's energy was 2.25 mJ, and the second pulse's energy was 0.8 mJ.

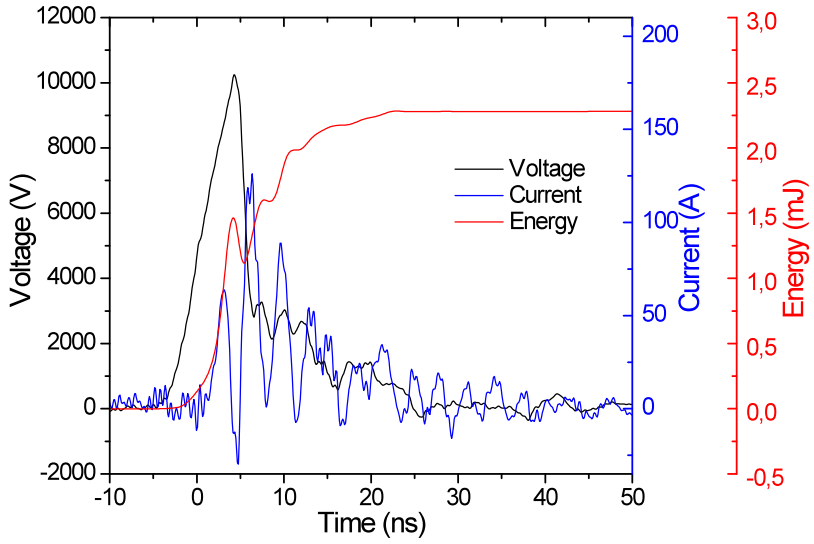

Figure 3.13 Measured voltage, current waveforms and calculated energy of the 1st pulse discharge for ignition. FID-4, d=0.6 mm, 100-Ω in series, PRF=30 kHz, 1-bar propane-air mixture Φ=0.7, T=300 K.

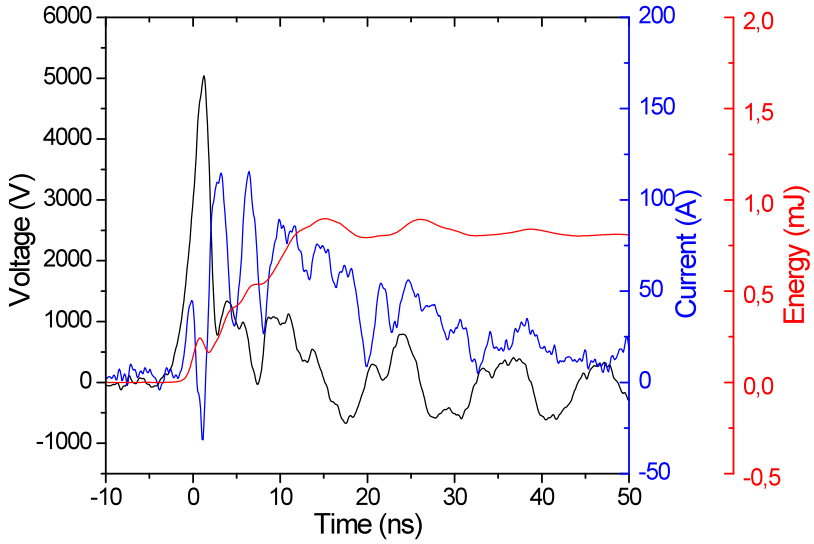

Figure 3.14 Measured voltage, current waveforms and calculated energy of the 2nd pulse discharge for ignition. FID-4, d=0.6 mm, 100-Ω in series, PRF=30 kHz, 1-bar propane-air mixture Φ=0.7, T=300 K.

Combustion dynamics

To show the effects of NRP discharges on combustion dynamics, the pulses were fired at variable PRF=10-80 kHz. As shown in Figure 3.3, the plasma was generated above the bluff-body of the Mini-PAC burner. The gap distance was 5 mm and the pulse waveforms were clean. Hence, no resistor was added. In this example, the PRF was fixed at 30 kHz, the energy per pulse deposited into the plasma was 0.35 mJ. Thus the plasma power was 10.5 W.

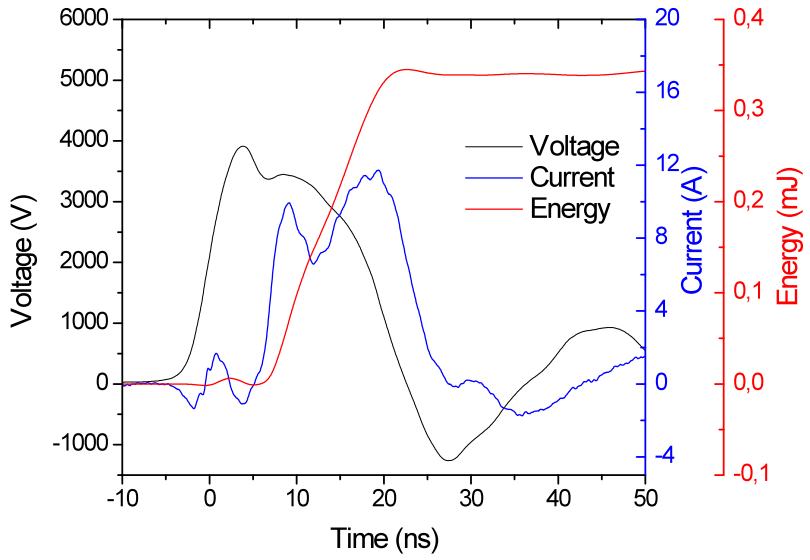

Figure 3.15 Measured voltage, current waveforms and calculated energy of the NRP discharges for combustion dynamics control. FID-2, d=5 mm, PRF=30 kHz, burned gas of 1-bar propane-air flame.

3.4 Schlieren technique

3.4.1 Schlieren theory and general setup

The schlieren technique has been used for centuries to observe inhomogeneities of transparent media like air and water, based on the refraction of light by the refractive index gradient. A general description of the technique may be found in Ref [65]. For air and other gases, the refractive index changes with the gas density ρ according to the Gladstone-Dale formula:

$$n-1=k\rho \tag{3.9}$$

where the Gladstone-Dale coefficient, k, is about 0.23 cm^3/g for air at standard conditions. The refractivity *(n-1)* or the refractive index n of a gas depends on the density, temperature, composition and the wavelength of illumination. Thanks to light refraction, shock waves or heated gas fronts with sharp density gradients can be visualized.

In the thesis, we assume that the gas density distribution in the NRP discharge channel is axisymmetric. The deflection angle α of a parallel light beam passing through the discharge channel at position y, shown in Figure 3.16, can be expressed as [43]

$$\alpha(y)=2y\int_y^{R_0}\frac{1}{n(r)}\frac{\partial n}{\partial r}\frac{dr}{\sqrt{r^2-y^2}} \tag{3.10}$$

where R_0 is the radial extent of the region perturbed by the discharge. In the undisturbed region $r > R_0$, ρ equals ρ_0, the ambient gas density.

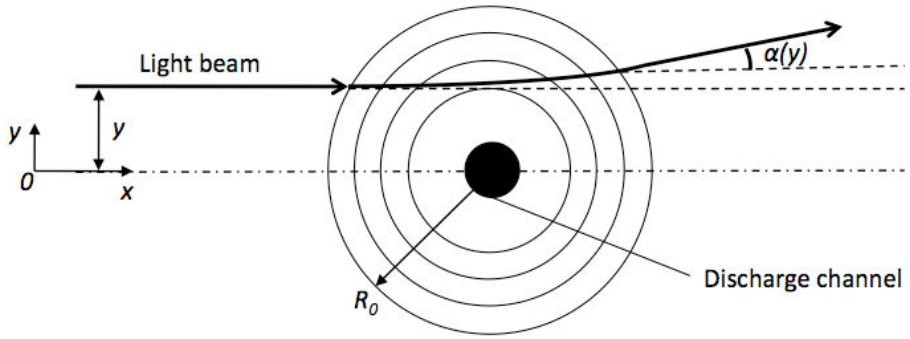

Figure 3.16 Beam deflection angle caused by a cylindrical density distribution.

In a schlieren system (as sketched in Figure 3.17a), the beam from the light source is collimated by Lens 1, then passed through the object (discharge region), and is finally refocused by Lens 2 to produce an image of the light source on the knife-edge plane. The object and the camera's image plane are placed on each side of Lens 2, both at twice the focal length of Lens 2, so that an inverted, same-size real image of the object is formed at the camera's image plane. In the case without knife-edge, whether there is light deflection or not, no difference in the image illumination is observed, because the light deflected is refocused on the same point in the camera, resulting in the same illumination.

Now, a vertical knife-edge is placed at a distance f_2 of Lens 2 to partially block the light source image (presented as a shaded ellipse in Figure 3.17b). Because the light source is not infinitesimally small (otherwise there is no schlieren, only a black-and-white image), the image of the light source at the knife-edge also has a finite spatial extent. The light beam that is deflected horizontally (in the y direction) moves towards or away from the knife-edge, passing fewer or more photons, thus resulting in a darker or lighter point in the image. For example, in Figure 3.17b, the dotted line ellipse shows a light beam moving away from the knife-edge, thus producing a lighter point in the image. In this way, the degree of deflection can be visualized as a gray-scale image.

We will discuss now how gas density profiles relate to gray-scale schlieren images.

We define I as the image illumination at the camera's image plane, and I_0 as the image illumination at the camera's image plane without knife cut. The change of image illumination ΔI at position y is related to Δd, the y-direction displacement of the source image at the knife-edge plane due to the light deflection, which is proportional to the deflection angle induced by the discharge [65]:

$$\Delta d = f_2 \alpha(y) \tag{3.11}$$

where f_2 is the focal length of Lens 2.

The y-direction displacement Δd can then be expressed as a function of the density profile $\rho(r)$, using equations (3.9-11):

$$\Delta d = 2 f_2 y \int_y^{R_0} \frac{k}{1+k\rho(r)} \frac{d\rho}{dr} \frac{dr}{\sqrt{r^2 - y^2}} \tag{3.12}$$

The relation between ΔI and Δd is not initially known. If the light source image at the knife-edge plane is rectangular and uniform, there is a linear relation between I and d, thus ΔI/Δd is constant [65]. However, this is not usually the case. For example in our study, the flashlamp light is emitted by an intense spark in air, which is neither uniform nor rectangular. Therefore an additional experimental procedure should be done to find the change of image illumination ΔI as a function of the y-direction displacement Δd. This procedure is detailed in the next subsection.

The image contrast *C(y)* is defined here as the ratio of the change of image illumination to the illumination without knife cut:

$$C(y) = \frac{\Delta I}{I_0} \tag{3.13}$$

Using the relation between *ΔI* and *Δd*, equation (3.13) can then be used to obtain *C(y)*. The image contrast *C(y)* can be used to generate numerical gray-scale images.

We have seen that it is possible to generate a numerical image from the density profile. The process is the so-called numerical schlieren method. We call the experimental procedure consisting in finding the relation between *ΔI* and *Δd* the numerical schlieren calibration.

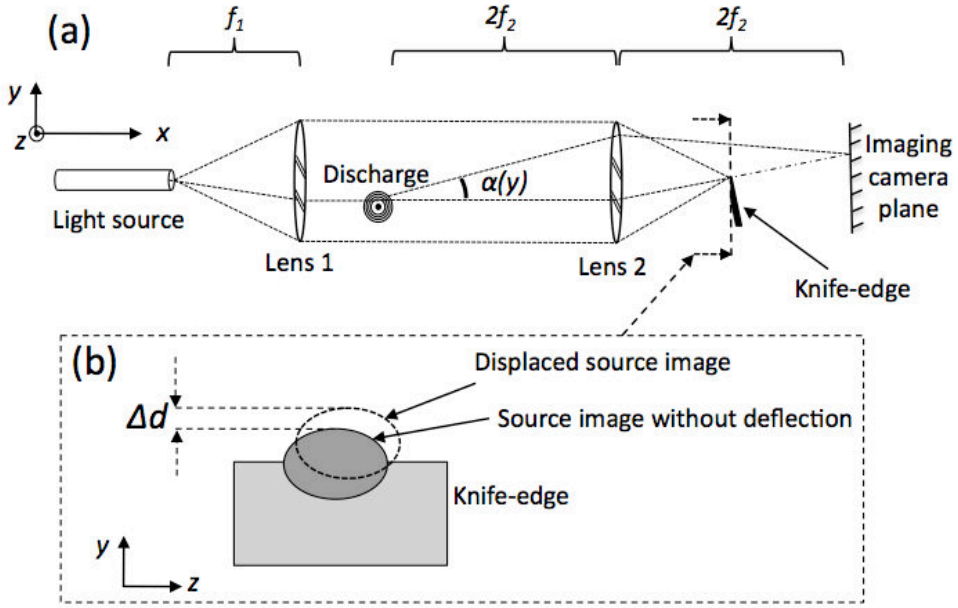

Figure 3.17 (a) Typical schlieren configuration (upper view) and (b) schematic of the source image displacement at the knife-edge plane.

3.4.2 Numerical schlieren calibration

A calibration was performed without plasma discharge to find the relation between *ΔI* and *Δd* for every schlieren image recorded. This process is necessary for generating numerical schlieren images with correct contrast profiles as stated in the previous

subsection. The procedure consisted in 1) measuring I_0 without the knife cut, and 2) measuring I as a function of the knife-edge position, and then normalizing I by I_0. The results are shown in Figure 3.18.

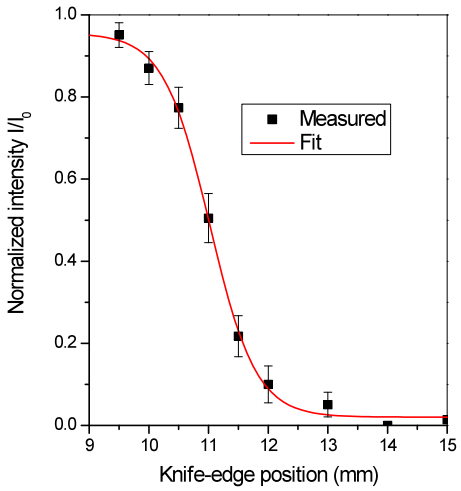

Figure 3.18 Image illumination as a function of knife-edge position.

We obtain a continuous variation by fitting the experimental data with a function of the form:

$$\frac{I}{I_0} = a_2 + \frac{a_1}{1 + e^{(d-d_0)/a_3}} \tag{3.14}$$

where $a_1 = 0.935$, $a_2 = 0.02$, $a_3 = 0.386mm$, $d_0 = 11.022\,mm$

Because the flashlamp is spatially unstable, we do not know *a priori* the knife-edge position d_b for the schlieren images. To circumvent this problem, we first determine the average background pixel intensity of the image, denoted I_b, and we determine d_b using Figure 3.18 and the measured value of I_b/I_0. This is equivalent to solving the equation

$$\frac{I_b}{I_0} = a_2 + \frac{a_1}{1 + e^{(d_b-d_0)/a_3}} \tag{3.15}$$

In the region where light is deflected, with a y-direction displacement Δd, the image pixel intensity is expressed as

$$\frac{I_b + \Delta I}{I_0} = a_2 + \frac{a_1}{1 + e^{(d_b+\Delta d-d_0)/a_3}} \tag{3.16}$$

Using equations (3.15) and (3.16), and recalling the definition of contrast given by equation (3.13), we thus obtain:

$$C = \frac{\Delta I}{I_0} = \frac{I_b + \Delta I}{I_0} - \frac{I_b}{I_0} = \frac{a_1}{1 + e^{(d_b+\Delta d-d_0)/a_3}} - \frac{a_1}{1 + e^{(d_b-d_0)/a_3}} = K_2\left(\frac{a_1}{K_2 - K_1 e^{\Delta d/a_3}} - 1\right) \tag{3.17}$$

$$with \quad K_1 = \frac{I_b}{I_0} - a_1 - a_2, \quad K_2 = \frac{I_b}{I_0} - a_2$$

3.4.3 Adapted schlieren configuration for NRP discharges in preheated air

The schlieren configuration should be adapted to meet the needs of visualizing the rapid development of a hydrodynamic expansion. First, the short lifetimes of shock waves (tens to hundreds of nanoseconds) require a short duration, intense light source to freeze the motion. Second, the weak shock waves produced by the NRP discharges in heated air require good schlieren sensitivity. Finally, the small plasma dimensions require a magnification of the schlieren image.

As shown in Figure 3.19, the beam from the light source is collimated by a lens with 1-m focal length, passing through the NRP discharge, refocused by a spherical mirror with 2-m focal length to an image of the light source on the knife-edge plane. As the light source of the system, the arc channel of the flashlamp has a length of about 1 mm and a diameter of about 0.6 mm, giving a source image twice that size at the knife-edge plane. The knife-edge was placed vertically in order to better visualize the radial gradients of gas density. Note that the radial direction is the main direction of hydrodynamic expansion.

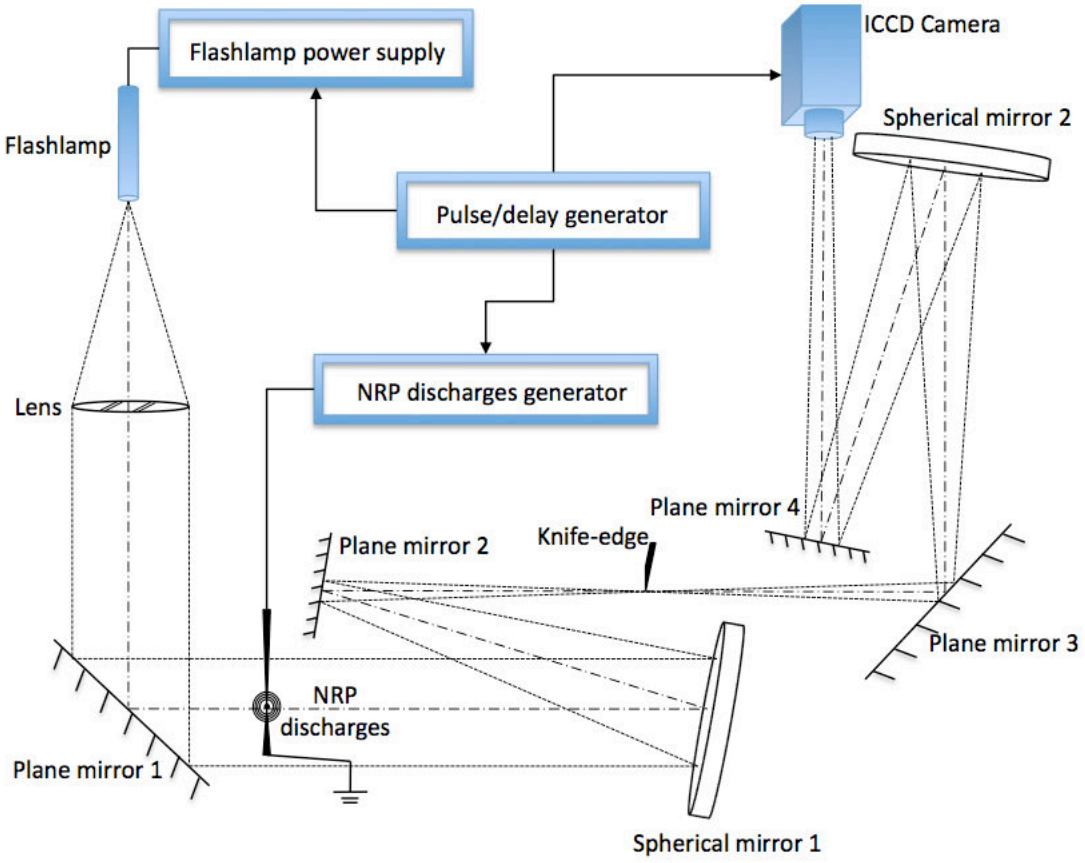

Figure 3.19 Schematic of the schlieren system (top view).

Geometric issues

Without the use of a focusing lens, the schlieren field lens or mirror (lens 2 in Figure 3.17) still forms a real image of the test area. Here we added a focusing lens (spherical mirror 2 in Figure 3.19) allowing one to control the image size independently.

Some geometric calculations are given here to determine the parameters of the schlieren system setup.

In Figure 3.20, a is the height of the object and b is the height of the image of a. The distances s, g, e, and x are defined in the figure. The thin lens approximation yields the following equations for the focal length f_2 of the second field lens:

$$\begin{aligned} \frac{a}{b} &= \frac{f_2}{f_2 + x} \\ \frac{a}{b} &= \frac{f_2 - s}{x} \end{aligned} \tag{3.18}$$

Resolving the above equations gives:

$$\begin{aligned} x &= \frac{{f_2}^2}{s} - f_2 \\ m_2 &= \frac{b}{a} = \frac{f_2}{s} \end{aligned} \tag{3.19}$$

where m_2 is the image magnification by lens 2, i.e. the ratio of image to test-area diameters.

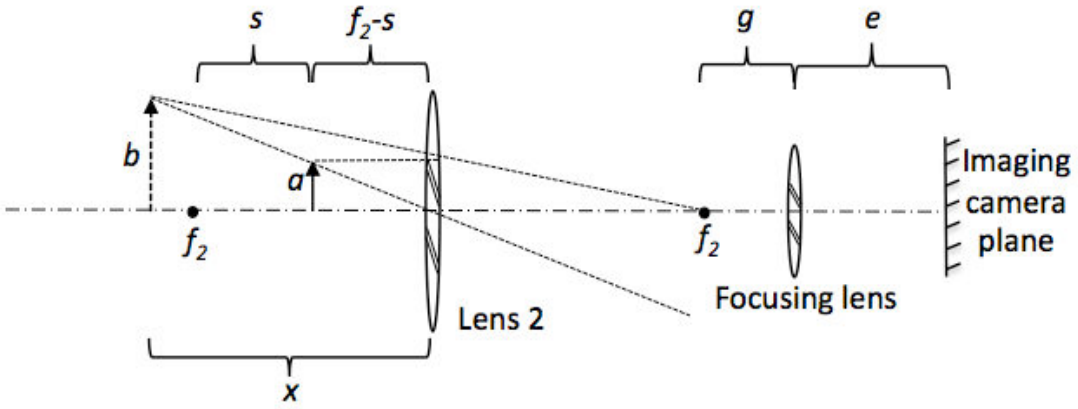

Figure 3.20 Diagram of the second field lens or mirror.

Likewise for the focusing lens, shown in Figure 3.21, we have:

$$\begin{aligned} e &= \frac{f_3\left(gs + {f_2}^2\right)}{{f_2}^2 + gs - f_3 s} \\ m_3 &= \frac{b}{c} = \frac{{f_2}^2 + gs - f_3 s}{f_3 s} \end{aligned} \tag{3.20}$$

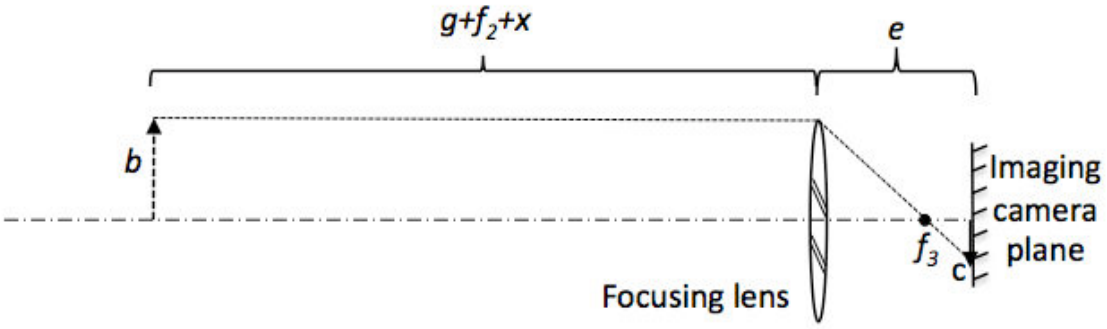

Figure 3.21 Diagram of the focusing lens or mirror.

The total magnification ratio m is given by:

$$m = m_2 m_3 = \frac{f_2 f_3}{f_2^{\,2} + gs - f_3 s} \tag{3.21}$$

In Figure 3.22 we plot the magnification m and the focusing distance e keeping s or g constant, respectively. We can see that increasing s or reducing g can both magnify the image. However, the magnification ratio increases at the expense of an increase in the focusing distance, thus an increase of the overall length of the optical train. In the experiments, we chose g=0.1 and s=0.2 as a good compromise, with a magnification ratio = 1.1 sufficient to visualize the object.

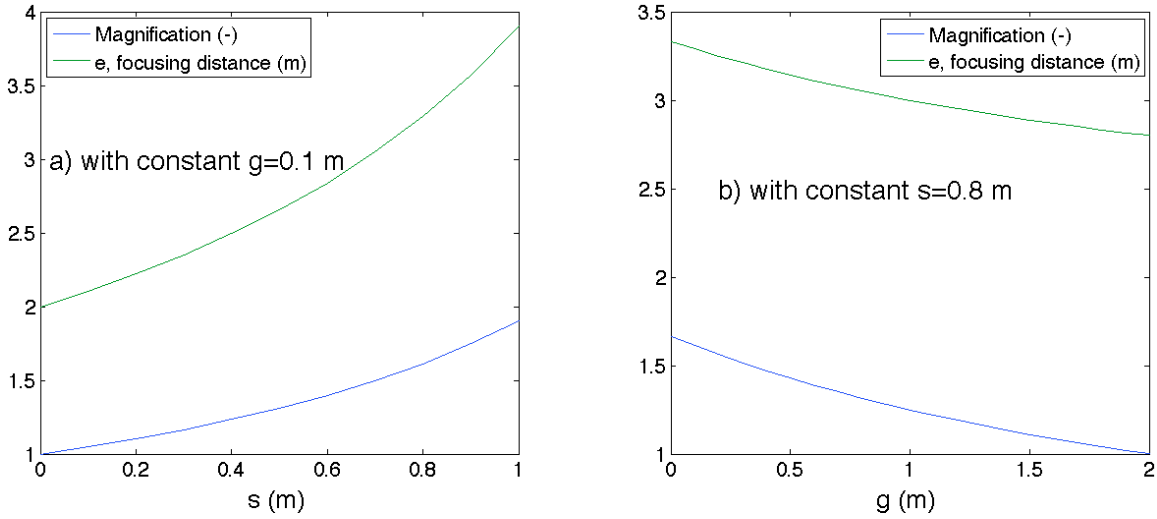

Figure 3.22 Magnification and focusing distance e, plotted vs. a) the distance s, keeping constant g=0.1 m, b) the distance g, keeping constant s=0.8 m. The distance s and g are defined in Figure 3.20. The focal lengths f_2=f_3=2 m.

Schlieren illumination and imaging camera

To provide sufficient image illumination for exposure times in the nanosecond range, pulsed light sources of high intensity should be used. In our experiments, the schlieren illumination was provided by a Nanolite flashlamp, which produces high-intensity, short duration arcs in air with a pulsing frequency of 1 Hz and a flash duration of about 20 ns, sufficient to freeze the shock wave in single-shot image recording. The flashlamp was intentionally run in low-frequency mode to reduce the

electrodes wear and to extend the flash lamp lifetime. It provides continuum of spectral emission that has advantages over coherent laser illumination because coherent light is not adequate for schlieren imaging due to the presence of diffraction fringes.

An intensified charge-coupled device (ICCD) camera (Princeton Instruments PI-MAX) with 512 × 512 pixel resolution recorded the schlieren images with a well-defined exposure time window, or gate width. The camera was run in Gate mode and the gate delay setting specified the synchronization of the flash lamp with the NRP discharge.

Sensitivity

The sensitivity of the schlieren system was ensured by the 300-mm diameter, 2-m focal length spherical mirror, because the schlieren sensitivity is linearly proportional to the focal length of this mirror. Another way to increase the sensitivity is to increase the knife-edge cutoff portion of the source image. However, this is limited by diffraction problems at the knife-edge and by the minimum image illumination required.

Magnification and aberration

As explained previously, a proper image magnification was achieved (~1 in the present investigation) at the expense of a very long optical length. A second spherical mirror with 2-m focal length served as focusing optics for the camera. Using only the central part of the mirror minimized the spherical aberration of the spherical mirrors. The coma aberration was minimized by reducing the offset angle between the incoming light beam and the mirror axis, and in doing so, additional plane mirrors had to be used to fold the optical path.

Synchronization

All NRP discharges were considered identical, and thus the schlieren images were taken from different discharges to show the temporal evolution. The synchronization of the NRP discharge with the flashlamp and the ICCD camera was achieved with a Berkeley Nucleonics (BNC 575) multi-channel pulse delay generator (200 ps RMS jitter). The BNC triggered the flash lamp and the camera at 1 Hz, and the discharge at 1 kHz or 10 kHz.

The synchronization strategy is shown in Figure 3.23. First, the ICCD gate delay was synchronized with the flashlamp light pulses. The ICCD gate width was narrowed to a value of 50 ns, during which time the camera received the 20 ns flash emission. The flash light sparks have a temporal jitter of about 100 ns, larger than the ICCD gate exposure time. As a result, not every flash is viewed by the camera because the flash light can arrive earlier or later than the gate exposure time. But fortunately, once the flash is viewed by the camera (i.e. when the flash enters in the ICCD gate exposure time), the timing accuracy is determined by the camera, which is ± 25 ns. To reduce the uncertainty, we recorded about 10 successful images for each gate delay. We then used these 10 images to determine the average radius of the shock wave and of the heated gas channel. Then we selected one image having characteristics closest to the average radius of the shock wave and of the heated gas channel. Second, the NRP discharges

were synchronized with the camera so that the start of the NRP plasma light emission arriving on the ICCD coincided with the start of the exposure gate. Finally, by varying the time at which the discharge was fired relative to the flashlight, the temporal evolution following the NRP discharge could be visualized.

To summarize, the schlieren system produces single-shot images of the post-discharge region with a time exposure of 20 ns and a timing accuracy of ± 25 ns.

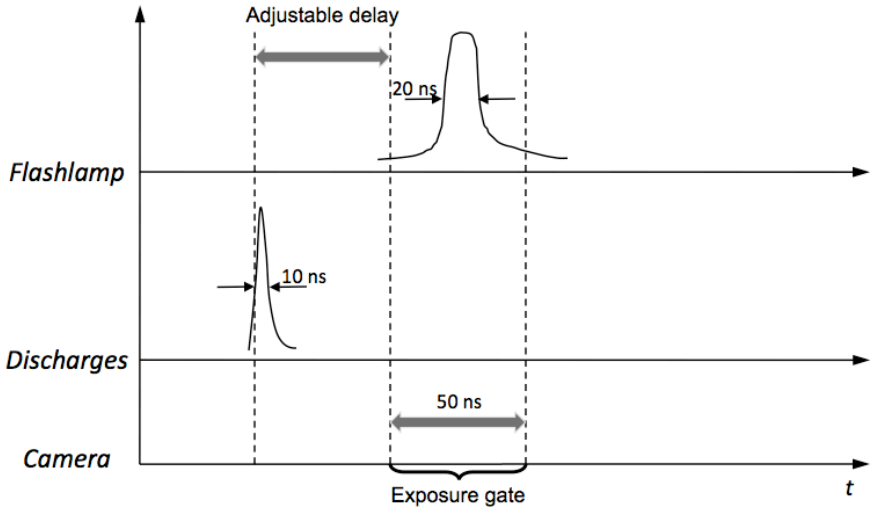

Figure 3.23 Schematic of the synchronization strategy.

3.4.4 Adapted schlieren configuration for ignition by NRP discharges

The spark ignition process generally involves three stages. The first stage is the electric breakdown followed by the formation of a plasma kernel on a time scale of 10 ns to microseconds. The second stage involves the growth the plasma kernel on a time scale of milliseconds. The final stage involves the ignition of the combustible gas mixture surrounding the hot plasma kernel to produce an auto-sustained, outwardly propagating flame. This occurs on a time scale of tens of milliseconds.

For the first and second stages of ignition, because the object of interest was the same as that in the preheated air experiments, the schlieren configuration described in Section 3.4.2 was adopted to visualize the NRP discharges and the plasma kernel.

For the last stage of ignition, on the contrary, the image should be demagnified because the flame front in the combustion chamber has a diameter up to 50 mm. Moreover, less sensitivity is required of the schlieren system because the flame front presents a high density gradient, thus large light deviation. A classical two-lens schlieren photography system for imaging of the flame front propagation in the combustion chamber can be easily constructed, with a third focusing lens for the camera. The illumination was provided by an 85W Hund halogen lamp. The schlieren images were captured by a monochrome fast camera (Photron FASTCAM-APX) with a resolution of 512×512 pixel allowing a frame rate of 10 kHz. A 105-mm NIKKOR lens was used as the focusing lens. Figure 3.24 shows a schematic of the schlieren system.

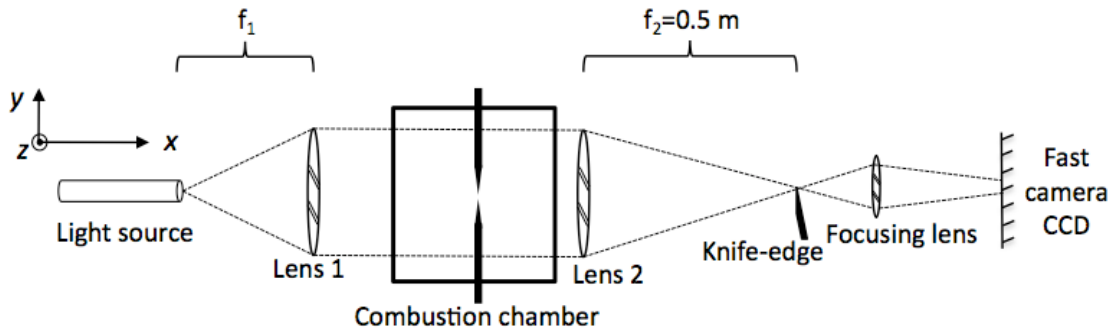

Figure 3.24 Schematic of the schlieren system for visualizing the flame propagation.

3.5 Planar laser-induced fluorescence (PLIF) imaging of OH radicals

The flame front is a region where many reactions occur, for instance, the oxidation of hydrocarbon fuels. One important intermediate species in the oxidation process is the OH radical. Because it is formed in the flame front, OH is a commonly used marker for this region.

Planar Laser-induced fluorescence (PLIF) is an optical diagnostic technique widely used in flame studies. It is applicable to a large number of molecules and atoms for combustion. In the current study, fluorescence is produced by excitating the OH radicals present in the flame by a Nd:YAG pumped dye laser.

As sketched in Figure 3.25, a frequency-doubled Continuum ND6000 dye laser is used with Rhodamine 590 dye diluted in methanol solvent and pumped by a Continuum Precision Nd:YAG laser. The laser was tuned to the $Q_1(6)$ transition of the (1,0) band of the $A^2\sum$-$X^2\prod$ system of OH, at 282.93 nm. The laser pulse energy is about 20 mJ. The thickness and the height of the laser sheet are approximately 0.1 and 7 mm, respectively. The OH fluorescence signal from the OH(A-X)(1,1) and (0,0) bands was collected using a 105-mm UV-NIKKOR lens, passed through a 10-nm bandpass filter (ZBPA310 Asahi Spectra Co.) centered at 310 nm, and was focused onto an intensified charge-coupled device (ICCD) camera (Princeton Instruments PI-MAX) with 512×512 pixels.

In the thesis, single-shot PLIF images were recorded at 15 μs after each high-voltage pulse. Because of the low signal levels, the PLIF signals were also accumulated over 200 events for further analysis. Synchronization of the NRP discharge with the laser and the ICCD camera was achieved with a Berkeley Nucleonics (BNC 575) multi-channel pulse delay generator (200 ps RMS jitter). The BNC triggered the laser at 10 Hz, the camera at 1 Hz, and the discharges at 30 kHz.

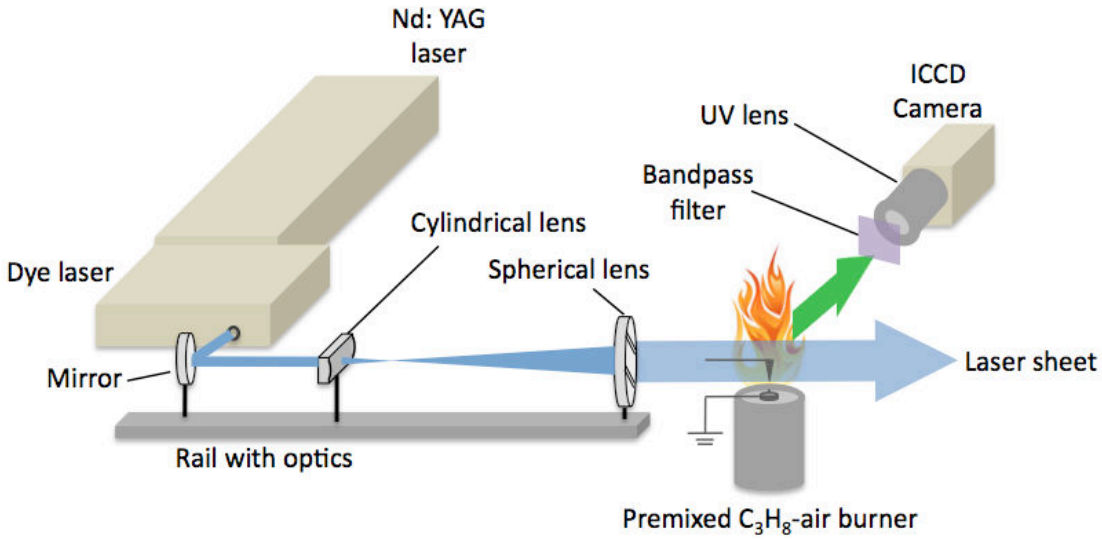

Figure 3.25 PLIF setup for OH radicals. The cylindrical lens focal length is 300 mm, and the spherical lens focal length is 500 mm. The thickness and the height of the laser sheet are approximately 0.1 and 7 mm, respectively. The laser sheet passed vertically above the bluff body. The 310 nm narrow bandpass filter was placed between the flame and the camera lens.

3.6 CH* and OH* chemiluminescence imaging

The emission of OH* and CH* were recorded to trace the location of the flame for comparison with PLIF images. Unlike PLIF, chemiluminescence imaging is a simpler technique, which uses chemical excitation instead of laser excitation. The camera records the light emitted from the chemically excited OH or CH, denoted OH* or CH* respectively.

These measurements were performed with the same optical setup as in the PLIF measurements but without the laser (see Figure 3.26). Longer gate times (or a larger number of accumulated events) on the image intensifier are required to increase the amount of light to a level sufficient for detection. As in the LIF imaging of OH, a 10-nm bandpass filter (ZBPA310 Asahi Spectra Co.) centered at 310 nm was placed in front of the UV camera lens, so that the detection system only recorded light around 310 nm. For CH* imaging, a 10-nm bandpass filter (ZBPA430 Asahi Spectra Co.) centered at 430 nm was used.

The chemiluminescence signals were accumulated over 500 events, because of the low signal levels. All measurements were taken at 15 μs after each pulse, as in the PLIF measurements. Synchronization of the NRP discharge with the ICCD camera was achieved with a Berkeley Nucleonics (BNC 575) multi-channel pulse delay generator (200 ps RMS jitter). The BNC triggered the camera at 1 Hz, and the discharges at 30 kHz.

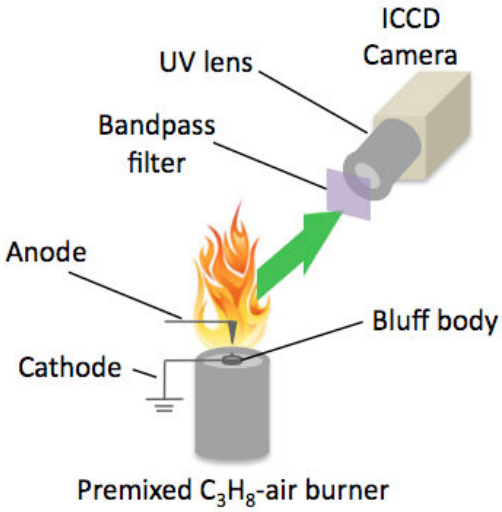

Figure 3.26 Chemiluminescence imaging setup for CH* and OH*, using bandpass filters centered at 310 nm and 430 nm, respectively.

3.7 Optical emission spectroscopy (OES)

3.7.1 OES Setup

Figure 3.27 shows the OES setup which comprises an Acton SpectraPro 2750i spectrometer (focal length 750 mm, grating of 1200 grooves/mm, blazed at 300 nm) fitted with a 1024x256-pixel ICCD camera (Princeton Instrument PIMax). An optical fiber (Acton LG-4550-020) is connected to the spectrometer through an imaging fiber adapter (Acton FC-446-010). The Full-Width-Half-Maximum (FWHM) of the slit function was 0.11 nm.

Two off-axis parabolic, UV-grade, MgF_2 coated aluminum mirrors of 50-mm diameter (Janos Technologies) were used to collect and focus the light into the optical fiber. A diaphragm placed before the collecting mirrors was used to adjust the solid angle to control the intensity of light. More details about the light collection system can be found in Pai (2006).

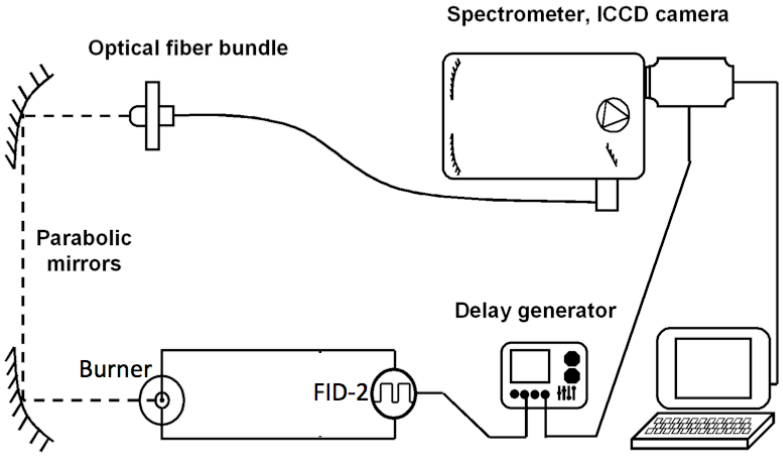

Figure 3.27 Experimental setup for optical emission spectroscopy.

3.7.2 Temperature determination

The gas temperature is one of the important factors required to understand the plasma-flame interaction processes, however it is quite delicate to measure time-resolved plasma temperature on nanosecond time-scales. Optical emission spectroscopy (OES) is one of the methods that can be used to measure the plasma temperature in certain conditions. Because the spectrum of certain molecules depends on the temperature, the temperature can be determined by fitting the measured spectrum with that calculated theoretically. For instance, the band spectra of the second positive system of nitrogen molecule can be used to determine the rotational temperatures of the $B^3\Pi_u$ and $C^3\Pi_g$ states. Thus, the gas temperature, which is assumed to be close to the rotational temperature, can be determined. This band of nitrogen has been extensively used in the plasma community to measure the plasma temperature (see for example [2, 18, 19, 22, 25]). Recently, Rusterholtz et al. [29] demonstrated that this technique provides indeed a good approximation of the gas temperature as long as the reduced electric field is higher than 10 Td, which is the case here for all cases investigated. In order to have sufficient OES signal, the measurements can only be done during the time when there is enough radiation from N_2(C-B) (i.e. during and shortly after the pulse, before the fast quenching processes by molecular oxygen deplete the population of the emitting states, and while E/N is greater than 10 Td).

In the 372-382 nm range, the N_2(C-B) (0,2) and (1,3) vibrational bands were identified (Figure 3.28). The spectra were calibrated in relative intensity with a tungsten lamp (Optronic Laboratories OL550) with spectral radiance values traceable to NIST standards. Figure 3.28 shows an example of experimental and calculated spectra with Specair software [66]. The best fit was obtained for a rotational temperature of 1500±100 K and a vibrational temperature of 3600±200 K.

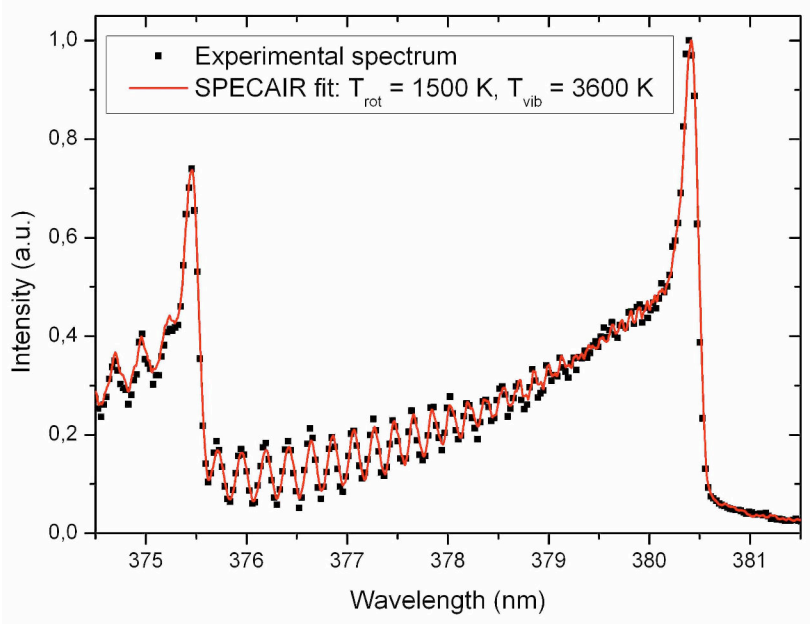

Figure 3.28 Experimental and Specair calculated N_2(C-B)(0,2) and (1,3) spectra.

In the plasma-assisted combustion dynamics experiments, we used NRP sparks to enhance the flame. The rotational temperature of $N_2(C)$ during the applied high-voltage pulses is close to the translational temperature of the neutral species [29]. We therefore assume that the gas temperature in the interelectrode region is given by the rotational temperature of $N_2(C)$.

The NRP sparks have a non-negligible thermal effect on the gas and they heat the gas in the inter electrode region. In order to determine the initial gas temperature without having been heated by the NRP sparks, we generated a weak glow discharge with a power less than 1 W and we measured the rotational temperature of $N_2(C)$ by the method explained above. Because the glow NRP discharges do not heat the gas [18], the temperature obtained is the initial gas temperature in the inter electrode region. The measured and calculated spectra shown in Figure 3.28 correspond to the case with only the glow discharge. The temperature in the recirculation zone without NRP discharges is thus determined as 1500 ± 100 K.

This temperature is significantly lower than the adiabatic flame temperature for a propane–air mixture with an equivalence ratio of 0.8 (2050 K). The explanations will be given in chapter 5.

3.8 Conclusion

In this chapter, we described the experimental setup used in this study and the general concepts of the experimental techniques. The three experimental facilities were presented. Then, we presented the electric energy measurement method for all the experiments. Special attention was paid to the issue of the external load resistance for FID pulse generators. Next, we detailed the optical diagnostic techniques used in this thesis, including schlieren imaging, OH planar laser induced fluorescence imaging, CH* and OH* chemiluminescence imaging, and optical emission spectroscopy. In addition, some practical issues have been addressed to optimize the fast schlieren system setup used to visualize the NRP discharges.

Chapter 4 Thermal and hydrodynamic effects of NRP discharges in air

4.1 Introduction

As presented previously in Chapter 2, the chemical reactions initiated by the NRP discharges induce thermal and hydrodynamic effects on air plasmas. For instance, NRP sparks can dissociate a large fraction of oxygen molecules and heat the gas by about 1000 K within a few tens of nanoseconds following each pulse [18, 67-69]. This effect has been attributed to the so-called ultrafast mechanism (see for example Popov [31]), which corresponds to the following two-step process:

$$N_2(X) + e \rightarrow N_2(A, B, C, a' ...) + e$$
$$N_2(A, B, C, a', ...) + O_2 \rightarrow N_2(X) + O + O$$

In the first step, which occurs during the high voltage pulse, nitrogen molecules are excited by electron impact to electronic states such as $A^3\Sigma$, $B^3\Pi$, $C^3\Pi$, $a'^1\Sigma$,... Next, these excited electronic states of N_2 undergo quenching by oxygen molecules, producing atomic oxygen and heat release. The dissociative quenching reactions of N_2 *A*, *B* and *C* occur immediately after the pulse, and proceed very quickly with characteristic times of 108, 0.9, and 0.6 ns respectively (at atmospheric pressure and room temperature). Accompanying the fast temperature increase, the pressure increases suddenly and pressure waves emerge from the discharge region and propagate through the surrounding air. The gas density *N* changes slightly within the first 50 ns, for example by about 10% when 50% of oxygen dissociates. Then, when the pressure returns to atmospheric behind the shock wave, the density decreases significantly because of the heating and the hydrodynamic expansion. The ultrafast mechanism described above is reported as strongly dependent on the reduced electric field (E/N) [33]. Thus, it is important to know the evolution of the hydrodynamic parameters (such as density, temperature and pressure) following a NRP discharge.

For these reasons, we have investigated the ultrafast heating and the hydrodynamic expansion following the spark. We imaged the NRP discharge region starting from 50 nanoseconds after each pulse in air at 300 and 1000 K. Then, we analyzed the developing shock wave and heated gas channel (see Section 4.2). A 1-D code was used to simulate the heating and the expansion process (Section 4.3). Numerical schlieren images were then generated for comparison with the experimental ones. The fraction of electric energy converted to heat and the initial temperature were determined from the comparisons (Section 4.4). Finally, experimental and numerical results are presented and discussed (Section 4.5).

4.2 Schlieren experiments

4.2.1 Schlieren images of NRP sparks in air at 300 K and 1000 K

Measurements were performed over a range of conditions. Here, four representative cases will be presented (see Table 4.1).

- Case 1: 1 kHz discharge in ambient air (300 K)
- Case 2: 10 kHz discharge in ambient air (300 K)
- Case 3: 1 kHz discharge in preheated air (1000 K)
- Case 4: 10 kHz discharge in preheated air (1000 K)

Table 4.1 Summary of the four cases investigated

	Gap distance	PRF	Electric energy per pulse	Air flow temperature T_{air}	Initial radius r_0[a]	V_{max}	V at I_{max}
Case 1	2 mm	1 kHz	0.15 mJ	300 K	200 μm	7.5 kV	6.1 kV
Case 2	2 mm	10 kHz	0.5 mJ	300 K	-	6.3 kV	3.5 kV
Case 3	4 mm	1 kHz	1 mJ	1000 K	380 μm	8.1 kV	4.1 kV
Case 4	4 mm	10 kHz	1.6 mJ	1000 K	480 μm	8.3 kV	3.4 kV

[a]The initial radius is measured from the schlieren image at 50 ns, assuming that it is nearly constant in the first instants. The measuring method will be presented in the following section. We could not obtain the radius of the initial heated channel for Case 2, because the heated air surrounding the gap prevented schlieren imaging of the initial heated channel.

The successive schlieren images for each case are shown in Figure 4.1. Cases 1 and 2 were investigated in a 300 K air flow environment with a gap distance of 2 mm, and Cases 3 and 4 were in a preheated air flow at 1000 K with a 4 mm gap distance. Case 4 is similar to the discharges studied by Pai et al [68], Stancu et al [6] and Rusterholtz et al [29, 69], but with more energy input (about 3 times that in [29, 69]).

From the general observation of the images in Figure 4.1, it appears that, first, the schlieren images taken in preheated air at 1000 K (Cases 3 and 4) have less contrast than those in air at 300 K because of the lower density of preheated air, thus the lower refractive index of light according to Equation (3.9). Second, with higher PRF, we note the presence of gas heated by the previous discharge pulses. In contrast, in the cases at low PRF the flow velocity seems to be sufficiently high to advect most of the gas heated by previous pulses between two consecutive discharges.

The first frame of each image set shows the cumulative effect of preceding discharges on the next discharge. It can be seen that the heated gas kernel produced by the discharge moves upward toward the anode, as a result of advection by the air flow, with some turbulence and diffusive expansion. At the time when the next discharge is fired (i.e. 1 ms in Cases 1 and 3 and 100 μs in Cases 2 and 4), it can be seen that the heated gas still occupies more than one half of the gap in Cases 1, 2 and 4. Although it is not obvious in Case 3 due to the low temperature gradient, we can infer from other cases that the gap is still occupied by heated gas ($T_0 > 1000$ K).

Starting from 50 ns, the heated channel can be identified in the schlieren images. The heated gas channel grows from a certain initial radius at 50 ns (about 0.2 mm for

Case 1, about 0.4 mm for Cases 3 and 4) and increases by about a factor 2 at 1 µs, before finally dissipating into the surrounding air. The shock wave emerges from the heated gas channel at about 0.5 µs. Its shape changes from a cylindrical to a spherical wave when its radius becomes comparable to the gap distance. As it propagates, the shock wave degenerates into an audible sound wave.

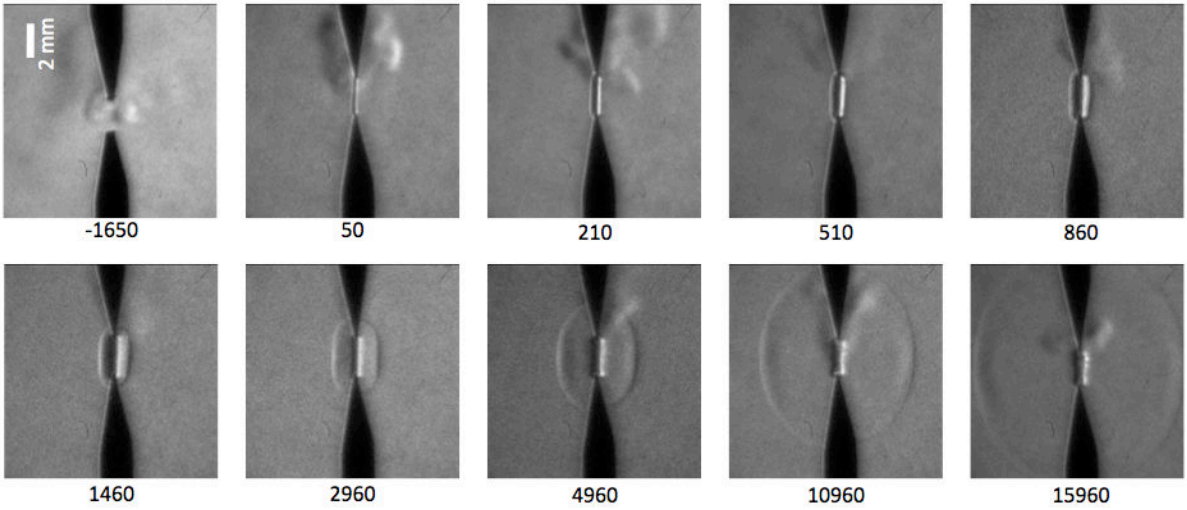

Case 1 (Gap distance = 2 mm, PRF = 1 kHz, $T_{air\ flow}$ = 300 K, $v_{air\ flow}$ ~ 1 m/s)

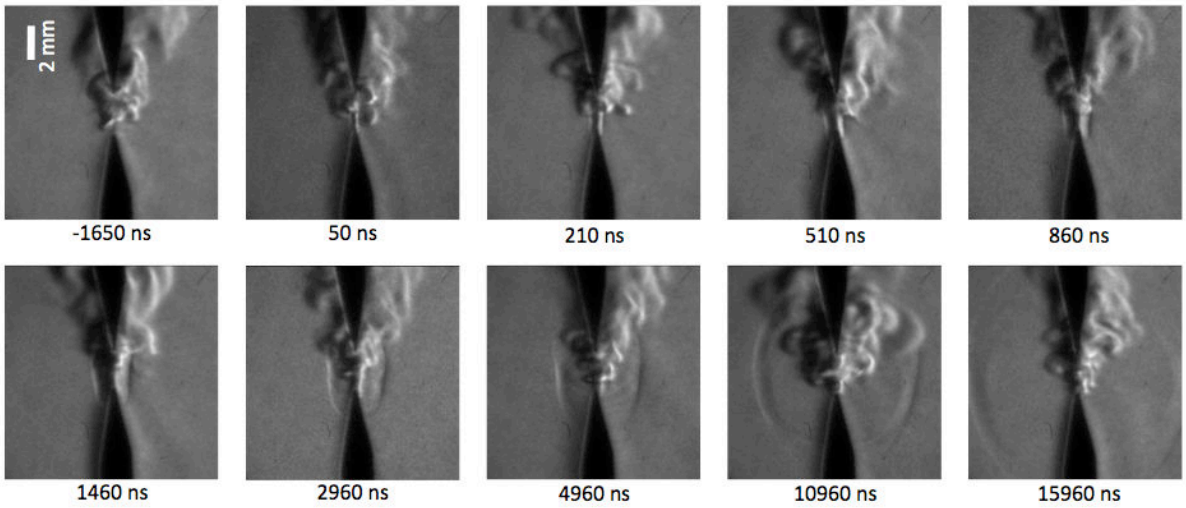

Case 2 (Gap distance = 2 mm, PRF = 10 kHz, $T_{air\ flow}$ =300 K, $v_{air\ flow}$ ~ 1 m/s)

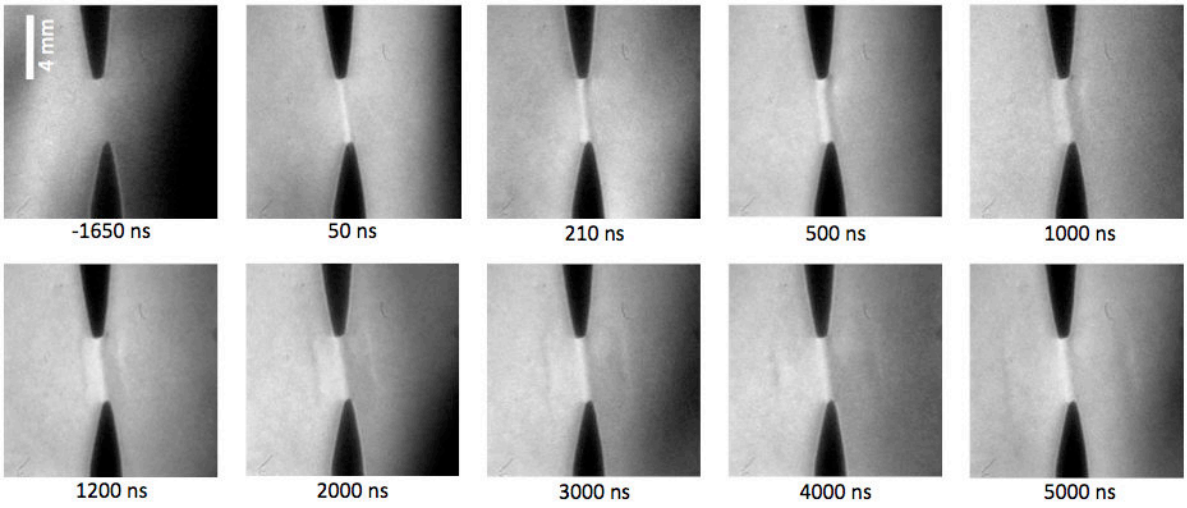

Case 3 (Gap distance = 4 mm, PRF = 1 kHz, $T_{air\ flow}$ =1000 K, $v_{air\ flow}$ ~ 1.5 m/s)

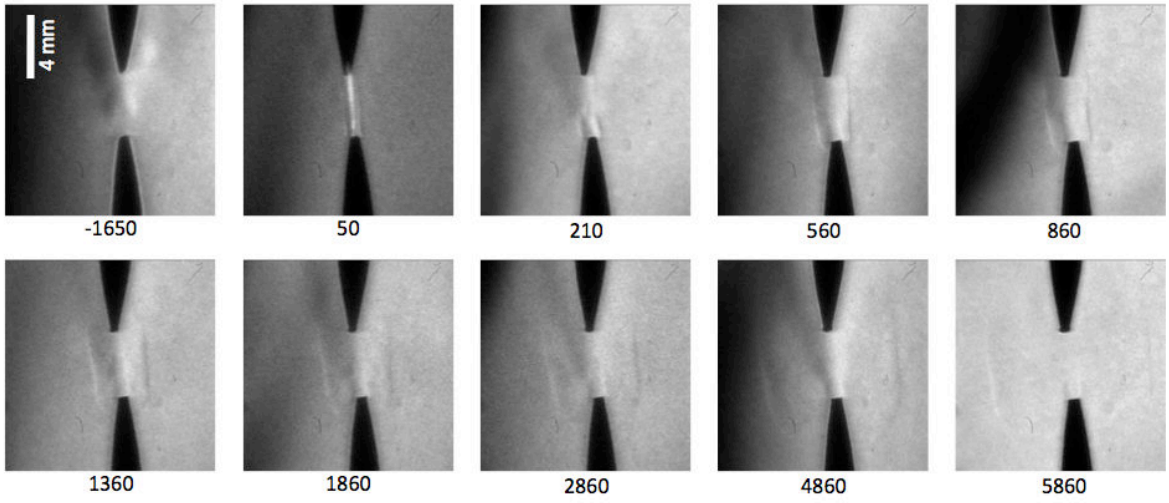

Case 4 (Gap distance = 4 mm, PRF = 10 kHz, $T_{air\ flow}$ =1000 K, $v_{air\ flow}$ ~ 1.5 m/s)

Figure 4.1 Successive single-shot schlieren images of NRP discharges in air. The exposure time is 20 ns. The numbers below the images represent the elapsed time (in ns) after discharge initiation. The minus sign indicates a time before the discharge.

In the next section, we present the post-treatment of the schlieren images obtained. The treatment is based on the contrast profile in the radial direction. Case 2 is excluded from the analysis because the heated air surrounding the gap prevented the extraction of the contrast profile in the heated channel.

4.2.2 Post-processing

The schlieren images obtained were post-processed to determine the hydrodynamic expansion parameters, i.e. the shock-wave and heated channel radii. Here we take the schlieren images for Case 1 at 210 and 2960 ns in Figure 4.1 as sample images to illustrate the post-processing procedure. The images are first rotated by a small angle so that the discharge channel appears vertically. They are then cropped to the inter-electrode region in Figure 4.2a and Figure 4.2c. The contrast profile in the

radial direction is then obtained with equation (3.13). Since the human eye is sensitive to differences in intensity, we define the radius based on the location of the black/white border in the image. From the first derivative curve of the contrast Figure 4.2b and Figure 4.2d, it can be seen that the black/white border corresponds to the negative peak of the contrast derivative. Here, we define the heated channel radius as the distance of the first negative peak from the center point, and the shock-wave radius as the distance of the second negative peak from the center point.

It is possible, however, that at short times ($t < 500$ ns) there is only one negative peak in the first derivative contrast curve as shown in Figure 4.2b. This is because initially the shock wave accompanies the heated channel growth and therefore we cannot distinguish them from each other in the schlieren images (see Figure 4.1). In this case, we assume that the shock wave has not separated from the heated channel and the first negative peak location defines the heated channel radius. At times between about 500 and 1000 ns, when the shock starts separating from the heated channel, it is possible to extract the experimental values of the shock-wave radius but not the heated channel radius. Thus in subsequent analysis, in particular in Figure 4.6, we could not obtain the radius of the heated channel between 500 and 1000 ns.

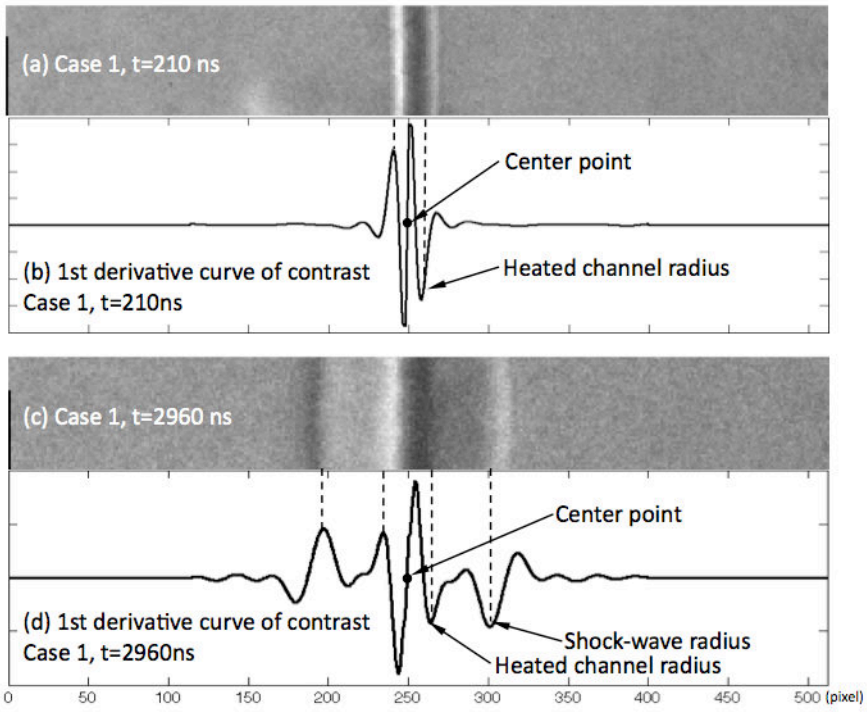

Figure 4.2 Determination of the shock-wave and heated channel radii from the images. (a) schlieren image at 210 ns, (b) derivative curve of contrast at 210 ns (c) schlieren image at 2960 ns, (d) derivative curve of contrast at 2960 ns.

4.3 Schlieren simulations

4.3.1 Hydrodynamic expansion model

The physical model of one-dimensional simulation was developed by Dr. Mikhail Shneider at Princeton University. The model is based upon the following assumptions:

(i) The equation of state is unchanged during the calculation period. As a result, the effect of dissociation on the ratio of specific heats is not taken into account.

(ii) A fraction of the electric energy is transferred into heating immediately. Thus, the power transferred into heating per unit volume (source term) can be expressed as:

$$Q = \eta W \tag{4.1}$$

where η is the fraction of electric energy transferred into heating immediately, and W is the electric power of the discharge per unit volume. Since the temporal current profile decays in less than 50 ns (see measured electrical waveforms in Figure 3.12), the energy is deposited in less than 50 ns, and therefore this assumption is reasonable.

(iii) The cathode sheath is negligible and the electric field distribution along the discharge channel between the electrodes is assumed to be uniform. This is also a valid assumption for spark discharges [68].

(iv) The electric field distribution is also uniform in the radial direction. Since the discharge channel has a radius less than 500 μm in all cases, this assumption will not change much the results.

(v) The discharge is axisymmetric.

(vi) The initial temperature T_0 is assumed uniform in the entire calculation domain.

With these assumptions, it is convenient to look for the solution in Lagrange's mass coordinates $dm = \rho r dr$ within the framework of the standard equations of one-dimensional gas dynamics [70]:

$$\begin{aligned}
&\frac{\partial r}{\partial t} = u, \\
&\frac{1}{\rho} = \frac{1}{2}\frac{\partial r^2}{\partial m}, \\
&\frac{\partial u}{\partial t} = -r\frac{\partial}{\partial m}(p+q), \\
&\frac{\partial \varepsilon}{\partial t} + (p+q)\frac{\partial}{\partial t}(1/\rho) = Q/\rho,
\end{aligned} \tag{4.2}$$

Equations (4.2) are solved together with the equation of state of the ideal gas in the channel:

$$p = (\gamma - 1)\rho\varepsilon = \frac{\gamma - 1}{\gamma}\rho h, \quad \gamma(T) = \frac{c_p}{c_v} \tag{4.3}$$

where p is the gas pressure, ρ is the gas density, γ is the specific heat ratio, q is a term related to the artificial viscosity, r is the radial distance, ε is the internal energy and h is the enthalpy per unit of mass of gas. In the general case, Q represents the influx and

losses of heat. For the conditions of our experiments, we can neglect the heat removed by thermal diffusion and radiation. The electric power deposition per unit volume is equal to the product of the current density and the electric field:

$$W = j(r,t)E(r,t) \tag{4.4}$$

where *j(r,t)* is the current density and *E(r,t)* is the electric field.

The current density in the plane perpendicular to the discharge is assumed to be Gaussian and defined as:

$$j(r,t) = \frac{I_{cond}(t)}{\pi r_0^2} e^{-\frac{r^2}{r_0^2}} \tag{4.5}$$

where r_0 is the initial channel radius. r_0 is taken as the heated channel radius at 50 ns measured from the schlieren image, assuming that the heated channel radius does not change in the first 50 ns due to the inertia of air.

The electric field is defined as:

$$E(r,t) = \frac{V(t)}{L} \tag{4.6}$$

where L is the distance between the electrodes. Figure 3.12 shows an example of the measured voltage and current waveforms *V(t)* and *I(t)* (see measurement procedure in Section 3.3) which are used as inputs to calculate the heating power by the discharge per unit volume, expressed as:

$$Q(r,t) = \eta W = \eta \frac{I_{cond}(t)V(t)}{\pi r_0^2 L} e^{-\frac{r^2}{r_0^2}} \tag{4.7}$$

The calculations were performed using an algorithm proposed by Brode [70] and used by many authors for modeling pulsed arcs [71-73] and laser spark dynamics [74]. The numerical solution of equations (4.2) and (4.3) is well discussed in the existing literature (see for example [70-72]).

4.3.2 Numerical schlieren images

The density profiles (Figure 4.3a) obtained by numerical simulation at different times are used to calculate the contrast profile (Figure 4.3b) using equations (3.12) and (3.17). For better comparison, we use the same average background grayscale level as in the experimental image to generate the numerical images (Figure 4.3c). The first derivative contrast curve is plotted to determine the heated channel radius and the shock-wave radius (Figure 4.3d), following the same method for the experimental images. The numerical schlieren images generated are compared with the experimental ones, which will be detailed in the following sections.

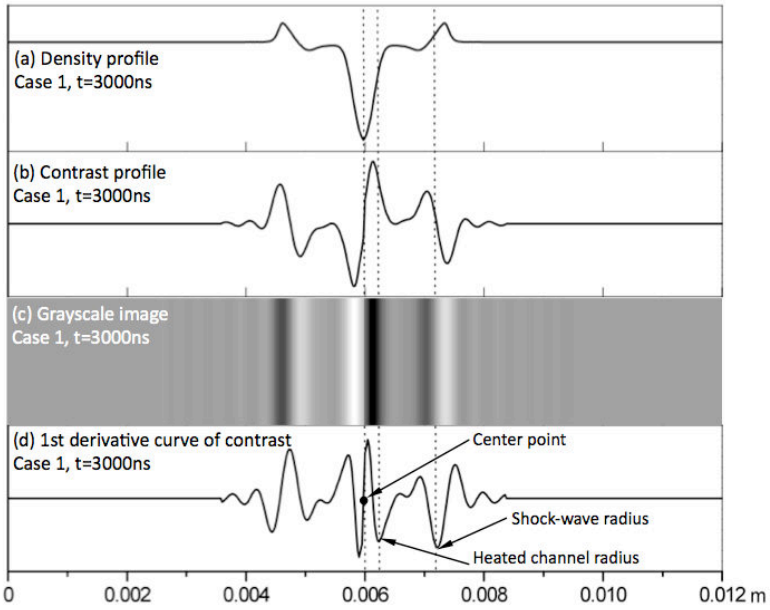

Figure 4.3 Typical numerical schlieren image (a) density profile (b) contrast profile (c) grayscale image (d) first derivative of contrast profile to determine radius

4.4 Comparison between experiments and simulations

4.4.1 Experimental schlieren image vs. numerical schlieren image

Examples of experimental and numerical schlieren images are shown in Figure 4.4. It can be seen that we have a very good agreement between the numerical and experimental schlieren images.

In Figure 4.5, we show the results of two series of simulations with different initial temperatures and different fractions of the heating energy. We see that the heated channel radius depends only on the amount of energy deposited, whereas the shock-wave radius depends on both the initial temperature and the energy. By virtue of these characteristics, we can determine η and T_0 through a comparison of the measured and computed results, detailed in the following subsections.

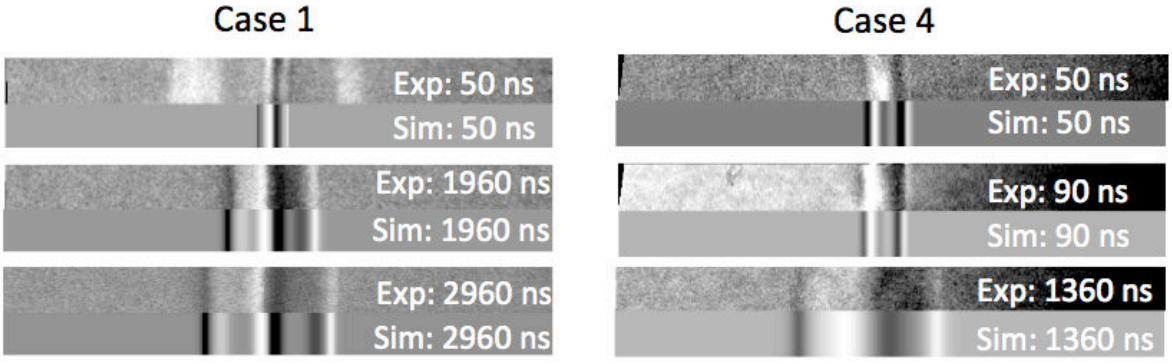

Figure 4.4 Comparison of schlieren and numerical schlieren images at different times.

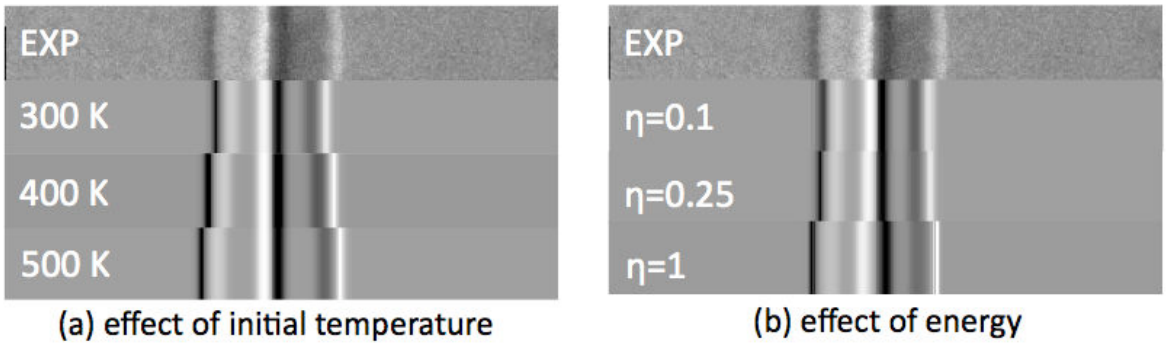

Figure 4.5 Comparison of experimental and numerical schlieren images for Case 1 at 2960 ns for (a) different initial temperatures (b) different fractions of the electric energy transferred into heating immediately. The initial radius r_0 for the simulations is taken at 200 μm. We see that the initial temperature affects the shock-wave radius but not the heated channel radius; and that the fraction of fast heating energy η affects both the shock-wave and heated channel radii.

4.4.2 Definition of the initial temperature

The initial temperature (i.e. the temperature at time '0') is higher in the inter-electrode region than that outside, due to the heating of previous pulses. This can be observed in the first frame of each image set in Figure 4.1. We see that the gas heated by the previous discharges has not been fully advected, and has a radius of less than about 2 mm in all cases investigated. The higher initial temperature in the center leads to the separation of the shock wave from the discharge channel at an earlier time, thus to a greater shock-wave radius. The wave propagation velocity is also greater in higher temperature gas. Then, when the shock wave leaves the heated gas region ($r > 2$ mm), its propagation slows down to a velocity corresponding to the speed of sound at the local temperature.

4.4.3 Fits of shock-wave and heated channel radii

It has been shown in Section 4.4.1 that the initial temperature affects the shock-wave radius but not the heated channel radius, and that the fraction η of energy into fast heating affects both the shock-wave and the heated channel radii. We can thus determine the fraction of heating energy and the initial temperature through the following procedure:

1) fit the heated channel radius to get η,

2) fit the shock-wave radius to get the initial temperature T_0 using η obtained in step 1).

In Figure 4.6, the experimental values of the shock-wave and heated channel radii are compared. We can see from the linear fit of the experimental data for $r > 2$ mm (dotted curves) that when the shock wave leaves the heated gas zone ($r > 2$ mm), the wave propagation slows down to the speed of sound corresponding to the value in ambient air. For instance, for Case 3, the slope of the dotted curve is measured to be

700±100 m/s, i.e. close to the value of the speed of sound in air at 1000 K (664 m/s). Note that we cannot determine precisely the temperature due to the experimental error. In Case 4, the slope was found to be 773±100 m/s, corresponding to the speed of sound at the temperature of 1500±500 K.

Inside the heated gas zone, where the temperature is assumed to be T_0, increasing η leads to larger heated channel radii (dashed curves), and increasing T_0 leads to larger shock-wave radii (solid curves). Note that in the numerical treatment, at early times when the heated channel boundary and the shock-wave front merge, it is difficult to extract shock-wave radius information. We thus extrapolated the solid curves at earlier times (dot-dash curves). It is then clear that increasing T_0 makes the shock wave separate from the heated channel at an earlier time. We then adjust the parameters η and T_0 to obtain good agreement with the experimental data.

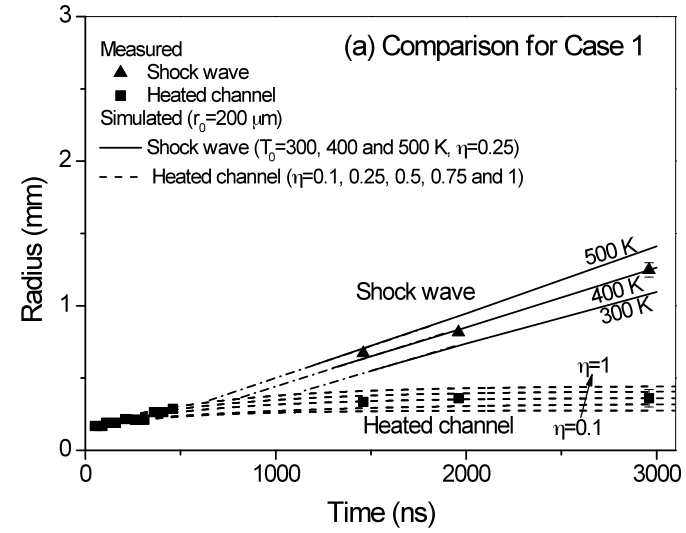

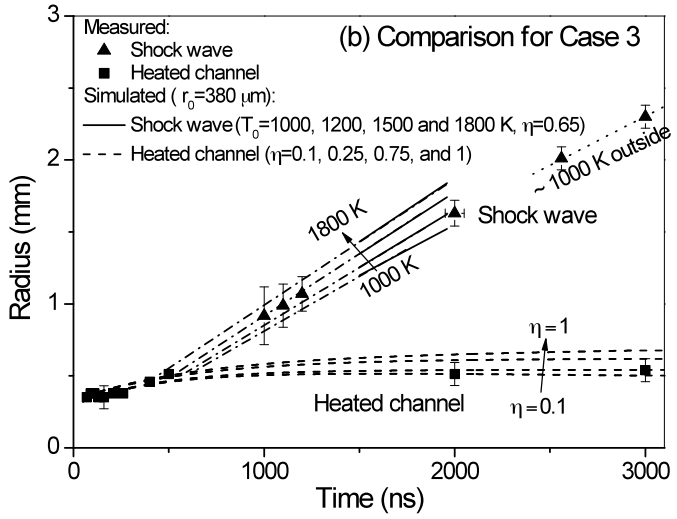

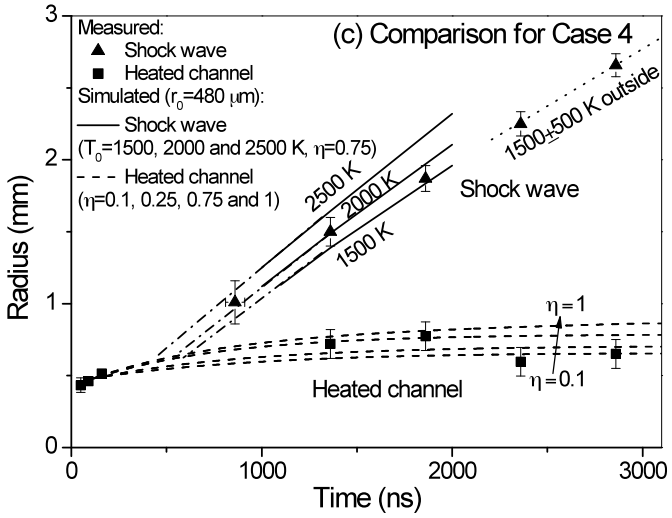

Figure 4.6 Comparisons of simulated and experimental shock-wave and heated channel radii for Cases 1, 3 and 4. Simulations are performed for various initial temperatures and η. The dash-dotted curves are extrapolated curves of the shock-wave radii. The dotted curves represent linear fits of the experimental data outside the heated gas zone, where the gas temperature is close to T_{air}

Despite the satisfactory fits, due to the experimental errors, we cannot determine very precisely the value of η only through the heated channel radius comparison. In fact, in the range of cases studied, the amount of initial energy deposition has little effect on the heated channel radius. In contrast, the amount of initial energy deposition has much effect on the deflection angle, thus on the value of the image contrast. By virtue of this effect, we can more accurately determine η through a comparison of the measured and computed contrasts, which will be detailed in the next subsection.

4.4.4 Fits of contrast profiles

The comparison of the contrast profiles is an effective way to determine the values of η and T_0 more precisely. As will be seen later, the contrast profile is a sensitive function of both η and T_0.

We continue to check the contrast profiles to verify η and T_0 obtained in steps 1) and 2) in the previous subsection. For instance, in Case 1, there exists a range of possible values of η obtained in step 1. Here we have selected four values: η = 0.1, 0.25, 0.5 and 0.75. With step 2, we find four different T_0 for each η selected. By doing so, we have four possible pairs of fitting parameters (η = 0.1, T_0 = 500 K), (η = 0.25, T_0 = 400 K), (η = 0.5, T_0 = 375 K), and (η = 0.75, T_0 = 300 K).

In Figure 4.7a, the contrast profiles, calculated with the four possible pairs of fitting parameters (η, T_0) obtained in steps 1 and 2, are compared with the experimental ones. The comparisons are made at a time when the shock wave has not yet left the heated gas region. For Case 1, the best fit is for η = 0.25 ± 0.1 and T_0=400 ± 50 K. By repeating the procedure for Case 3, the best fit is for η = 0.65 ± 0.15 and T_0=1350 ± 300

K (see Figure 4.7b). And for Case 4, the best fit is for $\eta = 0.75 \pm 0.25$ and $T_0=2000 \pm 500$ K (see Figure 4.7c). Only the shock-wave part of the contrast profiles is used for comparison. This is because the shock-wave intensity is sensitive only to the heat deposited at the first instants. After separation of the shock wave from the heated channel at about 600 ns, heating no longer affects the shock-wave intensity. Therefore, the comparison based on the shock wave is more reliable. In Case 3 and 4, it is interesting to note that the heated channel contrast is higher than the shock-wave contrast, meaning that the heating continues after the departure of the shock wave.

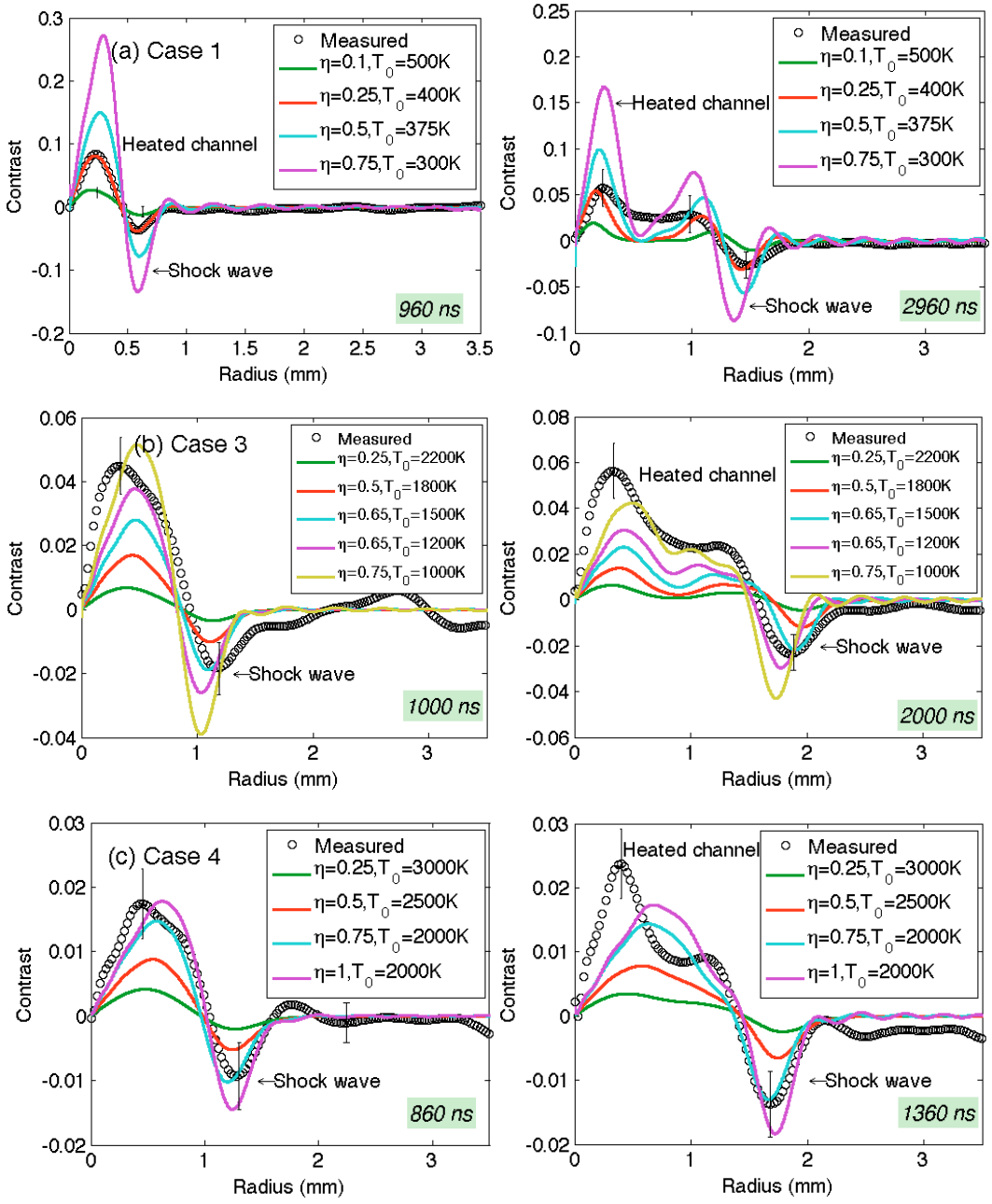

Figure 4.7 Comparison of contrast profiles in the shock wave to determine the initial temperature and the fraction of energy transferred into fast heating. For (a) Case 1, the best fit is for $\eta = 0.25 \pm 0.1$ and $T_0=400 \pm 25$ K. (b) Case 3, the best fit is for $\eta = 0.65 \pm 0.15$ and $T_0=1350 \pm 300$ K. (c) Case 4, the best fit is for $\eta = 0.75 \pm 0.25$ and $T_0=2000 \pm 500$ K.

4.5 OES measurements

To provide an independent confirmation of the initial temperature measured with schlieren, we also measured $T_{rot,0}$, the rotational temperature of $N_2(C)$ at time '0', with optical emission spectroscopy (OES) of the second positive spectrum of nitrogen, using the experimental setup described in Section 3.7, or in Ref [29]. We fit the (0,2) band of N_2(C-B) spectra at time '0' with Specair. The spectra for Cases 1, 3 and 4 are shown in Figure 4.8. It is found that, for Case 1, the best fit is for T_0=400 ± 50 K. For Case 3, the best fit is for T_0=1200 ± 200 K. And for Case 4, the best fit is for T_0=2000 ± 200 K. Thus, the initial temperatures measured by the two experimental techniques (schlieren and OES) are consistent.

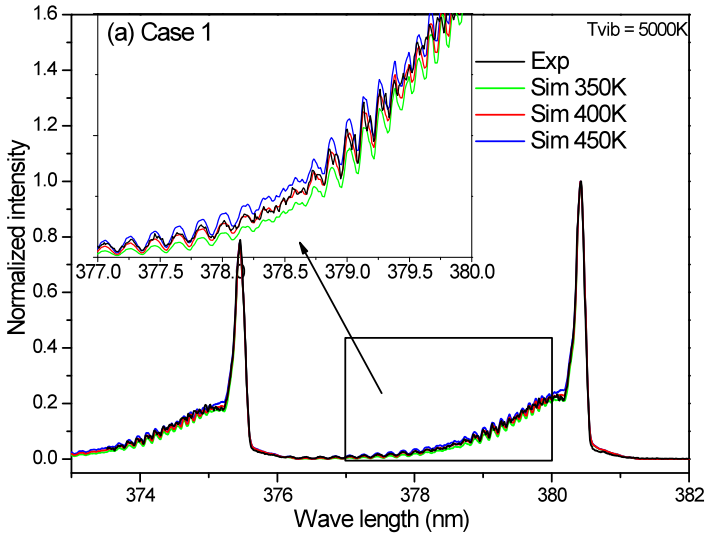

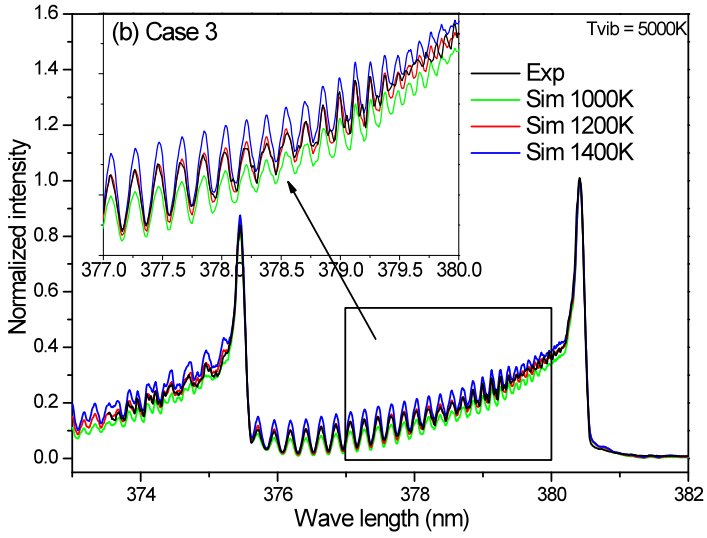

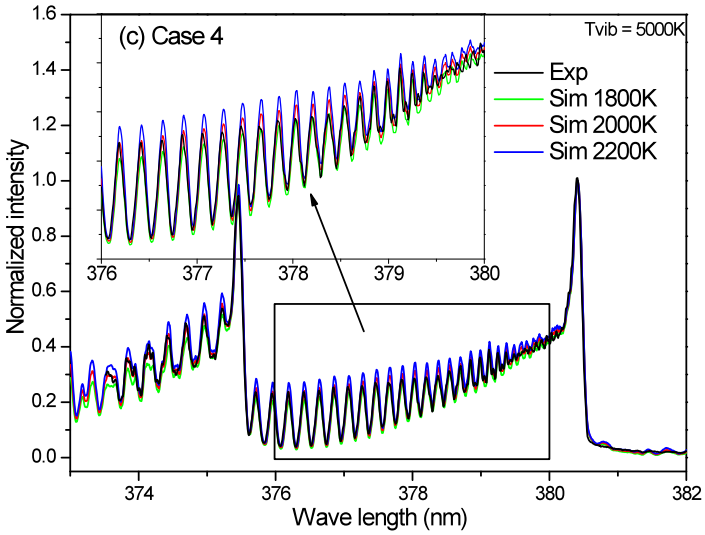

Figure 4.8 Experimental and Specair calculated N_2(C-B)(0,2) spectra. For (a) Case 1, the best fit is for T_0=400 ± 50 K. (b) Case 3, the best fit is for T_0=1200 ± 200 K. (c) Case 4, the best fit is for T_0=2000 ± 200 K.

4.6 Results and discussion

4.6.1 Initial temperature and fraction of energy transferred into fast heating

For nanosecond discharges, although all deposited energy eventually goes into gas heating (given that radiation losses, ionization, and dissociation are small), only a fraction goes into heating at the early stages (<50 ns). This early heating is caused by fast heating processes such as the dissociative quenching of N_2(B) and N_2(C), which occurs in about 20 ns [29]. Other heating processes need more time to occur. For example, the heating process corresponding to the dissociative quenching of the a' state and the A state of N_2 takes about 1 μs [31]. Also, the heating due to vibrational-translational relaxation is estimated to be at least 5 μs for the cases considered here (5 μs corresponds to Case 4 at about 2000 K and 10% mole fraction of atomic oxygen [68], and is calculated using Park's V-T relaxation rates [75]). If the heating occurred at these later times, the shock-wave radius profile would be shifted between 1 and 5 μs in Figure 4.6, which would clearly be in disagreement with the experimental results. Thus the observed shock wave is governed by heating processes lasting less than 50 ns, consistent with the ultrafast heating mechanism involving N_2(B) and N_2(C).

Table 4.2 summarizes the major results including the initial temperatures and heating fractions η for the three cases investigated. For the three cases investigated, the values of E/N listed in Table 4.2 are determined from the measured voltage at the peak of current and from the density taken at time '0' (since the discharge is isochoric during the first 50 ns, shown later in Figure 4.9b and Figure 4.10. It can be seen that η increases with E/N, from about 25±10% at 164 Td to 75±25% at 270 Td. The value measured in Case 1 can be compared with the numerical simulations at room

temperature presented in Ref [33]. According to Ref [33], η ~ 20% at E/N = 164 Td, which is close to our measured value of 25% ± 10%.

Table 4.2 Summary of the major results.

	Average power per unit volume	T_0 (schlieren)	$T_{rot,0}$ (spectroscopy)	(E/N) at I_{max}	η (schlieren)	η (simulation [33])
Case 1	600 W/cm^3	400 ± 25 K	400 ± 50 K	164 Td	0.25 ± 0.1	~ 0.2
Case 3	550 W/cm^3	1350 ± 300 K	1200 ± 200 K	225 Td	0.65 ± 0.15	-
Case 4	5500 W/cm^3	2000 ± 500 K	2000 ± 200 K	270 Td	0.75 ± 0.25	-

We can compare the present results with those obtained using OES in Ref [29] for the following conditions: pulse duration 10 ns, gap distance 4 mm, PRF 10 kHz, air flow temperature 1000 K. In Ref [29], the initial temperature measured by OES was 1500 K and the temperature 20 ns after the pulse initiation was about 2400 K, owing to the ultrafast heating mechanism. This case is close to Case 4, except that the average power per unit volume (2.26 kW/cm^3) is about 50% of the average power per unit volume deposited in Case 4. The initial temperature increase, about 500 K, is also about 50% of the initial temperature increase for Case 4 (from 1000 K to 2000 K). Thus these results are consistent. Furthermore, in Ref [29] the energy transferred into fast heating was determined to be about 21% for a value of E/N (at I_{max}) of 120 Td. This is consistent with the value of 25% measured here in Case 1 for E/N (at I_{max}) = 164 Td.

It is also interesting to compare the present results with the experimental observations of Messina et al [76] who studied the temperature evolution in room air excited by a 100-ns pulsed discharge. This discharge had the following characteristics: 3 mm gap, E/N (at I_{max}) = 140 Td, volumetric energy per pulse about 1.2 J/cm^3, volumetric average power 120 W/ cm^3. This case is fairly close to Case 1 in terms of E/N, volumetric energy per pulse and volumetric average power, and therefore the initial temperature and overall heating should be close to those in Case 1. Indeed, they obtained an initial temperature of 300 K and a temperature rise of less than 200 K at t < 1μs. This low temperature increase is consistent with the low temperature increase obtained in Case 1.

4.6.2 Temporal and spatial profiles of temperature, pressure and density

In this section, we will now examine the temporal and spatial behavior of the discharges studied for the three cases using the numerical model of Section 4.3.1. Figure 4.9 shows the calculated temporal evolutions of the hydrodynamic parameters (temperature, density and pressure) in the center of the discharge for the three cases. For the case with the highest energy transferred into heating (Case 4), the temperature increases by about 2000 K in less than 50 ns, and the density decreases by more than 50% within 1 μs. After that time, the density increases by about 5%. For the case with the lowest energy transferred into heating (Case 1), the temperature increase is about 220 K in less than 50 ns, and the density decreases by more than 30% within 1 μs. Thus, the change of density was significant for all cases investigated.

In all cases, the pressure returns to 1 atm within about 0.5 μs. The temperature and density reach steady state within 1 μs. These times are consistent with the hydrodynamic characteristic time of a channel of radius r_0:

$$t_c = \frac{r_0}{c} \tag{4.8}$$

where c is the speed of sound. The hydrodynamic characteristic times for cases 1, 3, and 4 are 0.50, 0.52 and 0.54 μs respectively.

Figure 4.10 shows the calculated temperature, density and pressure profiles in the radial direction from 50 ns to 3 μs for each of the three cases. We notice the fast depletion of the density in the heated channel and that the shock waves form at the edge of the heated channel before propagating toward the surrounding air. The amplitude of the shock waves decreases slightly as they propagate. The maximum pressure increase in the shock waves is only about 20%. As a result, those shock waves are very weak and propagate at a velocity close to the speed of sound, at the local ambient air temperature. The maximum temperature increase in the shock waves is less than 100 K in all cases, with the highest value for Case 4.

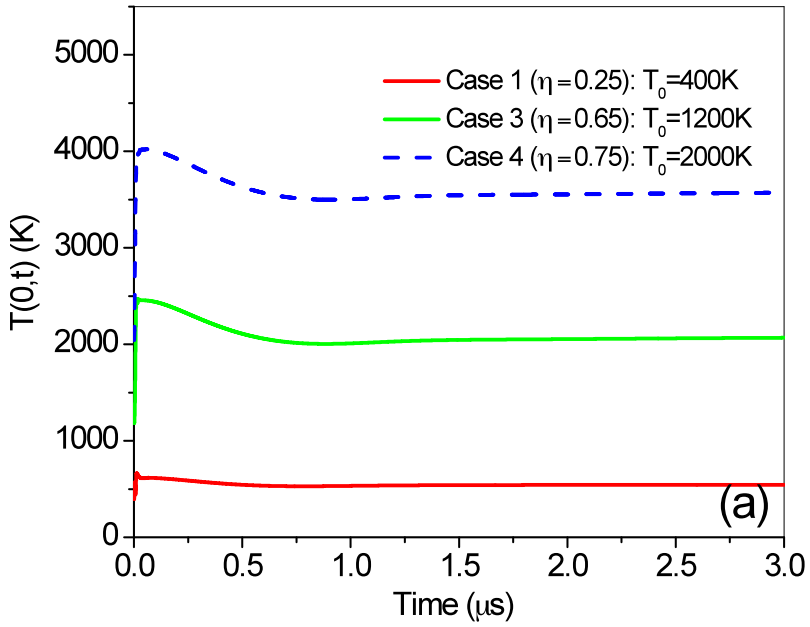

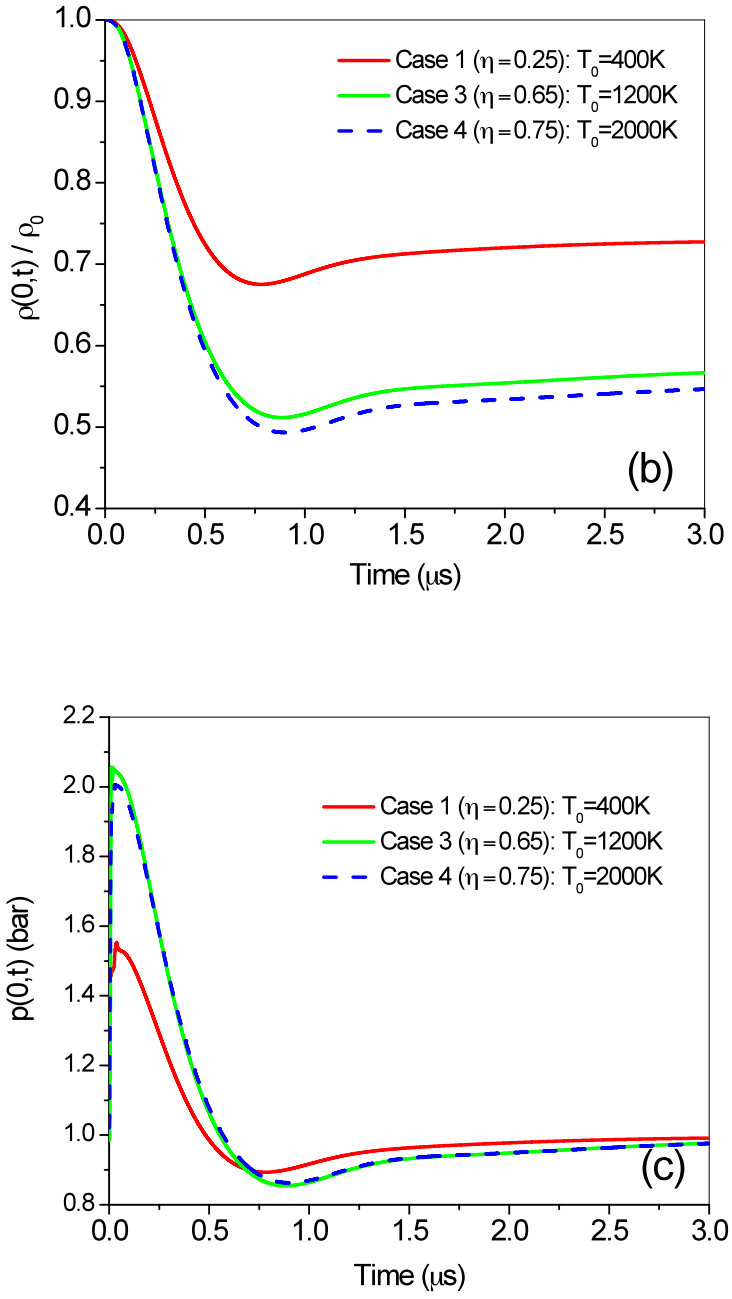

Figure 4.9 Temporal evolution of (a) temperature, (b) density and (c) pressure in the center of discharge.

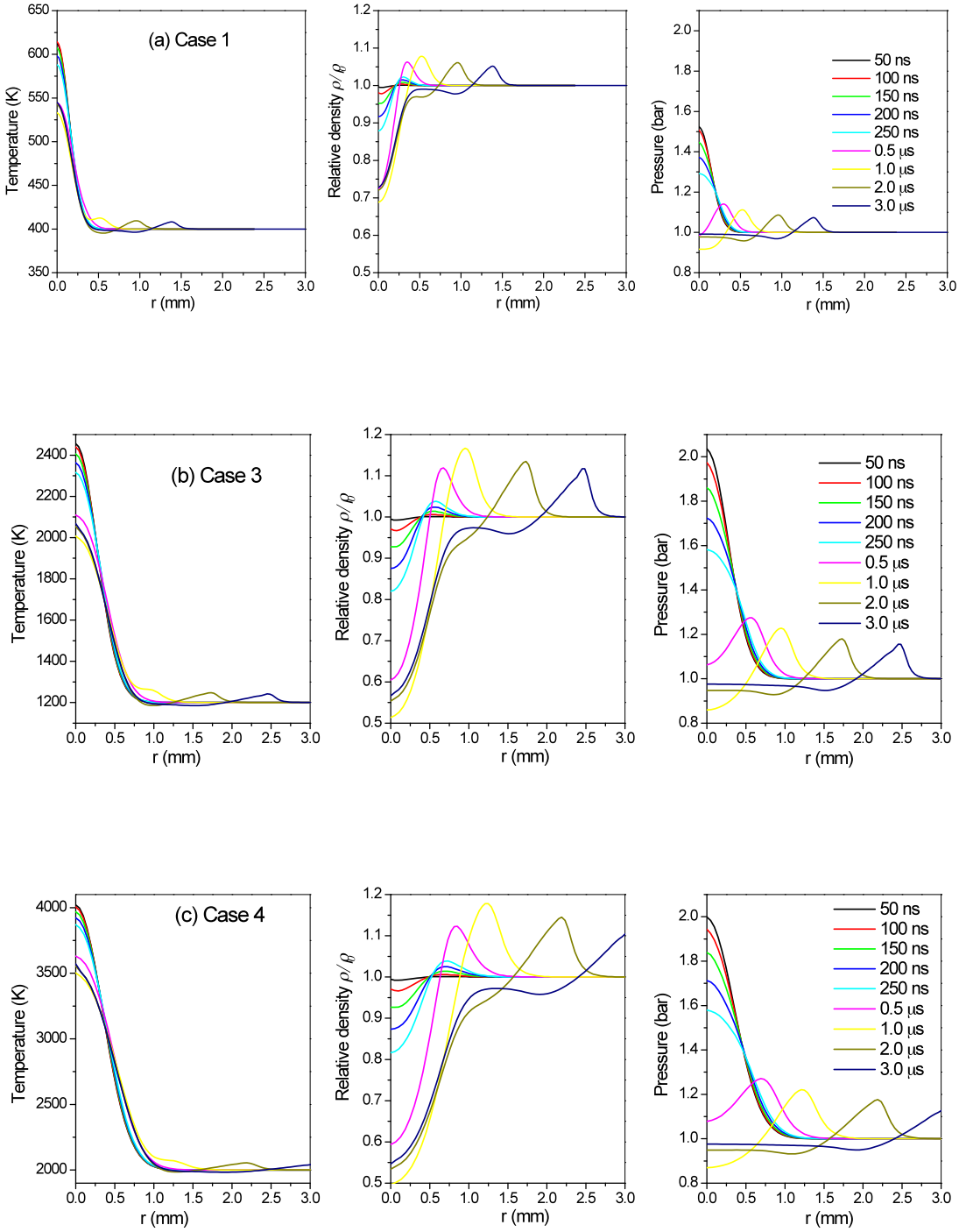

Figure 4.10 Calculated temperature, density and pressure profiles at different times for (a) case 1, (b) case 3, and (c) case 4.

4.7 Conclusion

The temporal evolution of the shock-wave and heated channel radii in a nanosecond repetitively pulsed discharge were measured using a fast schlieren technique and were compared with numerical results. The initial temperature and the fraction of energy transferred into heating were determined by fitting the contrast profiles of numerical schlieren images to the experimental ones. The contrast profiles were found to be a much more sensitive way of determining the initial temperature and fraction of energy transferred into heating than the fitting of shock-wave and heated channel radii.

The ultrafast temperature increase within 50 ns after the pulse is proportional to the product of the volumetric energy per pulse and the fraction of energy transferred into ultrafast heating. It was shown that the fraction of energy transferred into ultrafast heating strongly depends on the E/N value. At high E/N values (270 Td), 75±25% of the energy is transferred into heating in 50 ns. At lower E/N values (164 Td), this fraction is about 25±10%, in agreement with the numerical (25%) and experimental (21±5%) values reported in the literature [29, 33].

Before each pulse, the gas temperature in the gap increased due to heating by the previous pulses. This increase is proportional to the average power per unit volume deposited by the discharges, and varied from 100 to 1000 K in the cases studied. In NRP discharges, heating by previous pulses must be carefully accounted for because it leads to an increased value of E/N, which in turn produces high heating within a few 100 ns. In the cases we reported, over the range 164 to 270 Td, the measured and predicted temperature in a channel of about 1-2 mm diameter varied from 500 to 4000 K.

The present measurements thus provide a quantification of the thermal and hydrodynamic effects of nanosecond repetitively pulsed discharges in air. In particular, they confirm the measured ultrafast temperature increase that was observed by emission spectroscopy of the first and second positive spectra of nitrogen [29]. They also provide a significant improvement over previous methods to quantitatively measure the initial temperature and the fraction of energy deposition into heating.

The model could be improved, for example by taking into account the dissociation of nitrogen, which not only change the kinetics, but also influence the Gladstone-Dale coefficient which is smaller for N_2 than for N (by a factor of 0.78). Taking into account chemical kinetics can be also beneficial. The experiment can also be improved by using a spatially static, temporally stable light source (i.e. a powerful diode emitting incoherent light) in order to reduce experimental error.

Chapter 5 Characterization of NRP ignition kernel and application to lean mixture ignition

5.1 Introduction

As presented previously in Chapter 2, the NRP discharges have positive impact in terms of reducing ignition delay [3], thanks to a combination of thermal and chemical effects. Since it is difficult to separate experimentally these effects, numerical simulations are needed to understand and to optimize the effects of NRP discharges on ignition delay time and combustion time. The basic entry parameters for simulation codes are the initial ignition kernel radius, as well as the temperature and concentrations of active species (e.g. atomic oxygen, hydroxyl radical) at the end of the discharges. Among these parameters, the thermal effects of NRP discharges have been discussed in Chapter 4 of the thesis, as well as by other authors investigating the fast heating mechanism [18, 29, 31, 32]. The atomic oxygen concentration has been measured through Two-photon Absorption Laser-Induced Fluorescence (TALIF) [6, 8] or possibly deduced from absolute Raman measurements of the O_2 density [32]. The OH radicals have been measured by LIF and Coherent Anti-Stokes Raman Spectroscopy (CARS) [77]. On the other hand, the NRP plasma kernel radius has been determined only in a few cases, for instance using emission spectroscopy of the N_2 B and C states [19, 29]. Detailed investigations of the ignition kernel radius as a function of pressure and energy is therefore desirable in order to better understand the ignition process of nanosecond pulsed spark ignition, as well as to provide a database for simulations. This is the object of the present chapter.

In this chapter, we first present a characterization study of the ignition kernel. This consists in characterizing the initial spark radius (Section 5.2.1), and in its following development to providing a database for simulation validation (Section 5.2.2). Then we present an application of NRP discharges to lean mixture ignition (Section 5.3), where a comparison with a conventional ignition coil (Audi) will be made.

For reasons of clarity, we define the plasma kernel and ignition kernel as the kernel created by the discharges in air and in propane-air mixture, respectively. At early times (< 1 ms), as we will see later, the plasma kernel development is almost identical to the ignition kernel.

5.2 Characterization of ignition kernel

In this section, we characterize the second stage of the ignition process. As mentioned previously, the nanosecond pulsed spark ignition process involves generally

three stages. The first stage, which occurs on a time scale of tens of nanoseconds, involves electric breakdown followed by the formation of a narrow spark channel containing a non-equilibrium plasma. The electric energy is spent in various collisional processes including elastic, rotational, ionization, dissociation, vibration and electronic excitation processes by electron impact. At high values of reduced electric field (>100 Td), a dominant fraction of the energy is transferred almost instantaneously into the translational modes through fast heating processes that proceed via dissociative quenching of N_2(A,B,C,a',...) by molecular oxygen [29, 31, 33, 78]. As a result, at the end of the first stage, the temperature is increased by up to a few thousand Kelvin, molecular oxygen is dissociated (up to 50%) to produce atomic oxygen, and the pressure increase instantaneously with the temperature increase. However, the density changes little because of the inertia of the air (isochoric energy deposition) and because the overall degree of dissociation (i.e. the total number of particles in the discharge volume) does not vary much (see Chapter 4). For instance, even if 50% of O_2 dissociates, the total number of particles increases by only 10% since O_2 represents only 20% of the air composition.

The second stage, which occurs on a time scale of microseconds, involves first the expansion of the heated channel and second, the subsequent growth of the ignition kernel due to thermal and species diffusion. The hydrodynamic expansion of the heated channel takes place from the end of the first stage (~ tens of nanoseconds) to about 1 µs, and is followed by the formation of shock waves at the boundary of the heated channel. During that time, at the center of the gap, the gas density decreases and finally reaches steady state. The temperature and pressure also reach steady state in about 1 µs. Then, from about 1 µs, the ignition kernel grows due to diffusion.

In the case of ignition by multiple nanosecond pulses, the second pulse causes air breakdown again, and deposits additional energy. This process, analogous to the first step, is followed by a further expansion of the ignition kernel. The process continues until the last pulse is fired, and the ignition kernel thus develop in a transient way.

Lastly, the third and final stage corresponds to the ignition of the combustible gas mixture surrounding the ignition kernel to produce, under favorable conditions, a self-sustained propagating flame. The ignition occurs on a time scale of milliseconds and the flame propagates on a time scale of tens of milliseconds, in the constant combustion chamber used in this thesis.

The first stage of the nanosecond pulsed spark ignition process is very similar to the first stage following a nanosecond pulse in air, because in the lean mixture we have used (Φ=0.7) the mole fraction of propane is only 2.9%, and the cross-section of effective electron impact of propane (~1.3×10^{-19} m^2 at 15 eV) is close to that of nitrogen (~ 1.2×10^{-19} m^2 at 15 eV) [79]. The chemistry of NRP discharges in air has been investigated by Pai, Rusterholtz, etc., and the thermal and hydrodynamic effects of NRP discharges in air were presented in the previous chapter.

The second and third stages of the ignition process have been extensively studied

for ignition with conventional igniters [10, 36, 80, 81]. However, little is known for these stages when using nanosecond pulsed sparks.

In this section, we begin by characterizing the initial spark radius for the second stage of the ignition process. Then, we characterize the subsequent ignition kernel development. Quantitative or semi-quantitative models are used to analyze this ignition kernel development.

5.2.1 Initial spark radius

In this thesis, the initial spark radius is defined as the thermal radius of the heated channel viewed by the schlieren technique at the end of the energy deposition phase. In our nanosecond discharge, the energy deposition finishes in less than 50 ns (see for example the voltage and current curves in Figure 3.13). The initial spark radius is measured from the single-shot schlieren image at 50 ns after the pulse initiation. We assume that it does not change between 0 and 50 ns. This assumption was justified in Chapter 4, where we showed that the density remained the same at the first instants. The schlieren setup described in Section 3.4.2 has been used to visualize the NRP discharges and the plasma kernel. The post-processing procedure to measure the heated channel radius was presented in Chapter 4.

Effect of pressure (1-20 bar)

The FID-2 pulse generator was used to create nanosecond spark discharges in pure air up to 20 bars, with a constant pulse energy deposition of 6.2 mJ. Discharges were also created in a propane-air mixture of equivalence ratio 0.7 at 1 and 5 bar, in order to determine how the addition of propane affects the initial spark radius. The results are plotted in Figure 5.1, where each symbol represents the average value of five independent measurements.

We first observe that the initial spark radius in the lean mixture is the same as in pure air. This is not surprising because the mole fraction of propane is only 2.9%.

It can be seen also from the plot that the spark radius decreases nonlinearly as the pressure increases, from about 250 μm at 1 bar to about 125 μm at 20 bar. At pressures above 10 bar, the initial spark radius reaches an asymptotic value of about 125 μm.

In Ref [82], the streamer radius of a negative streamer discharge was measured at pressure from 0.5 bar to 1 bar, with a similar nanosecond discharge. The radius decreases from about 2.5 mm at 0.5 bar to about 250 μm at 1 bar. Thus the values obtained at 1 bar are consistent.

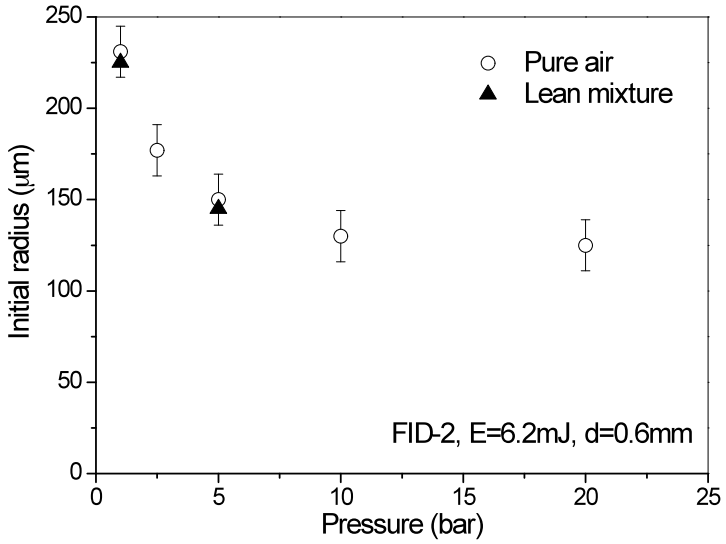

Figure 5.1 Effect of pressure on the initial radius. FID-2, 50-Ω in series, single pulse, electric energy E=6.2 mJ, gap distance d=0.6 mm, propane-air mixture Φ=0.7 or pure air, T=300 K

Effect of energy (1.5-6.2 mJ)

The electric energy deposited in the plasma is varied to see its effect on the initial spark radius. We have used two pulse generators in this purpose: FID-4 with 150, 100 or 50-Ω in series to deposit about 1.5, 2 or 3 mJ per pulse, respectively, and FID-2 with 50-Ω in series to deposit 6.2 mJ per pulse. The results are shown in Figure 5.2, where each symbol represents the average value of five independent measurements. Discharges have also been created in the lean mixture at 1 bar, in order to verify that the initial spark radius is the same.

These results confirm that the addition of propane with a mole fraction of 2.9% do not affect the initial spark radius. Therefore the experimental data obtained from pure air are appropriate to characterize the ignition of the lean mixture.

We can also see in Figure 5.2 that with the increase of pulse energy, the initial spark radius increases nonlinearly, and reaches an asymptotic value at high pulse energy.

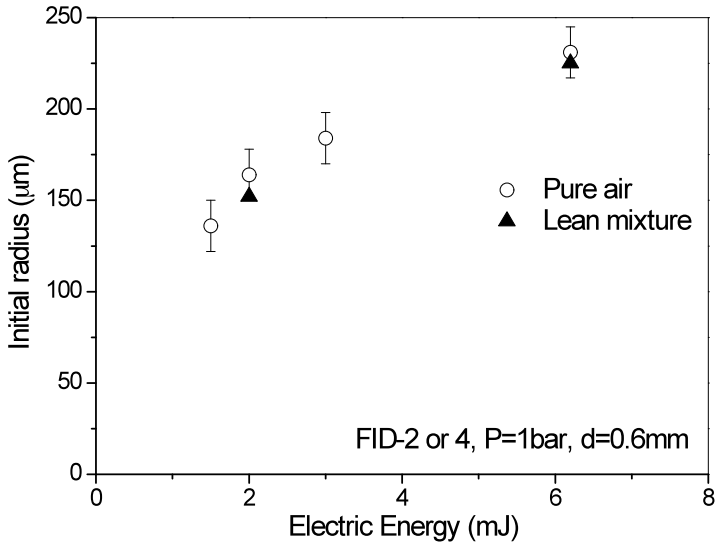

Figure 5.2 Effect of energy on the initial radius. FID-2 or 4, 50 or 100-Ω in series, single pulse, gap distance d=0.6 mm, 1bar propane-air mixture Φ=0.7 or pure air, T=300 K

Analytical treatment

The initial spark radius is determined by the electric field, the gas properties in the gap, and the electrodynamics of the pulse. We present next two simple analytical formulas to estimate the initial spark radius. Comparisons with experimental data will be given.

1) Estimation from streamer radius

We assume here that the spark radius at 50 ns is the same as the streamer radius. In the literature [83, 84], the streamer radius is estimated as the half-width of the electron density distribution, given by the following empirical expression:

$$r = 2\sqrt{0.693Dt} \tag{5.1}$$

where D is the diffusion coefficient along the radial direction (for nitrogen gas at atmospheric pressure and room temperature, D = 1800 cm^2s^{-1}) and t is the elapsed time after the release of the seed electrons. Using this equation, the initial radius is calculated at 158 μm, which is of the same order of magnitude as the experimental radii measured in this study.

Certainly, the diffusion coefficient depends on the temperature and the pressure. On the one hand, increasing the energy deposited in the gap leads to a higher temperature and a greater diffusion coefficient, thus a greater streamer radius. This effect is observed experimentally in Figure 5.2, but is difficult to quantify from the simulations presented in Chapter 4, since the temperature increase depends on the initial radius itself. On the other hand, increasing the pressure can lead to a smaller streamer radius. The pressure effect can be quantified because empirically, at constant temperature, we have [85]:

$$\frac{D_{p_1}}{D_{p_2}} = \frac{\rho_{p_2}}{\rho_{p_1}} = \frac{p_2}{p_1} \tag{5.2}$$

where p_1 and p_2 denote pressures 1 and 2, respectively. With this simple model, the pressure dependence of the initial spark radius is thus given by:

$$r = 2\sqrt{0.693\frac{D}{p}t} \tag{5.3}$$

where D =1800 cm^2s^{-1}, t = 50 ns. As will be seen below (subsection 3), this dependence qualitatively reproduces the trend observed in the data shown in Figure 5.1, but the temperature dependence is not taken into account.

2) Estimation from heated channel radius between 1-5 μs

In the previous chapter, we showed that at 50 ns after the pulse initiation, the temperature and pressure have reached the maximum value, however, due to the inertia of the neutral molecules, the density does not have enough time to change. In such a hydrodynamic non-equilibrium, between 50 ns and 1 μs, the density profiles change slowly, inducing an expansion of the heated channel (by a factor of about 2). The temperature, pressure and density reach steady state at about 1 μs, before the diffusion effects influence the channel radius at about 5 μs. Between 1-5 μs, the heated channel radius is nearly constant. If one knows the heated channel radius at a time between 1-5 μs, then the spark radius at 50 ns can be inferred, assuming that the heated channel between 50 ns and 1 μs expands by a constant factor σ. This expansion factor was measured experimentally for cases with an initial temperature of 300 K and with different energy input at 1 and 5 bars. It is found that this factor is quasi-constant with a value of 2.0±0.1.

We can estimate the heated channel radius at time t (1μs<t<5μs) after the pulse initiation, when the pressure returns to p_0 [27]. The increase in the enthalpy per unit discharge length is approximately:

$$\pi r(t)^2 p_0 \frac{\gamma}{\gamma - 1} \tag{5.4}$$

where γ is the ratio of specific heats and p_0 is the ambient pressure. The energy input per unit discharge length is:

$$\frac{Q(t)}{d} \tag{5.5}$$

where Q is the energy deposited into gas heating and d is the gap distance. The energy conservation law leads to equality of these two terms. We thus obtain:

$$r(t) = \sqrt{\frac{\gamma - 1}{\pi\gamma}\frac{Q(t)}{p_0 d}} \propto \left(\frac{Q(t)}{p_0 d}\right)^{1/2} \tag{5.6}$$

The initial spark radius is then:

$$r_0 = r(t = 50ns) = \frac{1}{\sigma} \cdot r(1\mu s < t < 5\mu s) = \frac{1}{\sigma}\sqrt{\frac{\gamma - 1}{\pi\gamma}\frac{Q(t)}{p_0 d}} \tag{5.7}$$

3) Comparison of analytical models with experimental data

The first model (called "Streamer-radius model") only accounts for the effect of pressure, whereas the second one (called "Heated-channel-radius model") accounts for both the effects of energy and pressure. Using (5.7), letting σ=2.0±0.1 and assuming that 25% of the electric energy is transferred into heating in the first 50 ns (25% corresponds to the results of Case 1 at room temperature investigated in Chapter 4), we can plot the initial spark radius as a function of energy (Figure 5.3) for Heated-channel-radius model, and as a function of pressure (Figure 5.4) for both Streamer-radius model and Heated-channel-radius model. The calculated curves are compared with the experimental data.

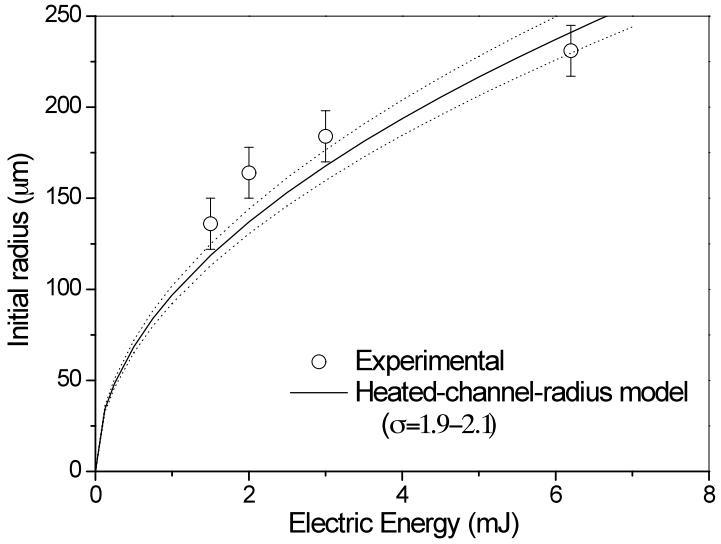

Figure 5.3 Analytical and experimental initial spark radii versus energy input. The fraction of energy transferred into heating is assumed to be 25% and the expansion factor σ=2.0±0.1. The pressure is 1 bar. The dotted curves represent the upper and lower bounds caused by the variation of the expansion factor.

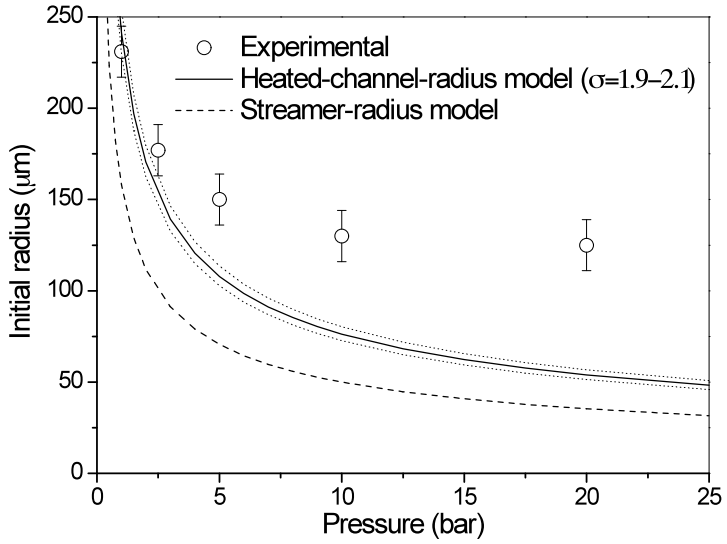

Figure 5.4 Analytical and experimental initial spark radii versus pressure. In Heated-channel-radius model, the fraction of energy transferred into heating is assumed to be 25% and the expansion factor σ=2.0±0.1. The dotted curves represent the upper and lower bounds caused by the variation of the expansion factor.

We see from Figure 5.3 that, at 1-bar pressure, the analytical approximation based on Heated-channel-radius model agrees fairly well with the experimental results. However, from Figure 5.4 we see that at high pressures, there is a large discrepancy between the experimental data and the analytical approximations. Both analytical expressions underestimate the initial spark radius. We note that in Heated-channel-radius model the analytical treatment is too simple to take into account the pressure effects. And the discrepancy between Streamer-radius model and the experimental results can be explained by the ultrafast heating during the pulse, because the air in the gap is suddenly heated in tens of nanoseconds, the diffusion coefficient D increases, thus the spark radius increases according to (5.3). Taking into account of ultrafast thermal effects will improve the Streamer-radius model, but nevertheless the model already well captures the qualitative trends.

5.2.2 Ignition kernel development

After the formation of the initial heated channel with a certain radius, the heated channel growth is determined by the hydrodynamic expansion (50ns-1μs), the diffusion processes (>8μs) and the energy deposited by the subsequent pulses. At early times (50 ns -1 ms) when the oxidation of propane is not strong enough to make the flame self-sustained, the ignition kernel development is almost identical to the plasma kernel development in air [86]. As we will see later, at 1-bar pressure, the reactions of oxidation of propane occurs at a very early time, but they are not strong enough to make a difference in terms of kernel radial extent. Diffusion also has a weak effect on the kernel development, in comparison with the contribution of the energy deposited in the

plasma by the NRP discharges. Thus the kernel growth is mainly controlled by the energy deposited by the subsequent discharges.

We thus studied the plasma kernel development in air using the fast schlieren technique. Schlieren pictures were taken from 50 ns after the first pulse, using the schlieren setup described in Section 3.4.2.

Schlieren images of plasma kernel with single pulse

We first studied the plasma kernel development with a single-pulse nanosecond spark. Figure 5.5 shows single-shot schlieren images of the plasma kernel generated by a single-pulse spark in pure-air. As can be seen, the heated channel is formed at about 50 ns and doubles in size at 0.5 µs. Between 0.5 µs and 8 µs, a shock wave appears at the boundary of the heated channel and propagates outwardly. The plasma kernel in the center continues growing by diffusion over a longer period of time (8 µs-500 µs), and it finally dissipates in the surrounding air. At 500 µs, we see that the contrast of the plasma kernel is low, indicating that the density of the plasma nearly returns to that of ambient air.

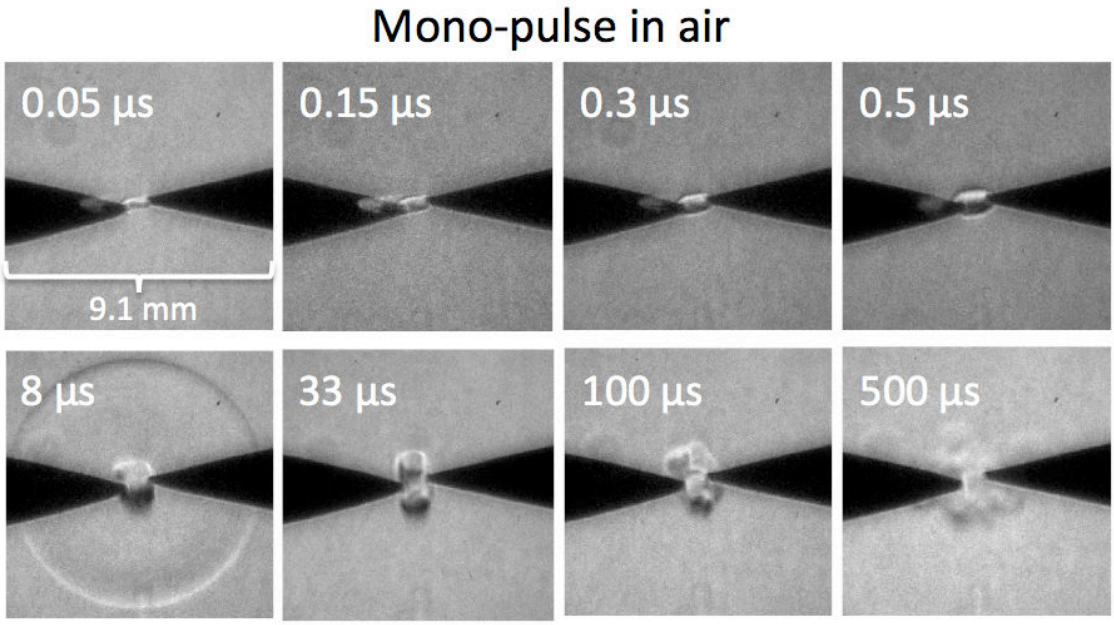

Figure 5.5 Single-shot schlieren images of the plasma kernel generated by a single-pulse nanosecond spark. The exposure time is 20 ns. The times indicated on the images are relative to the discharge initiation. FID-4, d=0.6 mm, 50-Ω in series, energy of pulse = 3 mJ, air temperature = 300 K, pressure = 1 bar.

Moreover, we can see from Figure 5.5 that in order to create synergetic effects with multiple pulses, one should create the second pulse at a time when the plasma kernel has not yet cooled down (i.e. time between two pulses < 100 µs, or pulse repetition frequency (PRF) >10 kHz). This provides a qualitative explanation of why NRP discharges with high PRF favor the ignition process in contrast with NRP discharges with low PRF. The effect of the PRF on the global ignition parameters (e.g.

ignition delay time, combustion time and ignition probability) will be presented in detail in Section 5.3.

Schlieren images of plasma kernel with multiple pulses

We generated a train of 10 pulses with a PRF=30 kHz to investigate the accumulative effect of successive NRP discharges. Figure 5.6 shows single-shot schlieren images of the plasma kernel generated by a train of 10 nanosecond pulses in pure-air. The first 6 images are taken at 8 μs after the 1st, 2nd, 3rd, 4th, 5th and 10th pulse, respectively. Then, after the NRP discharges stop (at time t = 333 μs), we show 3 additional images taken at longer elapsed times to show the subsequent evolution of the plasma kernel. It is interesting to see that each pulse generates one shock wave, however, because the FID pulser fires a secondary pulse at about 250 ns after the main pulse, the secondary pulse also generates a weaker shock wave (except for the secondary pulse of the 1st pulse, which did not make a breakdown). Those weak shock waves generated by secondary pulses follow the shock waves generated by the main pulses with a spatial distance of about 1 mm.

As can be seen from the images, the velocity of the shock waves increases slightly from one pulse to the next, with about a 10% increase from the 1^{st} to the 10^{th} pulse, because they propagate in the heated air created by previous pulses.

In contrast, compared with the plasma kernel development in the single-pulse case shown in Figure 5.5, we see that with multiple pulses the plasma kernel grows to a much greater volume, and dissipates into the surrounding air after a much longer time. For instance, during times from 8 μs to 338 μs, in the single-pulse case the plasma kernel radial extent doubles and the plasma volume increases by about 8 times, governed only by the diffusion. In contrast, in the multiple-pulse case, the plasma kernel radial extent increases 4 times and the plasma volume increases about 64 times, which is 8 times greater than for the single-pulse case. This is due to the energy deposition by subsequent pulses. Therefore, as mentioned earlier, the diffusion is a very weak phenomenon contributing to the kernel development. The driver of the kernel development is the energy deposited by the NRP sparks.

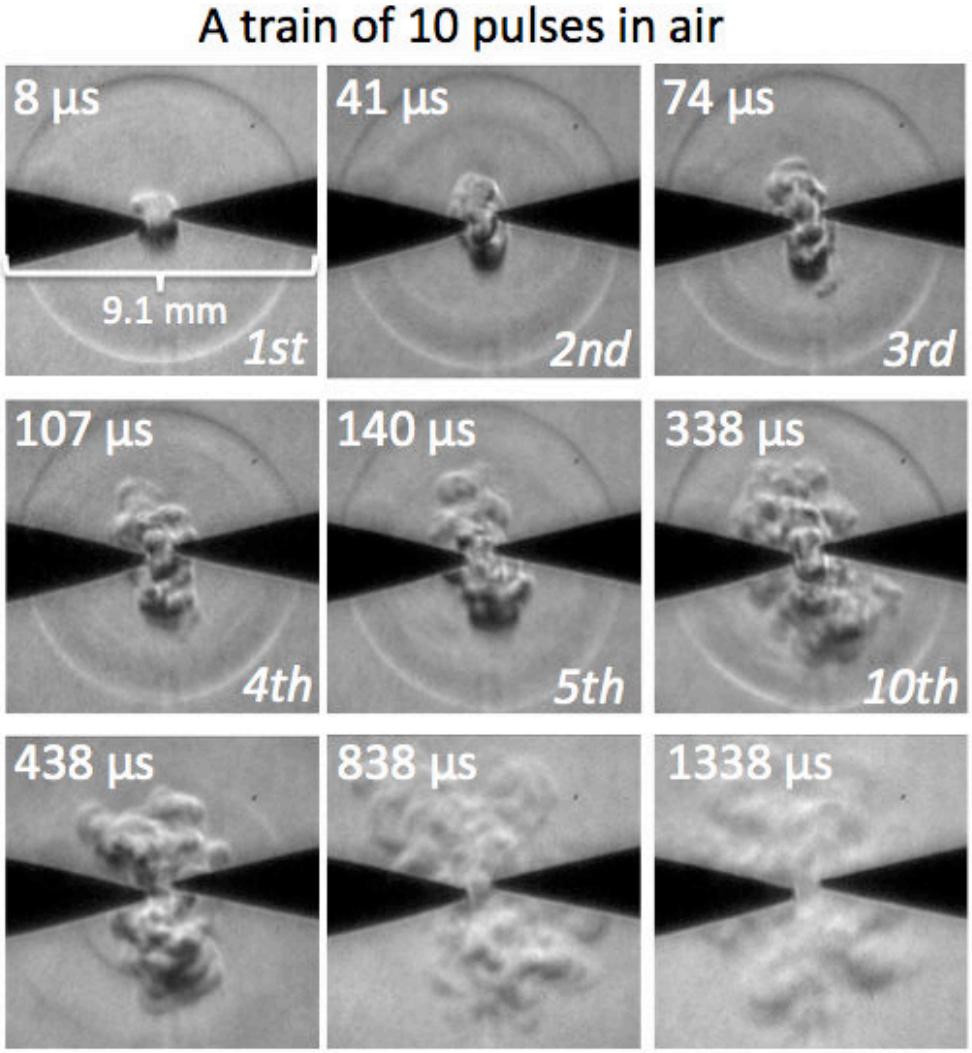

Figure 5.6 Single-shot schlieren images of plasma kernel generated by a train of 10 nanosecond spark pulses applied at 30 kHz. The exposure time is 20 ns. Numbers in the top left corner represent the elapsed time after the 1st pulse initiation. Numbers in the bottom right corner represent the counts of pulses fired. FID-4, d=0.6 mm, 50-Ω in series, PRF=30 kHz, energy per pulse = 3 mJ for the 1st pulse and 1.5 mJ for the subsequent pulses, air temperature = 300 K, pressure = 1 bar.

Plasma kernel in air vs. ignition kernel in lean mixture

Figure 5.7 shows single-shot schlieren images of the plasma kernel generated by a train of 10 pulses for pure air and the ignition kennel for the lean (ϕ=0.7) propane/air mixture. Images are shown for both an ignited mixture (successful ignition) and a non-ignited mixture (misfire). The quality of the images is better for pure air than for the propane/air mixture because in the case of pure air we did not use the sapphire windows. Inhomegeneities in the surface of these windows are responsible for the grainy appearance of the images observed with propane/air. At early times ($t < 0.8$ ms), we see that the kernel radii are almost identical for pure air and for the lean propane/air

mixture, but that the local structures are different. At 140 µs for instance, the boundary of the kernel is smoother in the mixture than in air. This effect could be due to partial ignition because the reactions of oxidation of propane occur at a very early time. Yet, the amount of heat released by the chemical reactions is too small to make a difference in terms of kernel radial extent. Therefore, the ignition kernel development in the lean propane/air mixture is similar to plasma kernel development in air.

Additionally, we observe that in the non-ignited case the ignition kernel radial extent is almost identical to that in the ignited case in the first 1 ms. After that time, the ignition kernel dissipates into the surrounding mixture, whereas in the ignited case the kernel grows into a self-sustained propagating flame. In this final stage, chemical energy and transport processes are the drivers of the flame.

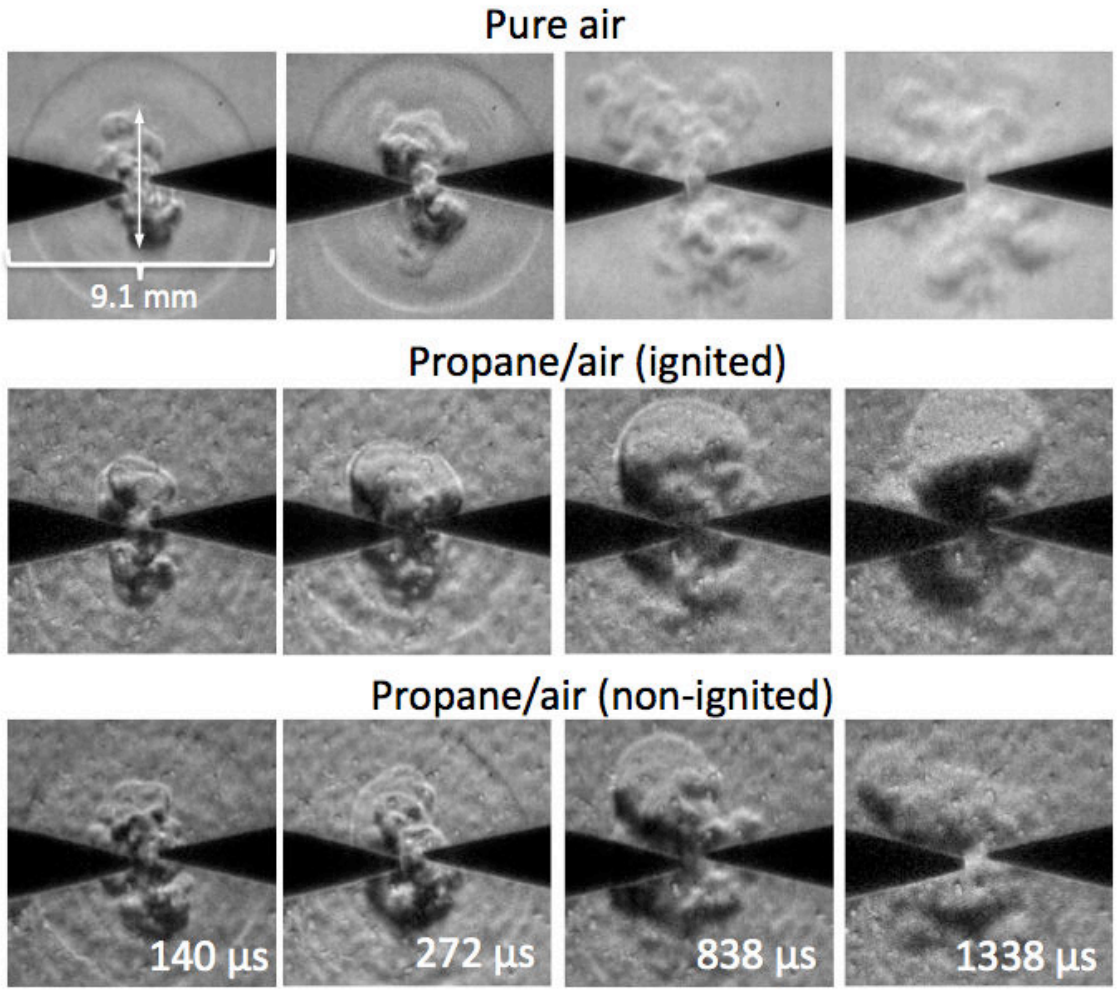

Figure 5.7 Single-shot schlieren images of plasma/ignition kernel generated by a train of 10 nanosecond spark pulses at 30 kHz in air and in the propane/air mixture (ignited and non-ignited cases). The exposure time is 20 ns. Numbers in the bottom represent the elapsed time after the 1st pulse initiation. FID-4, d=0.6 mm, 50-Ω in series, PRF=30 kHz, energy per pulse = 3 mJ for the 1st pulse and 1.5 mJ for the subsequent pulses, temperature = 300 K, pressure = 1 bar. Note that the image quality is degraded for propane/air due to impurities of the sapphire window.

Kernel growth and analytical treatment

Since the kernel is not spherical, it is difficult to determine the kernel radius. Thus we use the kernel radial extent to characterize the kernel development. The plasma radial extent is defined as the radial extent of the heated zone in a plane placed in the center of the spark and perpendicular to the electrodes, as is illustrated in Figure 5.7. Figure 5.8 shows the measured plasma radial extent as a function of time for ignition in the propane/air mixture with different number of pulses (NoP). A train of 15 pulses (duration 466 μs, E_{total}=24 mJ) or 10 pulses (duration 300 μs, E_{total}=16.5 mJ) successfully ignited the mixture. However, a train of 8 pulses (duration 233 μs, E_{total}=13.5 mJ) is near the ignition limit. In the latter case, the ignition kernel growth either leads to combustion and thus to a faster growth or degenerates and extinguishes. The limit between ignited and non-ignited cases occurs for a kernel radial extent of about 2.8 mm at about 800 μs. This value is close to the quenching distance of 3 mm reported by Lewis and von Elbe [87], and to the critical radius of 3.5 mm measured by Ko et al [36].

As can be seen from Figure 5.8, the ignition kernel grows rapidly with the energy deposited by the pulses. For the different cases, the kernel growths are almost identical in the first instants until the 8th pulse at 233 μs. At that time, for the 8-pulse case, the energy deposition is finished and the kernel growth slows down. For the 10-pulse and 15-pulse cases, the ignition kernel growth continues with the energy deposited by the subsequent pulses. The flame is then formed at about 1 ms, and it has a greater radial extent. Thus the flame radial extent increases with the increase of number of pulses deposited.

From the slopes of the curves, it can be inferred that after the ignition kernel grows into an outwardly propagating flame (at $t > 1$ ms), the flame propagates at nearly identical velocities of about 1 m/s for all the ignited cases.

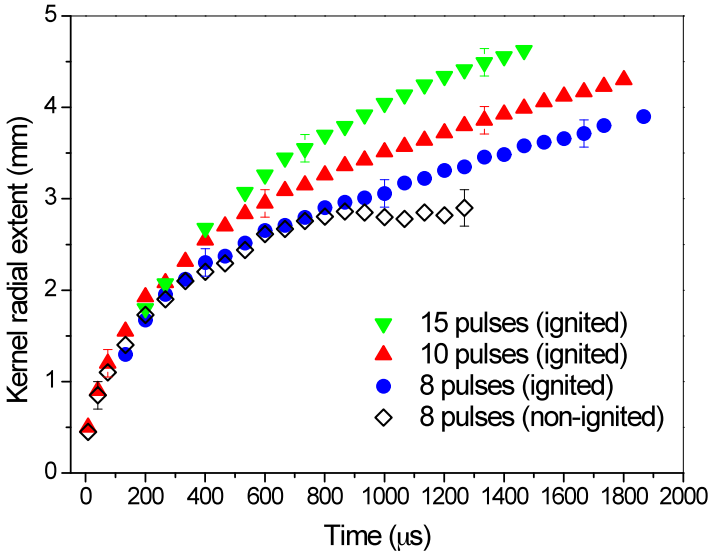

Figure 5.8 Ignition kernel radial extent vs. time for different number of pulses in the propane/air mixture (ignited and non-ignited cases). FID-4, d=0.6 mm, 50-Ω in series, PRF=30 kHz, energy per pulse = 3 mJ for the 1st pulse and 1.5 mJ for the subsequent pulses, temperature = 300 K, pressure = 1 bar.

Figure 5.9 shows the ignition kernel development in propane/air mixtures at pressures of 1 and 2 bar. The mixtures are ignited with 10 pulses at both pressures. It can be seen clearly that at 2-bar pressure, both the kernel radial extent and the flame propagating velocity are smaller than that at 1-bar pressure (the flame velocity decreases from about 1 m/s to about 0.7 m/s).

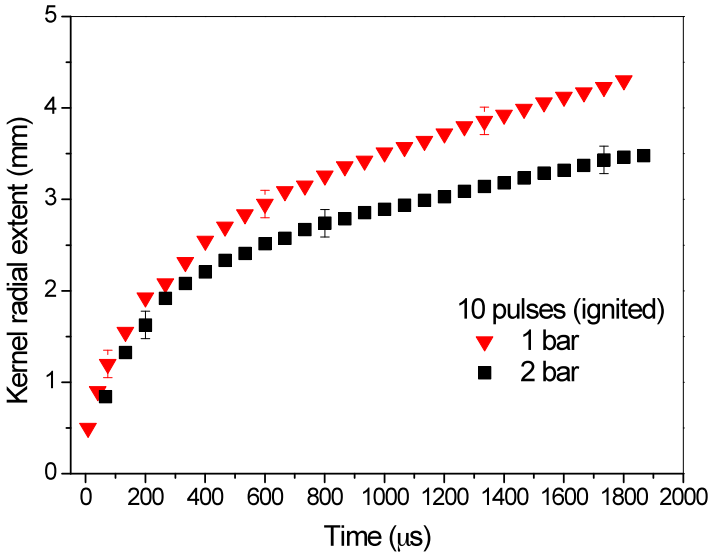

Figure 5.9 Ignition kernel radial extent vs. time at 1 and 2 bar. Propane/air mixtures ignited with a train of 10 pulses. FID-4, d=0.6 mm, 50-Ω in series, PRF=30 kHz, energy per pulse = 3 mJ for the 1st pulse and 1.5 mJ for the subsequent pulses, temperature = 300 K.

A simple thermodynamic model can be used to describe the ignition kernel growth [80]. The model depends on the following assumptions:

1) The amount of heat released by chemical reactions is negligible.

2) The calculations start after the hydrodynamic expansion following the breakdown (i.e. at 1 μs). The gas is assumed to be under hydrodynamic equilibrium.

3) Since the temperature rise is less than 2500 K [3], a value well below the range for conventional ignition (6000-7000 K), the equation of state is assumed to be unchanged. The radiation from the plasma to the surroundings is negligible.

4) The kernel is approximately spherical.

5) Since the thermal boundary layer is thin, it is assumed that the kernel is a mass-constant system.

6) The diffusion processes to the surroundings and the conduction losses to the electrodes are negligible.

7) The cathode sheath and the associated heat loss are negligible. This is a valid assumption for spark discharges [68].

The energy conservation law leads to

$$\frac{dQ}{dt} = \frac{C_p}{R} p \frac{dV}{dt} \tag{5.8}$$

where Q is the total energy deposited by the NRP discharges at time 't,' C_p is the heat capacity, R is the perfect gas constant, p is the pressure and V is the volume of the ignition kernel：

$$V = \frac{4}{3}\pi r^3 \tag{5.9}$$

Solving (5.8) and (5.9) we obtain:

$$r = \left(\frac{3}{4\pi} \frac{R}{pC_p} (Q - Q_1) + r_1^3 \right)^{\frac{1}{3}} \tag{5.10}$$

where Q_1 is the energy input of the first pulse = 3 mJ, r_1 is the radius at t = 1 μs after the first pulse, $r_1 = \sigma r_0$ with $\sigma \sim 2.0$. Note that we distinguish between the initial spark radius r_0 discussed in Section 5.2.1 and the radius r_1 used as the start of calculations for the model.

Figure 5.10 shows the comparison between the model and the experiment for the propane/air mixture. Good agreement is obtained for 1-bar pressure during the energy deposition (1-300 μs). After that time, the radius remains constant in the model while in the experiments the radial extent continues to increase due to diffusion. For 2-bar pressure, good agreement is maintained only in the first 200 μs and large differences can be observed at later times between experimental and theoretical kernel radii. This is probably because the heat release of chemical reactions is greater for high-pressure mixtures. Taking into account the amount of heat release would improve the ignition kernel growth models, but nevertheless the trends are already well captured by the

model.

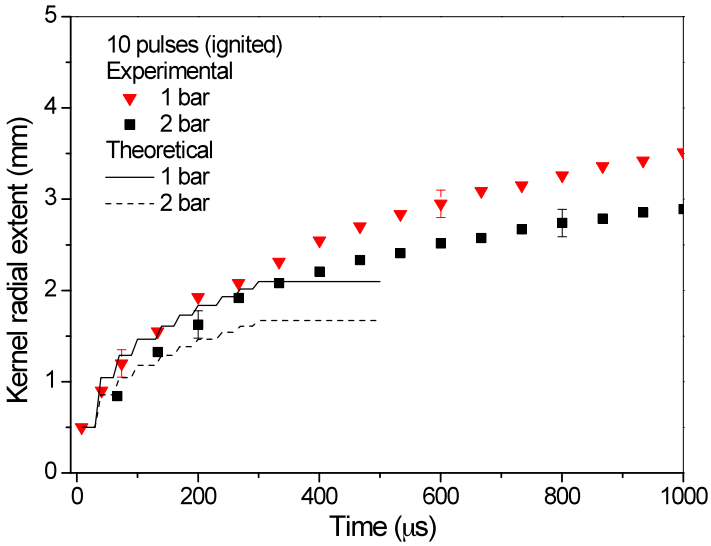

Figure 5.10 Predicted ignition kernel radii and comparison with experimental kernel radial extent at different pressures.

5.3 Lean mixture ignition by NRP discharges

In a constant volume chamber, it is difficult to conduct experiments representative to real engine conditions. For instance, in an automobile spark-ignited engine working with gasoline/air or an alternative fuel/air mixture, the operative conditions with typical spark ignition energy ~ 60 mJ are: pressure above 10 bar, temperature above 500 K. In contrast, in our constant volume chamber, the conditions for a propane/air mixture with NRP discharges of equivalent energy are: pressure under 10 bar, temperature of 300 K. Clearly, we cannot reproduce real engine conditions here. Nevertheless, laboratory-scale experiments are useful to understand the general effects of NRP discharge parameters on lean mixture ignition

In this section, the effects of PRF, which determines the average power, and of the number of pulses (NoP), which determines the total energy, on lean mixture ignition are examined under typical laboratory operating conditions. The ignition parameters measured are: minimum ignition energy, ignition probability, pressure increase during combustion, pressure delay time and rise time, equivalent flame radius and flame propagation speed. A comparison between FID-2 and a conventional igniter (Audi coil, duration 3.5 ms, E=57 mJ) is made for various parameters related to the pressure and the equivalent flame radius.

5.3.1 Minimum ignition energy (MIE) and ignition probability

Definitions and experimental procedure to determine the MIE

The minimum ignition energy (MIE) is an important parameter for ignition. It is

defined as the smallest amount of energy that an electric spark discharge must have to successfully ignite a given gas mixture at certain conditions. For the last century, many experiments have been conducted to determine the MIE for hydrocarbon fuels [36, 87, 88]. However, near the ignition limit, there is not single threshold energy value [89]. Ignition or no-ignition is a statistical binary response. Thus the MIE is statistically determined at a certain ignition probability. Moorhous et al. [88] used a probability of ignition of 1% as the criterion with which to define MIE, whereas Ko et al. [36] suggested 50%. Since different authors used different criteria, it is difficult to compare the obtained values of MIE.

The ignition probability depends not only on the composition of the mixture, but also on the electrode geometry, the spark generation method, the type of discharge, the pressure, temperature, flow characteristics, spark gap length, and discharge duration. Therefore, the ignition probabilities measured by previous authors differ from one to another

The ignition probability (denoted P) is defined as the ratio of the number of ignition events (denoted m) to the total number of trials (denoted n):

$$P = m / n \tag{5.11}$$

A practical question is: how many trials are required to obtain a meaningful ignition probability? Figure 5.11 shows the ignition probability as a function of the number of trials. As can be seen from the figure, a sample size of at least 20 trials must be considered for the measured ignition probability to reach steady state. Therefore, in all our experiments, 40 trials were conducted for each energy to obtain a sufficiently accurate determination of the ignition probability.

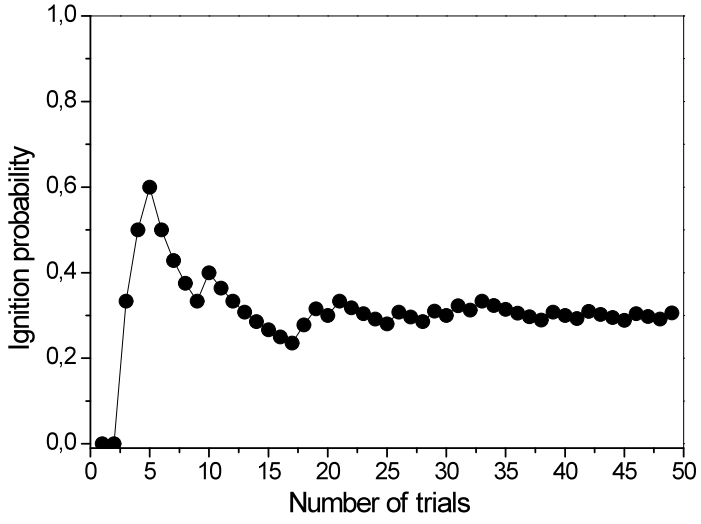

Figure 5.11 Ignition probability versus number of trials. Propane/air mixtures ignited with a train of 15 pulses (20 mJ in total) generated by FID-2, energy per pulse = 6.2 mJ for the 1st pulse and 1.2 mJ for the subsequent pulses. d=0.6 mm, 50-Ω in series, PRF=30 kHz, T = 300 K, P = 2 bar.

Logistic regression is a convenient approach for modeling binary response and it can be used to model the ignition probability [89]. Based on the logistic regression model, the ignition probability P as a function of energy E can be fitted by the following equation:

$$P(E) = \frac{1}{1 + e^{-(\beta_0 + \beta_1 E)}} \tag{5.12}$$

where β_0 and β_1 are fitting parameters.

In this thesis, the MIE is defined using an ignition probability of 50%, as proposed by Ko et al[36]. With known β_0 and β_1, the MIE can be calculated:

$$MIE = (\ln\frac{50\%}{1-50\%} - \beta_0)/\beta_1 = -\frac{\beta_0}{\beta_1} \tag{5.13}$$

Effects of PRF and number of pulses (NoP) on the MIE

The effects of PRF and NoP on the ignition probability were studied using the FID-2 generator and are presented in Figure 5.12. As explained above, each experimental data point (symbol) represents a minimum of 40 trials to accurately determine the ignition probability for PRF from 2 to 30 kHz and for NoP up to 800 pulses (equivalent to about 965 mJ). It can be seen that for all the PRFs investigated, the ignition probability increases with the total energy deposited. The ignition probability also increases with the PRF. In other words, ignition is easier at high PRFs. For instance, for PRF=30 kHz, 40 mJ is enough to get 100% ignition, however, for PRF=2 kHz, almost 1000 mJ is required to reach 100% ignition.

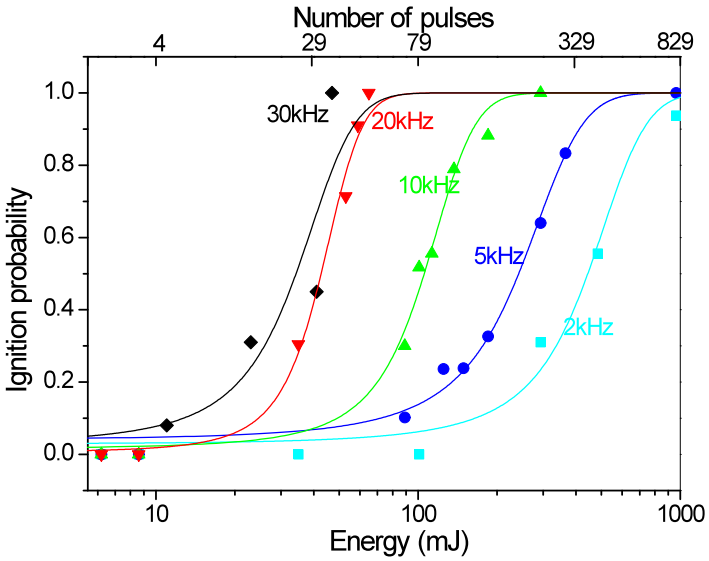

Figure 5.12 Ignition probability as a function of NoP (or energy) and PRF. FID-2, energy per pulse = 6.2 mJ for the 1st pulse and 1.2 mJ for the subsequent pulses. d=0.6 mm, 50-Ω in series, T = 300 K, P = 2 bar.

In Figure 5.12, logistic regressions (curve) are shown for each PRF. The MIEs are determined as the energy required to obtain a 50% ignition probability on the fitted curves, and are plotted in Figure 5.13 as a function of PRF. It is found that the MIE decreases with increasing PRF. Above 20 kHz, increasing the PRF has little benefits on the MIE, which seems to reach a steady value of about 35 mJ. The MIE cannot be reduced further because it depends on other parameters such as the nature of the combustible mixture, the losses to the electrodes...

Since the PRF is directly related to the average power of the NRP discharges, we conclude that the average power is a key parameter for the ignition of lean mixtures. Given a certain amount of total energy, the way in which the energy is deposited is very important. Depositing the energy in a short time (i.e. high power) can result in small MIEs, making a lean mixture easier to ignite, thus is beneficial to lean mixture ignition. However, this result is probably flow-dependant and further investigation will be necessary to conclude for real condition engines.

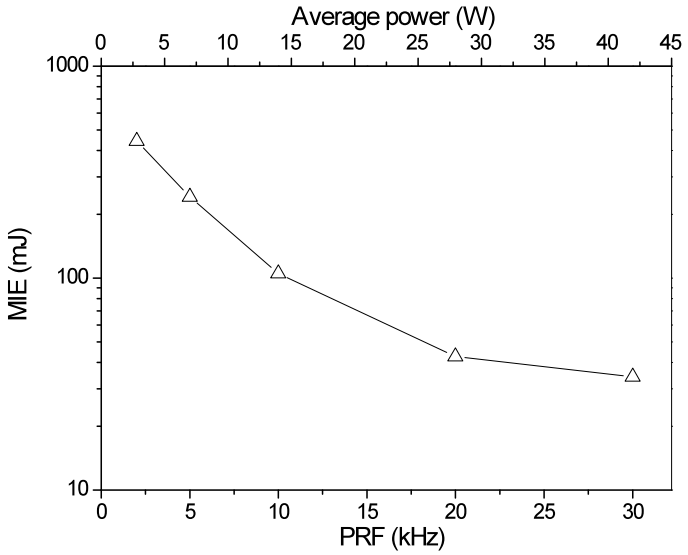

Figure 5.13 Minimum ignition energy as a function of PRF (or averaged power).

5.3.2 Pressure delay time and pressure rise time

Definitions

We recorded variations of pressure to follow the evolution of the combustion process inside the chamber. The pressure rise occurs at the end of the combustion process when the flame front compresses the unburned gas near the wall.

An example of the variation of pressure during combustion is presented in Figure 5.14 for an initial pressure of 1 bar. To analyze the pressure change, we use two usual parameters: the delay time, defined as the time between the last pulse and a 10 % pressure increase, and the pressure rise time, defined as the time required for the pressure to increase from 10% to 90% of its maximum value. For each configuration, 5

independent trials are recorded to determine accurate values of the pressure delay time and rise time. As can be seen in Figure 5.14, the reproducibility of the measurements is quite good and the experimental scattering is within ±5%.

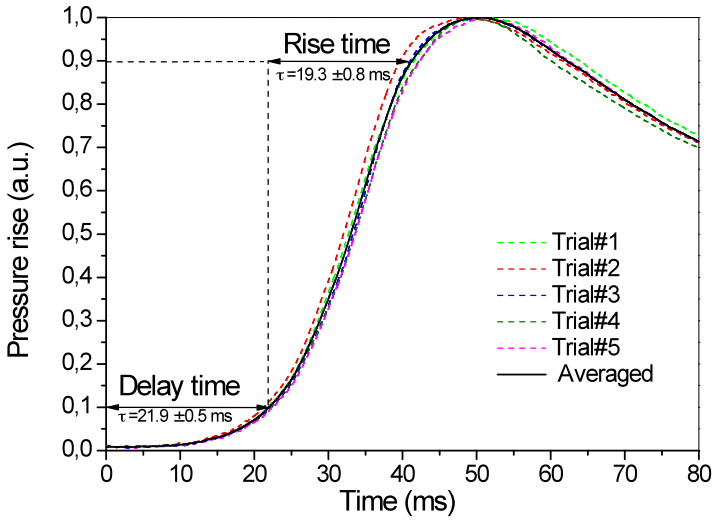

Figure 5.14 An example of pressure increase. Propane/air mixture ignited with a train of 15 pulses (20 mJ in total) generated by FID-2, energy per pulse = 6.2 mJ for the 1st pulse and 1.2 mJ for the subsequent pulses. d=0.6 mm, 50-Ω in series, PRF=30 kHz, T = 300 K, P = 3 bar.

Effects of PRF and NoP

The effect of PRF on the pressure delay time is presented in Figure 5.15. For all measurements, the total energy deposited is kept constant at 41 mJ. It is observed that for NRP spark ignition, the pressure delay time decreases with increasing PRF, from about 28 ms at 2 kHz to about 19 ms at 30 kHz. Increasing the PRF above 20 kHz does not further reduce the delay time, which seems to reach an asymptotic minimum value of about 19 ms.

We repeated the measurements for a conventional igniter (Audi coil producing a capacitive spark discharge with energy 57 mJ and duration 3.5 ms, thus power 16 W). The measured pressure delay time is plotted in Figure 5.15 against the average power for comparison with NRP spark ignition. Although the total energy deposited by the capacitive spark discharge (Audi coil) is a bit different from that of NRP discharges (41mJ compared to 57 mJ), the measured pressure delay time for the conventional igniter is very close to that for NRP spark ignition at the same power level, for instance, the one at 10 kHz and about 13 W. This confirms that for a given energy and for quiescent mixture, the pressure delay time depends primarily on the average power deposited by the ignition system.

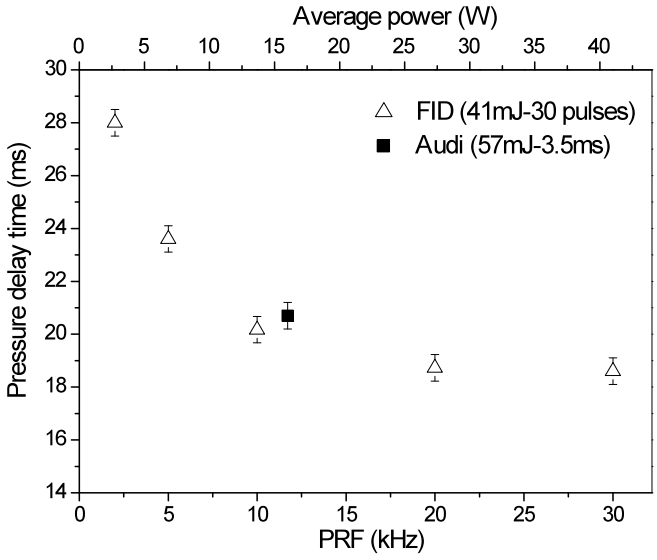

Figure 5.15 Pressure delay time for different PRFs (or averaged power) compared with an Audi igniter. NoP = 30 pulses (41 mJ in total) generated by FID-2 with 50-Ω in series, d=0.6 mm, T = 300 K, P = 2 bar.

Although the PRF has a strong effect on the pressure delay time, it seems to have no effect on the pressure rise time, as seen in Figure 5.16. The pressure rise time stays constant at about 17 ms for different PRFs of NRP discharges and also for the Audi igniter.

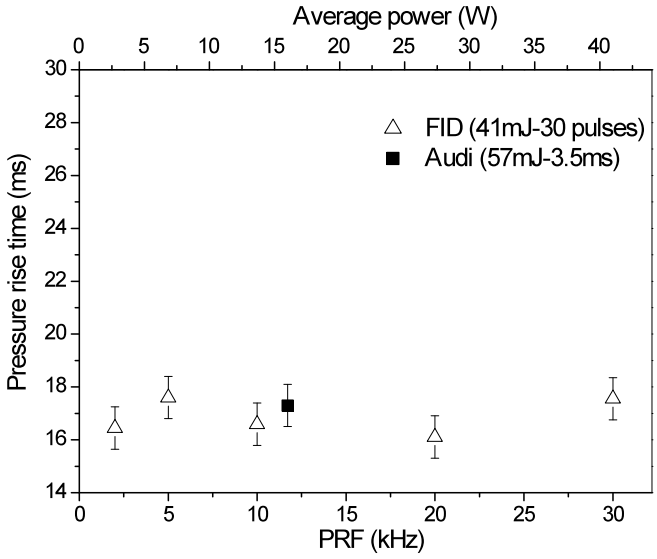

Figure 5.16 Pressure rise time for different PRFs (or averaged power) compared with an Audi igniter. NoP = 30 pulses (41 mJ in total) generated by FID-2 with 50-Ω in series, d=0.6 mm, T = 300 K, P = 2 bar.

The effect of NoP on the pressure delay time is presented in Figure 5.17. For all

measurements, the PRF is kept constant at 30 kHz. We chose this value of 30 kHz because it gave the best results in terms of MIE and pressure delay time. For NRP spark ignition, we observe that the pressure delay time decreases with increasing NoP, from about 21 ms with 3 pulses (or 8.6 mJ) to about 15 ms with 400 pulses (or 485 mJ). Above 100 pulses (or 125mJ), increasing the NoP provides little gain on the delay time, which seems to reach a constant value.

For the Audi igniter, the capacitive discharge energy is 57 mJ. The measured pressure delay time is plotted in Figure 5.17 against the total energy for comparison with NRP spark ignition. We note a significant difference in pressure delay time between the Audi and the NRP spark igniters for the same total energy. This can be due to the different average power for those two ignition systems. The average power of NRP discharges is 40 W, which is twice the power of the Audi igniter.

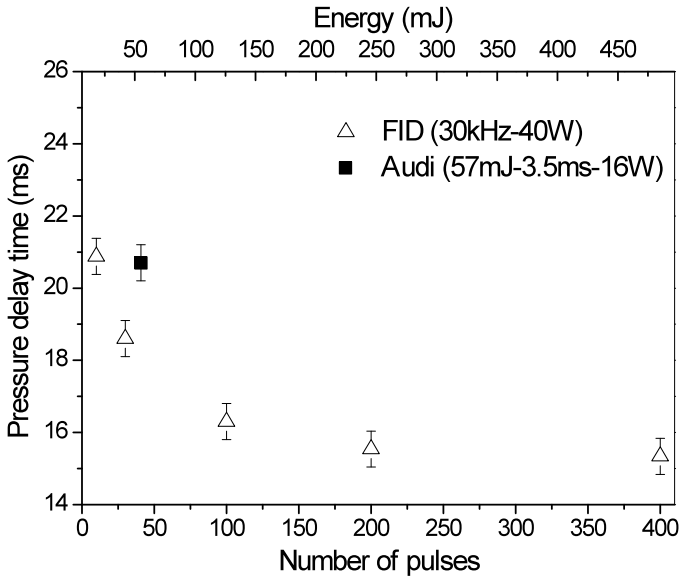

Figure 5.17 Pressure delay time for different NoPs (or total energy) compared with an Audi igniter. PRF = 30 kHz (averaged power = 40 W) generated by FID-2 with 50-Ω in series, d=0.6 mm, T = 300 K, P = 2 bar.

Like the PRF, the NoP has a strong effect on the pressure delay time, but it seems to have no effect on the pressure rise time, as can be seen in Figure 5.18. The pressure rise time is constant whatever the total energy deposited, and whichever ignition system used. This means that, when the flame is far from the ignition zone, there is no influence of the ignition process.

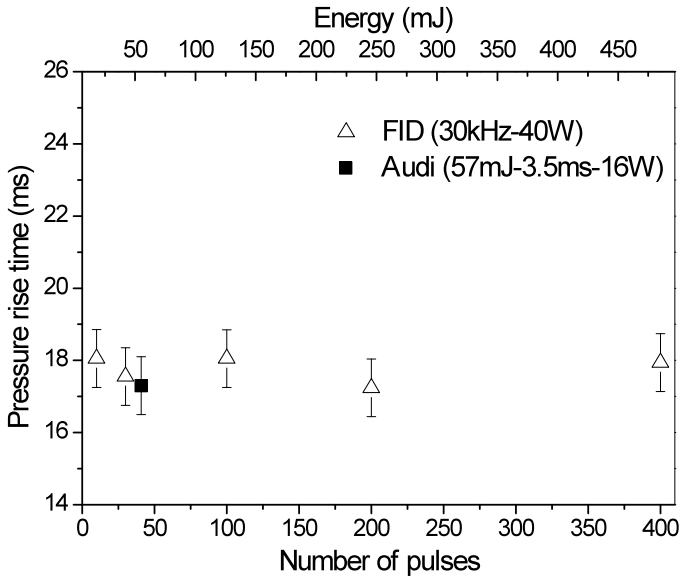

Figure 5.18 Pressure rise time for different NoPs (or total energy) compared with an Audi igniter. PRF = 30 kHz (averaged power = 40 W) generated by FID-2 with 50-Ω in series, d=0.6 mm, T = 300 K, P = 2 bar.

We have seen in this subsection that the PRF and NoP of NRP discharges are two important parameters that have large effects on the pressure delay time of lean mixture ignition, because they are directly related to the average power and total energy, respectively. Thus the reduction of the pressure delay time of ignition systems relies on the optimization of these two parameters. On the other hand, these parameters do not affect the pressure rise time. However, the pressure rise time is not directly related to flame speed, so we need to investigate more closely the effects of the types of discharge on the flame speed. This is done in the following section.

5.3.3 Flame radius, flame speed and laminar burning velocity

Definitions

The flame speed is an important parameter for combustion. It is the rate of expansion of the flame front in a combustible mixture. In an internal combustion engine, the flame speed influences the rate of pressure rise inside the cylinder, the quality of combustion and consequently it affects the engine performance.

In contrast to the flame speed that depends on different flow and flame parameters, the laminar burning velocity is a fundamental, intrinsic property of a combustible mixture. It is defined as the speed at which an unstretched, planar laminar flame propagates through a quiescent mixture of unburned reactants. It depends only on the chemical properties, the pressure and the temperature of the mixture.

In this thesis, the flame speed is determined as follows: the trajectories of the

outwardly propagating spherical flames initiated by NRP discharges are recorded by using the schlieren photography technique detailed in Section 3.4.4. The evolution of the flame radius R_f is obtained through frame-by-frame processing. The flame speed is equal to the propagation velocity of the flame front, and is evaluated as [81, 90, 91]:

$$S_f = \frac{dR_f}{dt} \tag{5.14}$$

where S_f and R_f are the flame speed and the flame radius, respectively.

The obtained flame speed reflects the stretch effects associated with the propagation of a flame surface. These effects consist of both the flame-front curvature and the local dynamic strain.

It is also interesting to measure the laminar burning velocity for comparison, although it is not supposed to change with different ignition systems.

For a spherical flame in the constant volume chamber used in our experiment, we can determine the laminar flame speed from the measured flame speed for moderate stretch rates. This is because for moderate stretch rates, the flame speed can be considered to vary linearly with the stretch rate, K [92, 93]:

$$S_f = S_b^0 - L_b K \tag{5.15}$$

where S_b^0 and L_b are the unstretched flame speed and the Markstein length, respectively, of the burned mixture. The Markstein length can be either positive or negative, and it indicates how the flame is influenced by the stretch. If L_b is positive, the flame speed decreases with stretch, thus the flame is stable. If L_b is negative, the flame speed increases with stretch, thus the flame becomes unstable. Moreover, the magnitude of L_b indicates to what extent the flame is influenced by the stretch. The stretch rate, K, is defined as the rate of relative change of the flame area. For expanding spherical laminar flames, it can be expressed as:

$$K = \frac{1}{A}\frac{dA}{dt} = \frac{2}{R_f}\frac{dR_f}{dt} \tag{5.16}$$

where A is the flame area.

Hence, the unstretched flame speed, S_b^0, and the Markstein length, L_b, can be obtained from a linear extrapolation of the plot of S_f versus K using (5.15).

Finally, the laminar burning velocity S_u^0 (relative to the unburned gas) is related to the unstretched flame speed, S_b^0 (relative to the burned gas) through the mass conservation law:

$$S_u^0 = \frac{\rho_b}{\rho_u} S_b^0 \tag{5.17}$$

The above equation is valid under the assumption that the laminar flame thickness is far less than the flame radii [91], which is thus justified in the present study.

Actually, utilizing an outwardly propagating spherical flame in a confined bomb is the most favorable way to determine the laminar flame speed experimentally, especially

at high pressures [90].

Schlieren images of the flame

We recorded successive schlieren images of the flame ignited by the Audi igniter and the FID-2 generator for from 2 to 10 bar. As discussed previously, it is interesting to compare the two ignition systems for the same power and the same total energy. To do so, we increased the resistance in series with the FID-2 generator to reduce the energy per pulse. Using a 100-ohm resistance, the energy per pulse deposited in the plasma by FID-2 is reduced to 4.6 mJ for the first pulse and 0.62 mJ for the subsequent pulses. Therefore, for 82 NRP pulses with PRF=30 kHz, the total energy is about 55 mJ, equivalent to the 57 mJ deposited by the Audi coil; the power is about 22 W, also close to the 16 W of the Audi coil.

Figure 5.19 shows high-speed schlieren images of flames ignited by NRP discharges and by the Audi coil at pressure 2-10 bar. A flame is formed in the discharge channel and propagates outward. The flame is smooth only for ignition with the Audi coil at 1 atm. At all pressures, the flame ignited by NRP discharges has more cellular instabilities on the flame surface than that ignited by the Audi coil. This phenomenon affects the flame radius at elevated pressure. For instance, at 2-bar pressure, the flame ignited by the Audi coil is smooth and it can be considered as a wrinkle-free spherical flame, whereas the flame ignited by NRP discharges exhibits some structures. Nevertheless, the radii of the two flames are very close. At 5 and 10 bar, although the flames ignited by the Audi coil are not smooth, the flame ignited by NRP discharges are much more wrinkled and thus propagate at a greater speed. Thus at 15 ms for instance, the equivalent flame radius is about 2 mm greater than with the Audi coil.

The flame wrinkling induced by the NRP discharges seems to accelerate the flame. Interestingly, the wrinkling appears at a very early time. At 5 ms for instance, the flame ignited by NRP discharges seems to have more structures, and this turbulence appears to be induced by the multiple nanosecond discharges. At later times, these structures develop into cellular wrinkling at the flame surface. Therefore, the flame propagation strongly depends on the ignition kernel. It is shown that NRP discharges generate more aerodynamics in the ignition kernel, leading to a faster flame propagation speed.

We will quantify these effects in the following section.

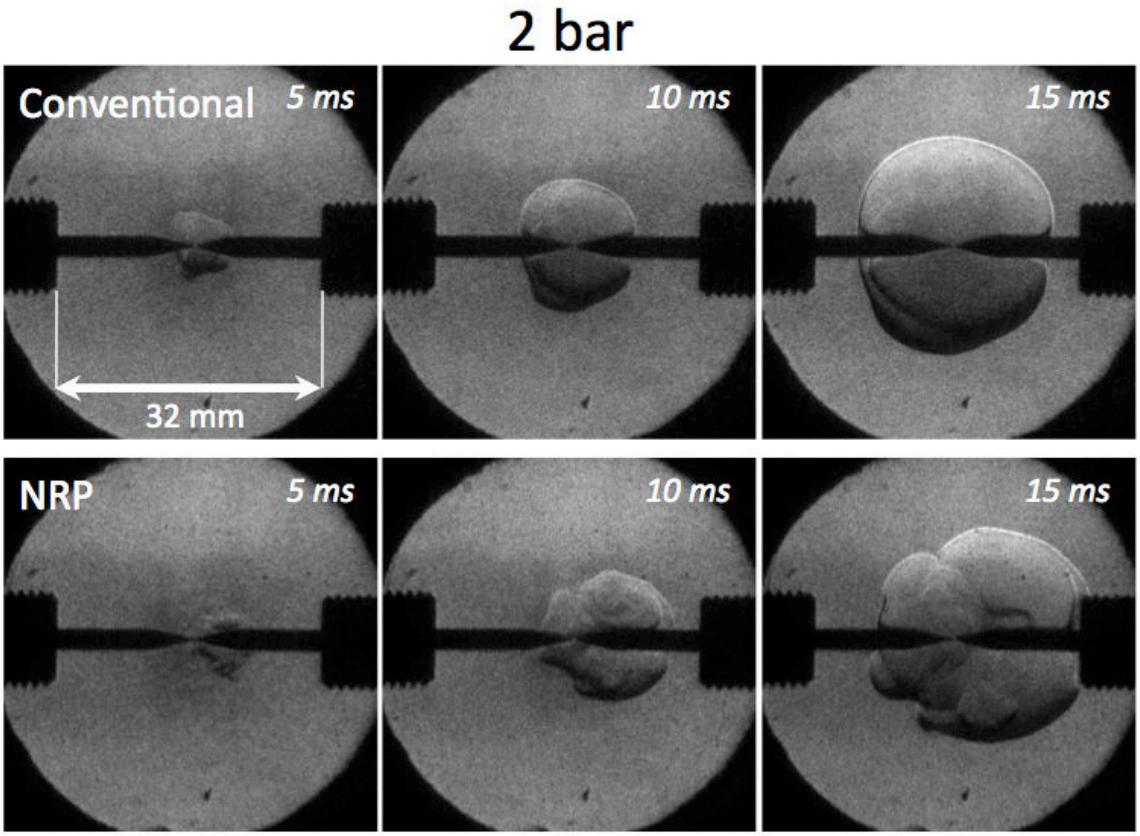
2 bar
Conventional
5 ms
10 ms
15 ms
32 mm
NRP
5 ms
10 ms
15 ms

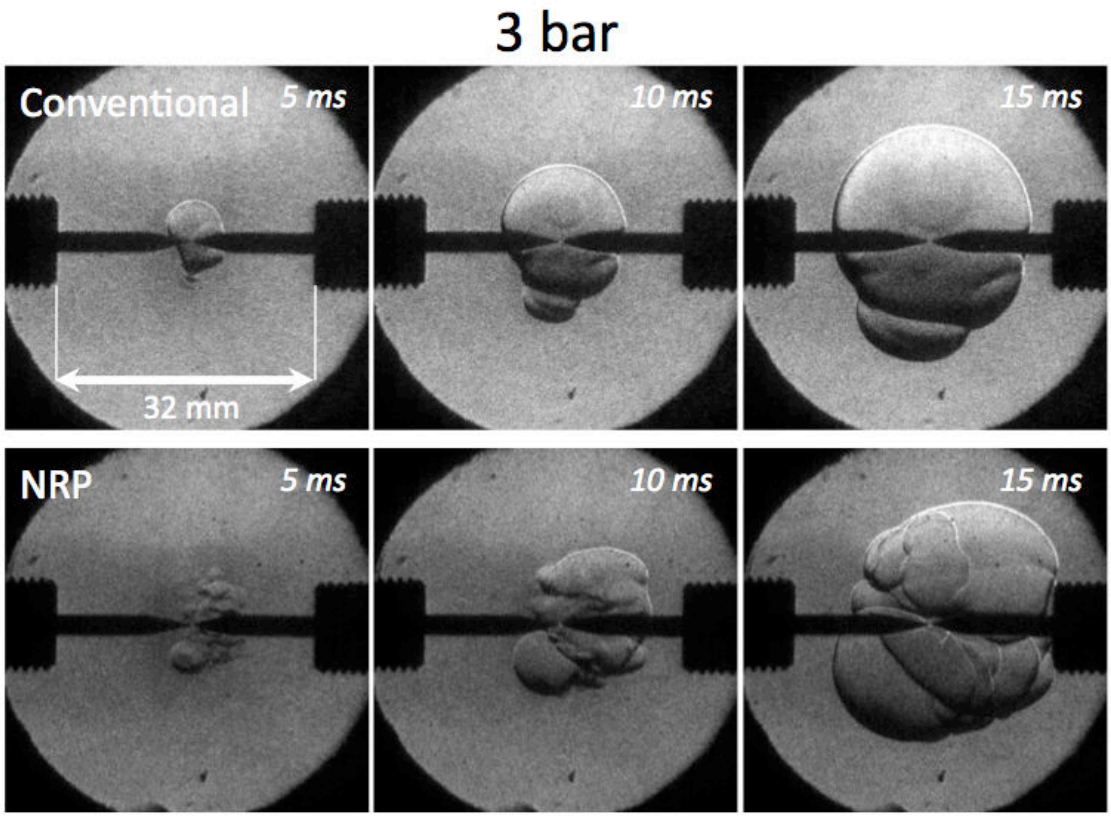
3 bar
Conventional
5 ms
10 ms
15 ms
32 mm
NRP
5 ms
10 ms
15 ms

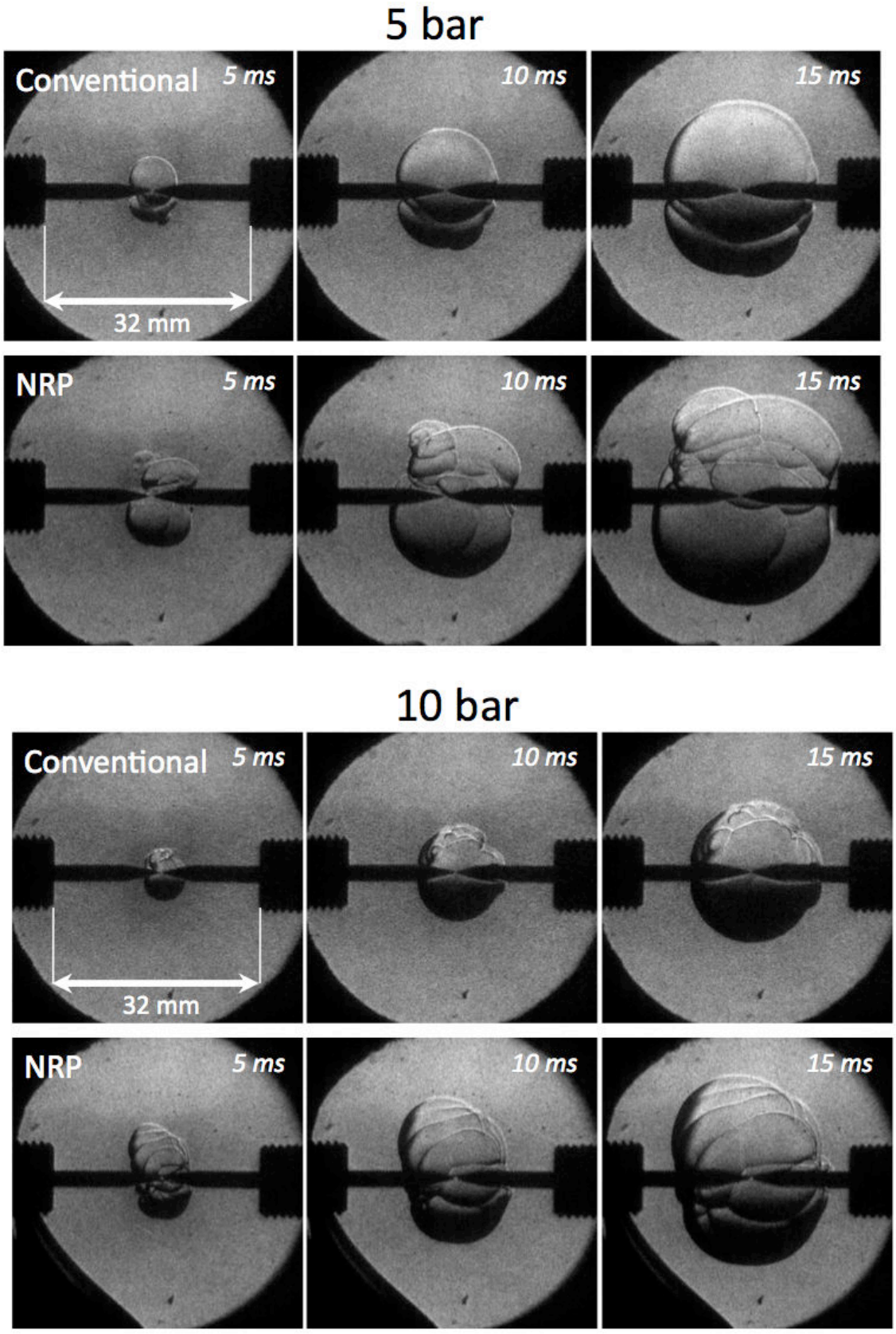

Figure 5.19 Schlieren images of C_3H_8/air (ϕ=0.7) flames at 2, 3, 5 and 10 bar ignited by 82 NRP discharges at 30 kHz (55 mJ - 22 W - 2.7 ms) and by a conventional Audi coil (57 mJ - 16W - 3.5 ms). Exposition time is 1 µs. Gap distance d=0.6 mm. T=300 K.

Measured equivalent flame radius and analysis

To quantify the effects discussed in the previous section of the pressure on the flame speed, we performed a quantitative analysis of the temporal evolution of the radii of the flames shown in Figure 5.19. A Matlab program was developed to extract the equivalent flame radii in the schlieren images. Sample measurements by the program are shown in Figure 5.20. As can be seen, the program automatically traces the flame front location and fit it with an ellipse. An equivalent radius is then computed as the radius of a sphere with the same area as the ellipse. This method has been adopted and discussed by previous authors [37, 94].

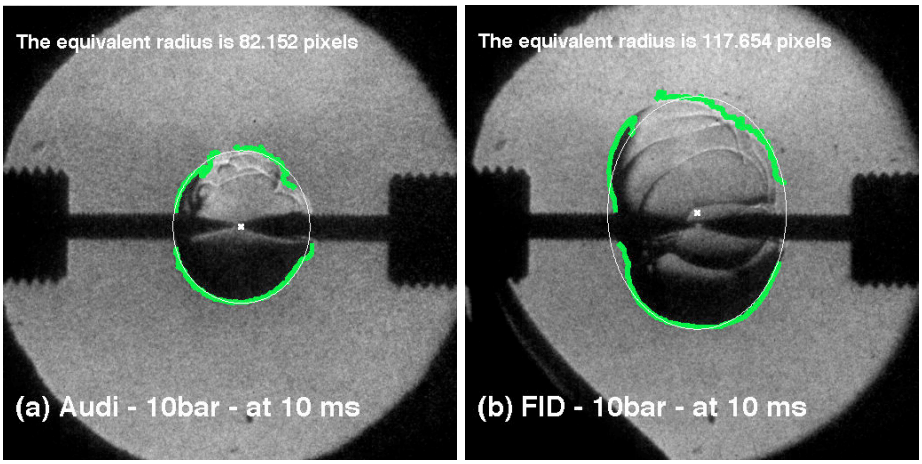

Figure 5.20 Sample Matlab treatment to extract equivalent flame radius.

The effect of pressure on the flame propagation for the case of the Audi igniter is shown in Figure 5.21, where the measured equivalent flame radius is plotted as a function of time for initial pressures ranging from 2 to 10 bar. It is seen that the slope of the radius curve decreases with increasing pressure, indicating that the flame speed decreases with the pressure.

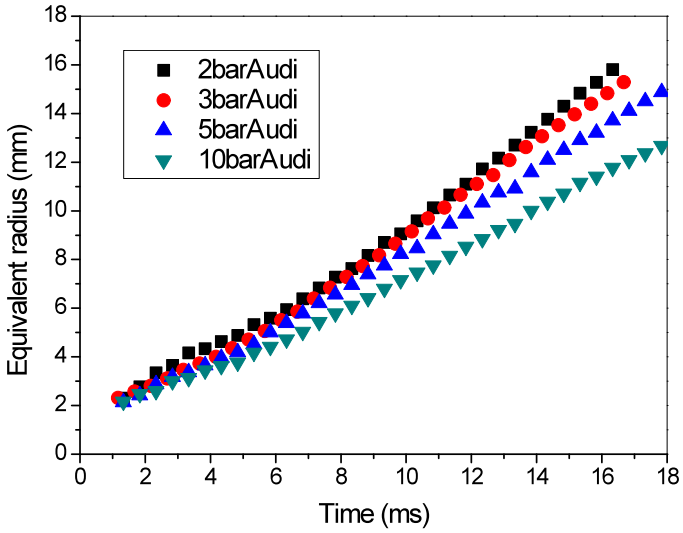

Figure 5.21 Effect of the initial pressure on the measured equivalent flame radius.

Figure 5.22 shows a comparison of the equivalent flame radii obtained with the

two ignition systems at pressures up to 10 bar. At 2 bar, the flame radii are almost identical. At 3 bar, the equivalent flame radius for NRP discharges becomes larger after t>10 ms. Here an additional ignition experiment with 10 pulses was performed. This experiment shows that with 10 times less total energy, the equivalent flame radius is the same as that for ignition with the Audi coil. Finally, at 5 and 10 bar, we see that the NRP spark igniter clearly increases the equivalent flame radius and the flame speed. As shown in Figure 5.23, the flame speed increases by up to 18% over the same pressure range. Thus these experiments evidence a beneficial effect of NRP spark discharges on the flame speed.

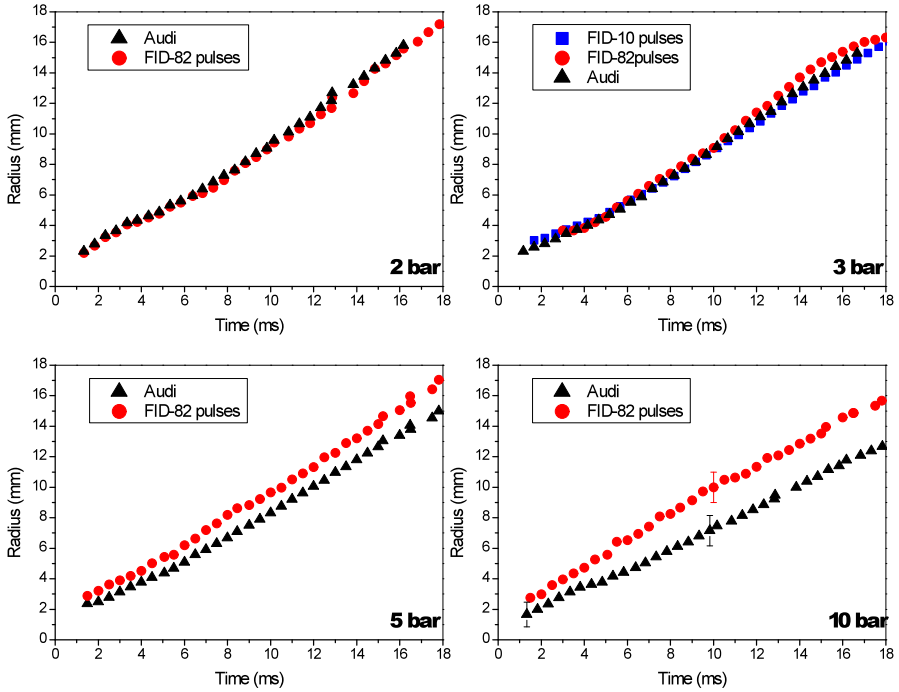

Figure 5.22 Comparison of the equivalent flame radius of lean flames ignited by 82 NRP discharges at 30 kHz (55 mJ - 22 W - 2.7 ms) and by a conventional Audi coil (57 mJ - 16W - 3.5 ms). Exposition time is 1 µs. Gap distance d=0.6 mm. T=300 K, P = 2-10 bar.

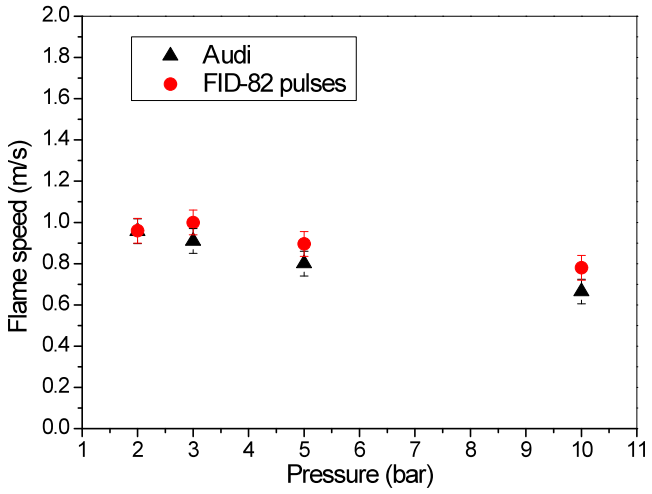

Figure 5.23 Comparison of the flame speed at 10 ms.

To validate the experimental procedure, we return to the question of the laminar flame speed. Because the laminar speed is an intrinsic property of the mixture independent of the ignition source, we can compare our results with the experimental data in the literature. Since the flame is wrinkle-free only for ignition with the Audi coil at 2-bar, we limited our analysis to that pressure condition. We obtained the laminar flame speed at 2 bar using the linear relation between the flame speed and the stretch rate expressed in (5.15). Although a few wrinkles are seen for ignition with NRP discharges, the equivalent flame radius is almost identical to that for the Audi coil. We thus did the same analysis for NRP discharges.

Figure 5.24 shows the flame speed as a function of stretch rate for these two cases. In Figure 5.24, the unstretched flame speed S_b^0 (relative to the burned gas) is found to be 1.4 m/s. The expansion factor for the propane/air mixture at 2 bar is about 6.7. Thus the laminar burning velocity, S_u^0 (relative to the unburned gas) is 20.9±1.0 cm/s, which is close to the value of 21.5 cm/s reported in the literature [95]. The Markstein length is found to be about 2.3±0.5 mm. A positive Markstein length indicates that the flame is stable.

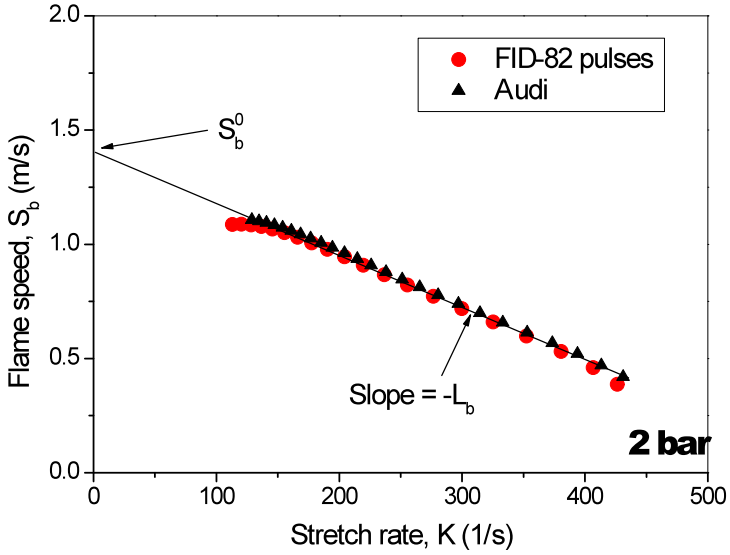

Figure 5.24 Measured flame speed as a function of stretch rate at 2 bar.

Moreover, in Figure 5.24, the linearity is better for the smooth flame ignited by the Audi coil than that for the slightly wrinkled flame ignited by NRP discharges. Nevertheless, the results are the same for both ignition systems.

The results show that our measurements are in good agreement with other data in the literature, and our experimental procedure is thus validated.

5.4 Conclusion

In this chapter, we first characterized the ignition kernel produced by NRP discharges. This consisted in measuring the initial spark radius and in characterizing the

ignition kernel development, using the schlieren technique. The effects of pressure and spark energy on the initial spark radius were studied. It was shown that the initial spark radius decreases with increasing pressure, and increases with increasing nanosecond spark energy. After breakdown by the first pulse, the development of the ignition kernel is dominated by the energy input of the subsequent discharges. The expansion of the ignition kernel slows down at high pressures.

Secondly, we studied the effects of NRP discharges on lean mixture ignition. We examined the effects on lean mixture ignition of the PRF, which is equivalent to the average power, and of the number of pulses (NoP), which is equivalent to the total energy. We showed that high PRFs and large NoPs reduce the minimum ignition energy (MIE) and the pressure delay time, but have no effect on the pressure rise time.

A comparison was then made of the equivalent flame radii obtained with FID-2 and with a conventional igniter with the same average power and total energy level. The laminar flame speeds are the same for the two ignition systems, indicating that the localized NRP discharges do not affect the intrinsic burning rates of the mixture in the chamber. We also found the interesting result that the flames ignited by NRP discharges propagate at a greater speed, especially at high pressures, due to more wrinkling of the flame surface induced by NRP discharges.

Chapter 6 Application of NRP discharges to the control of combustion dynamics

6.1 Introduction

Electrical discharges have been used for centuries in the field of combustion, mainly for ignition. In the past decade, electrical discharges, in particular nanosecond repetitively pulsed (NRP) discharges, have found other applications in reacting flows, such as combustion enhancement, with a significant improvement of the lean blow-off limit [20], and an increase of the flame propagation velocity [96]. These studies have shown a significant effect of the plasma on the flame behavior through chemical and thermal activation. Since these two mechanisms are strongly coupled, their individual contributions to the flame properties have not been clarified yet. Through experimental and numerical studies [5, 97, 98], atomic oxygen has been identified as one of the most important chemical species produced by the NRP discharges to enhance combustion. Chemical models of plasma-aided combustion have then been proposed.

In previous studies, the influence of various parameters, such as pressure, temperature, fuel, diluent, burner geometry or plasma properties, was investigated. Except for ignition studies that aimed to determine the induction time, all previous investigations, in particular flame stabilization experiments [2, 99], were made under stationary conditions only. The dynamic response of a flame to NRP discharges is therefore largely unknown; this motivates the present contribution. While it is sufficient to study stationary effects in order to assess the capability of NRP discharges to augment static stability limits, alternate applications such as combustion instability control require, in addition, an understanding of the transient processes associated with the interaction of the plasma and the flame.

Combustion instability has been a key issue for lean premixed combustion in gas turbines [60]. Instabilities generally occur when the unsteady heat release rate couples with the acoustic modes of the combustor, resulting in detrimental outcomes ranging from unacceptable noise and increased heat transfer to structural failure. This effectively results in a limited operating range [61] with drawbacks in power and efficiency. For these reasons, combustion instabilities are generally undesirable and to be avoided at all cost.

One approach to mitigate these instabilities is based on active control of the system dynamics [62, 63]. However, despite numerous successful demonstrations, the application of these methods in full-scale engines remains scarce. Restrictions in available actuator technology have been identified as one of the key issues responsible

for this [63].

NRP discharges have favorable properties with respect to combustion instability control. In addition to low power consumption and a strong effect on the flame, NRP discharges can be modulated at high frequencies because there are no mechanically moving parts. This property is also promising in terms of robustness of the actuator system. Using this type of plasma as an actuator for feedback control applications in combustion systems therefore appears to be a promising approach. However, the dynamic response of the flame to the plasma forcing needs to be understood.

In this chapter, we present a fundamental investigation of the dynamic response of a weakly turbulent premixed flame to NRP discharges. In this entire chapter, we consider a lean propane/air flame at atmospheric pressure. First, in Section 6.2, we present a characterization of the recirculation zone of the Mini-PAC burner described in Chapter 3. Then, in Section 6.3, temporal CH* images when applying the discharge are presented. We extracted the flame location from the time-resolved CH* images, and focused on the temporal evolution of the lift-off height (i.e. evolution of the flame location) of a bluff-body-stabilized flame as a function of the pulse repetition frequency and power. In Section 6.4, we present the OH-PLIF images showing the temporal evolution of the distribution of OH radicals in the inter-electrode region under the application of an NRP discharge. This is followed in Section 6.5 by an interpretation of the flame enhancement process.

6.2 Characterization of the recirculation zone of the Mini-PAC burner

As observed by previous authors [2], the recirculation zone plays an important role in the combustion behavior. The deposition of active species and radicals by the discharge into the recirculation zone can be beneficial to the flame enhancement. In this study, we adopted this configuration of generating NRP plasma in the recirculation zone behind the bluff-body, with the anode 5 mm above the grounded bluff-body, as described in Chapter 3.

The velocity field has been measured by Pilla et al. [2] using the Particle Imaging Velocimetry (PIV) technique. Figure 6.1 shows the averaged velocity field at the exit of the burner for operating conditions similar to those studied in this thesis. It is clearly shown that there is a recirculation zone extending up to about 8 mm above the bluff-body. The mean velocity in the discharge region was measured at about 1 m/s. The mean residence time of the gas molecules in the discharge region was thus about 5 ms. Note that the PIV measurements were made with a cold flow (i.e. without flame). In presence of a flame, the mean velocity in the discharge region can be higher, and the residence time of the gas molecules can be shorter, but it is expected to be of the same order of magnitude.

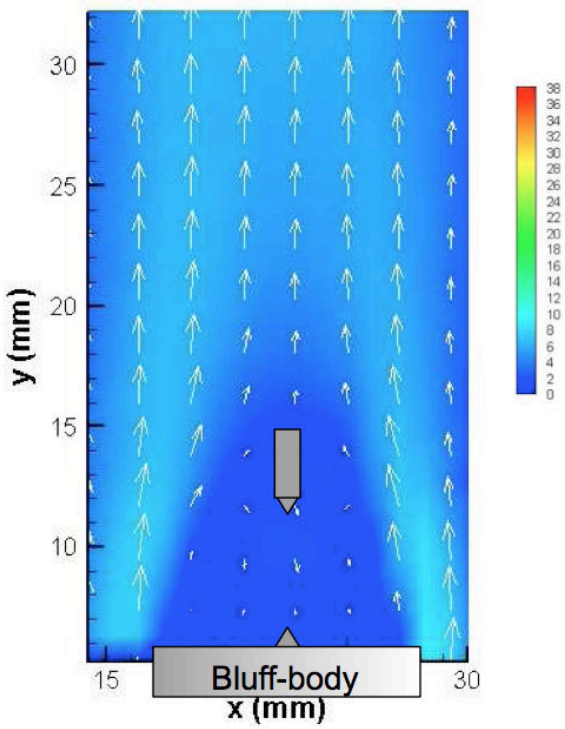

Figure 6.1 Velocity field measured by PIV at the exit of the Mini-PAC burner with an air flow rate of 3 m^3/h. Taken from [2].

6.3 Dynamic response of a weakly turbulent lean-premixed flame

6.3.1 Time-resolved images of CH* emission when applying NRP discharge

To determine the temporal response of the flame after applying NRP discharges, successive CH* images were recorded with a band pass filter (425 – 435 nm) during the first 20 ms starting from the plasma initiation. Due to the weakness of CH* emission, the images presented here were averaged over up to 500 events. To avoid the intense emission of N_2(C-B) in the spectral range of the band pass filter during a few tens of nanoseconds after each pulse, the images were recorded 1 µs after each pulse and the gate width of the intensifier (depending on the PRF of the plasma) was 2 µs shorter than the delay between two pulses. Figure 6.2 shows that the imaging zone of the camera was just above the bluff-body and included the inter-electrode region.

The spontaneous emission of CH* evidences the enhancement of combustion with NRP discharges. The lift-off height is significantly reduced so that the flame is essentially attached to the bluff body. This is apparent in Figure 6.3, where the spontaneous CH* emission is compared for five cases: (a) without plasma, (b)–(e) with plasma, 2, 4, 6, and 8 ms after applying NRP discharges. In cases (b)–(e), the average plasma power was kept constant at 12 W and the PRF at 30 kHz. We can see the temporal evolution of the flame root, moving from about 7 mm above the bluff-body down to about 1 mm.

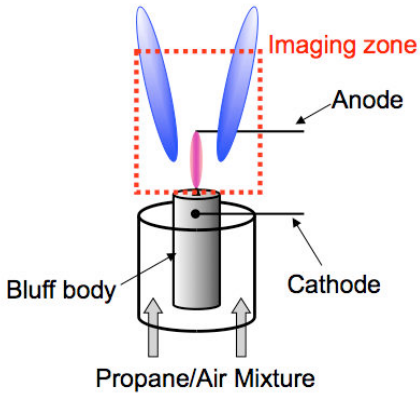

Figure 6.2 Schematic showing the imaging zone of the camera for CH* emission.

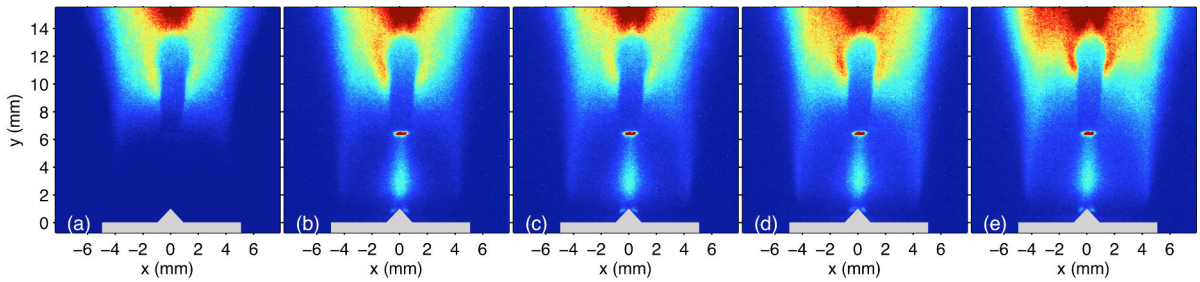

Figure 6.3 Images of spontaneous CH* emission intensity: a) without NRP discharges, (b)–(e) with plasma 2, 4, 6, and 8 ms after applying NRP discharges (12 W average power and 30 kHz PRF). These images are averaged over 500 events.

6.3.2 Characterization of the dynamic effect of the plasma

To study the influence of NRP discharges on the flame, the distance between the bluff-body and the lowest part of the reaction zone was determined. The following post-processing procedure was used to extract the flame location from the CH* images. The images were first filtered to reduce noise. A threshold of 20% of the maximum intensity of the CH* spontaneous emission was used to binarize the image (1, indicating the presence of a flame, or 0, indicating no combustion). An example is given in Figure 6.4. The distance between the bluff-body and the bottom location of the V-shaped flame on the binarized image was then measured. The distances obtained by this method were normalized by the distance from the bluff-body to the location of the flame front without plasma.

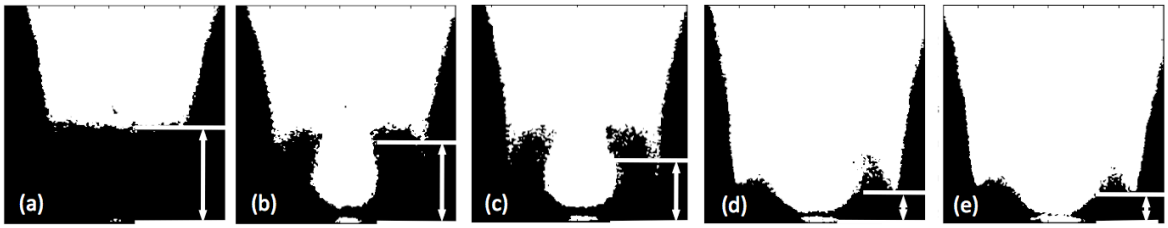

Figure 6.4 Binarized images of CH* emission corresponding to the images shown in Figure 6.3: a) without NRP discharges, (b)–(e) with plasma 2, 4, 6, and 8 ms after applying NRP discharges. The white arrows indicate the distance between the bluff-body and the bottom location of the flame.

6.3.3 Influence of the average power deposited by NRP

Keeping the PRF of the discharges constant at 30 kHz, the dynamic response of the flame was measured for 7.2, 12 and 19 W of power deposited by the discharge. Figure 6.5 shows that for 7.2 W (electric power into the plasma≈0.4% of the thermal power of the flame), NRP discharges start to have an effect on the flame. At this low power, the response lag of the flame is about 10 ms, and the distance of the flame root to the bluff-body is decreased by 20% compared to the case without plasma. When the plasma power is increased, the flame response is faster and the decrease in lift-off height more significant. For a plasma power of 19 W (1% of the thermal power of the flame), the response lag of the flame is about 4 ms and the distance between the flame root and the bluff body is decreased by 90%, i.e., the flame is almost fully attached to the bluff body (see Figure 6.3).

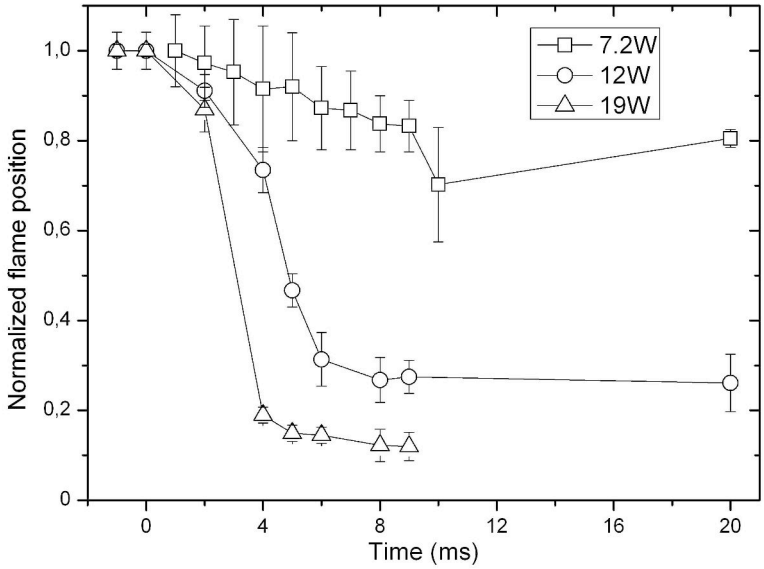

Figure 6.5 Temporal evolution of the flame position after applying NRP discharges, as a function of the electric power deposited into the plasma.

To understand the energy transfer between the NRP discharges and the combustion zone, the influence of the plasma power on the gas temperature and the $N_2(C)$ density in the inter-electrode region was studied (Figure 6.6). Time-resolved OES measurements were made for two different delays: first, during the first 2 ns of the $N_2(C\text{-}B)$ emission after initiating a pulse; second, 10 ns later. The recorded spectra were accumulated over 900,000 pulses.

The rotational temperature in the early stages of the pulse is not influenced by the discharge power and is about 2000 K. The measurements were made over the first 2 ns of the pulse. At that instant, the rotational temperature of $N_2(C)$ is not affected by the ongoing pulse and thus, this temperature corresponds to the average gas temperature in the plasma zone, resulting from the effect of the previous pulses. We found that the plasma has a noticeable thermal effect. As shown in Section 3.7.2, the gas temperature without plasma was 1500 K. The temperature increases by about 500 K when NRP

spark discharges are applied. This increase of temperature is due to not only the heating effect of the NRP discharges, but also to the heat released when the flame reattaches to the bluff-body.

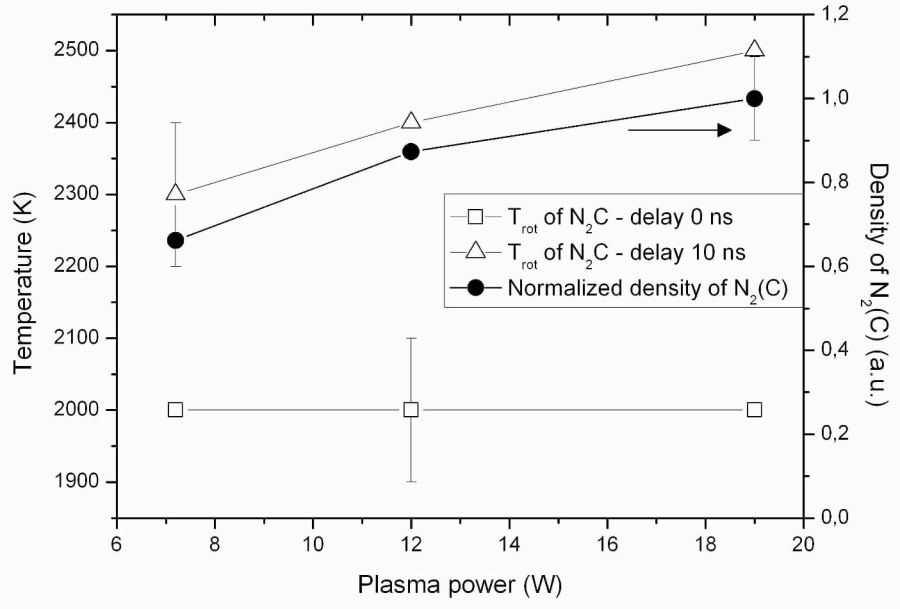

Figure 6.6 Influence of the plasma power (PRF = 30 kHz) on the temperature of the gas and maximum of $N_2(C)$ density in the inter-electrode region.

Measurements made 10 ns later show an increase of the gas temperature in the inter-electrode region varying from 300 to 500 K with the plasma power. At the same time, the maximum peak emission of the N_2(C-B) (0, 2) vibrational band was recorded (Figure 6.6). $N_2(C)$ is one of the key species in the mechanism of ultrafast atomic oxygen production [19, 29]. The peak density of $N_2(C)$ increases with the plasma power, as does the gas temperature, 10 ns after initiating the pulses. These results are consistent with the mechanism of ultrafast heating and atomic oxygen production validated for NRP discharges in air [6, 31]. According to this mechanism, molecular nitrogen is excited by electron impact during the voltage pulse. Then, the electronically excited molecular nitrogen dissociates molecular oxygen through dissociative quenching reactions, generating atomic oxygen and heat.

Thus, the combined effects of thermal and chemical, which are strongly coupled, could be responsible for the change of the flame location.

6.3.4 Influence of the repetition frequency

The dynamic response of the flame to NRP discharges was studied for PRFs of up to 80 kHz, while keeping the average plasma power constant at 12 W. Figure 6.7 shows that for PRFs of 10, 20, 30 and 50 kHz, the temporal response and the final location of the flame are always pretty much identical. In addition, the location of the flame front 20 ms after starting NRP discharges was determined for PRFs of up to 80 kHz with a constant average plasma power of 12 W (Figure 6.8). The stabilized flame location after applying NRP discharges in the recirculation zone is approximately constant for PRFs

larger than 10 kHz. This is an interesting observation if we consider the fact that the energy deposited by a plasma with an average power of 12 W decreases from 1200 µJ per pulse (10 kHz PRF) to 150 µJ per pulse (80 kHz PRF).

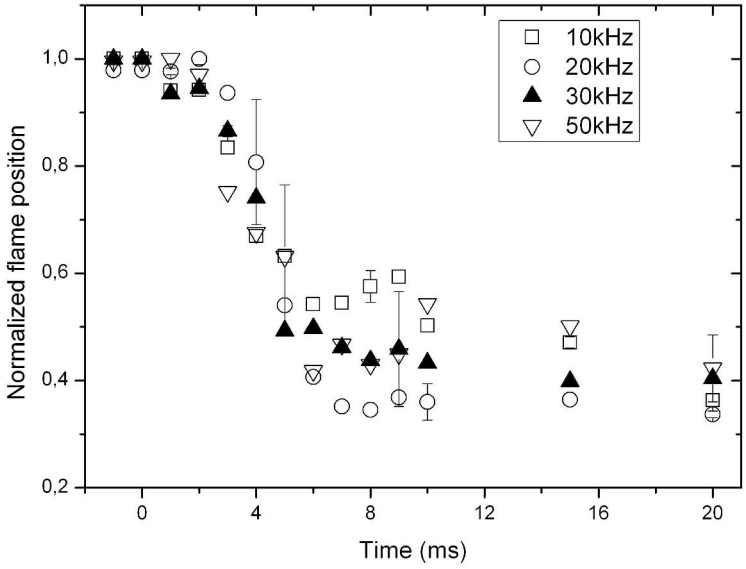

Figure 6.7 Influence of the PRF of the discharge on the temporal evolution of the flame position, for a constant average plasma power of 12 W.

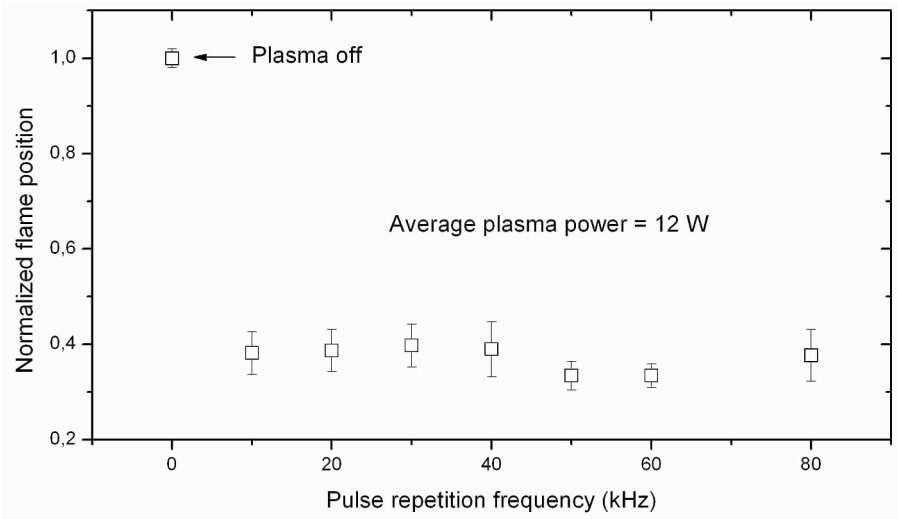

Figure 6.8 Influence of the PRF of the discharge on the flame position after 20 ms.

In this context, OES measurements were performed to determine the increase of the gas temperature induced by NRP discharges with various PRFs. Figure 6.9 presents the rotational temperature and the estimated production of $N_2(C)$ in the interelectrode region for PRFs of up to 80 kHz and an average plasma power of 12 W. The production of $N_2(C)$ was estimated based on the normalized peak emission of the $N_2(C\text{-}B)$ (0, 2) band during the pulse multiplied by the pulse repetition frequency. The temperature measurements were made for the same two delays defined previously: during the first 2 ns of the $N_2(C\text{-}B)$ emission and 10 ns later.

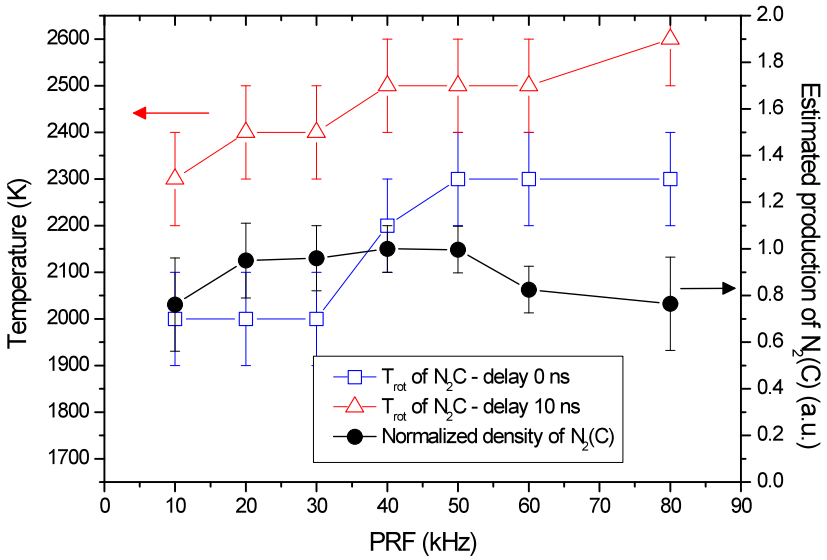

Figure 6.9 Influence of the PRF on the gas temperature and on the estimated production of $N_2(C)$ density in the inter-electrode region.

Keeping the plasma power constant, the gas temperature in the inter-electrode region increases from 2000 K at 10 kHz to 2300 K at 80 kHz, possibly due to the accumulative effect of pulses. Measurements taken 10 ns after the beginning of N_2(C-B) emission show that the gas temperature in the plasma zone increases by about 300 K for all the PRFs studied.

The production of $N_2(C)$ was estimated (Figure 6.9). It can be noted that the PRF does not have a noticeable influence on the total production of $N_2(C)$ for an average plasma power of 12 W. This means that the pulses does not have an evident accumulative effect on the production of $N_2(C)$, because of its relatively short lifetime.

These results can be summarized as follows: by increasing PRF from 10 kHz to 80 kHz while keeping constant power, the gas temperature in the plasma zone increases from 2000 to 2300 K, but the total production of active species, such as atomic oxygen or excited states of nitrogen, is constant. This suggests that in the current flame conditions and temperature range (2000-2300 K), the temperature does not influence the flame position. The thermal and chemical effects of the plasma are already known to enhance combustion, but their relative influence is still not comprehensively established [100-102]. As will be seen later, the mechanism of flame position reduction is the continuous ignition of fresh mixture by the radicals and/or heat produced by the NRP discharges, a temperature of 2000 K may be already high enough to ignite the upcoming fresh mixture. Thus, in this study, due to the high temperature range (2000-2300 K), it cannot be discriminated which effect has the most significant impact on combustion enhancement. However, we have shown that in the range of 10–80 kHz, the key parameter for flame lift-off reduction by NRP discharges is the overall plasma power.

6.4 Effect of OH radicals on the flame dynamics

We have shown in the previous section that NRP discharges have great potential in control of combustion instabilities, thanks to their ability to modify the anchoring of a lean propane-air flame behind a bluff-body, within a few milliseconds after the discharge initiation. Based on CH* imaging and spectroscopic measurements, we have explained that the lift-off-height reduction, which eventually indicates an increase in burning velocity, could be due to the production of active species or the heating of the gas by the NRP discharges. According to previous studies [2], OH radicals are key species in combustion. In order to understand the role of OH radicals in plasma-enhanced combustion, temporal evolution of the distribution of OH radicals should be obtained.

In this section, the planar laser-induced fluorescence (PLIF) technique presented in Section 3.5 is used to study the temporal and spatial development of OH concentration. Images of CH* emission are also recorded temporally to trace the location of the flame. The results are analyzed and a possible enhancement process is proposed.

6.4.1 Single-shot OH-PLIF images with and without plasma

In this study, as in previous sections, the NRP discharges were applied in the recirculation zone, downstream of the bluff-body. Figure 6.10 shows typical instantaneous images of the OH LIF signal with 50-ns integration time for the cases without (a, b) and with (c, d) plasma, among the 500 images recorded, respectively. Since OH radicals are present only in the burned gas, from the two images without plasma on the left, it is clear that the recirculation zone is partly filled with burned gases. However, we can see that due to the turbulent nature of the flow, some fresh mixture can also enter into the recirculation zone (as shown in Figure 6.10b), leading to a complex mixture of burned gas (CO_2, H_2O), air and propane.

When the plasma is on (Figure 6.10c-d), the OH fluorescence signal increases in the inter-electrode region and in the lower part of the recirculation zone. The fresh mixture cannot any longer penetrate deeply into the recirculation zone (see the image with the deepest penetration among the 500 images recorded, shown in Figure 6.10d). Thus, we can note that applying NRP discharges in the burned gases can significantly change the spatial location of a lean premixed flame stabilized over a bluff-body. Based on the streamline topology measured by Pilla et al.[2], we can assume that the OH produced in the inter-electrode region is entrained toward the bluff-body, hence the observed OH distribution.

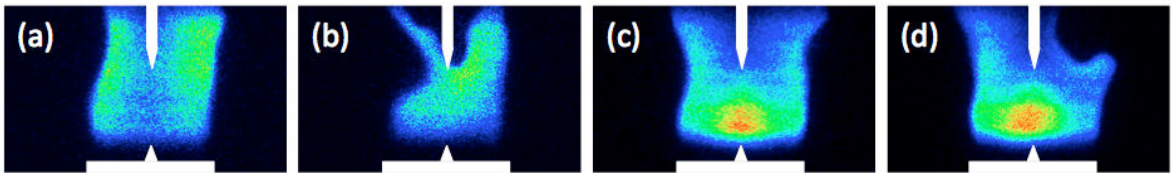

Figure 6.10 Single-shot OH PLIF images without (a, b) and with (c, d) NRP discharges with a power of 12 W and a PRF of 30 kHz, 10 ms after starting the plasma pulses (integration time 50 ns).

6.4.2 Time-resolved images of OH-PLIF after applying plasma

Since the average time-phased PLIF and CH* images are symmetrical, we are showing composed images for easier comparison. In this part, the left pane of each image shows the OH-PLIF signal and the right pane shows the CH* signal. As illustrated in Figure 6.11, the signals have been subtracted by the signals at 0 ms (which correspond to the CH* chemiluminescence and OH-PLIF signals of the flame without plasma) to show the relative concentration change. In each OH-PLIF image, the area outside the laser sheet generating OH-PLIF is blackened. After such treatment, the successive PLIF and CH* images are presented in Figure 6.12.

It can be seen from Figure 6.12 that the OH radicals are produced rapidly after the pulse initiation in the NRP discharge region, and are advected towards the bluff-body outer edge, via entrainment by the recirculating flow. According to the results of previous cold PIV studies presented in Section 6.2, the corresponding recirculation flow velocity is estimated to be about 1 m/s, which indicates that the time scale for OH radicals to reach the outer edge of the bluff-body, where the shear layer is located, is about 5 ms. The actual time scale for OH radicals to reach the shear layer is about 3 ms according to Figure 6.12. This is in reasonable agreement with the estimated 5 ms when we consider that recirculation flow velocity may have been underestimated since the PIV measurements were made in a cold flow. After reaching the bluff-body outer edge, the OH radicals are mixed with the fresh gas mixture and they go upward with the mixture. From the CH* images, it can be seen that at 4 ms the CH* emission signals are higher in the region where the OH radicals are in contact with the fresh gas mixture. Later on, this luminous zone extends upward along the shear layer and finally connects with the upper flame region. Since the CH* emission is directly related to the flame heat release rate, it can be considered as an indicator of flame enhancement.

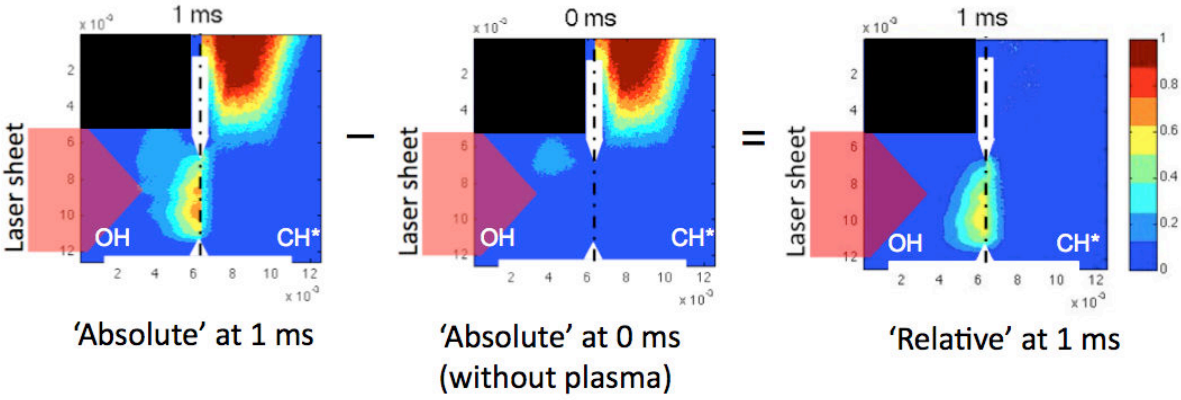

Figure 6.11 Illustration of the image treatment. For each image, OH-PLIF is shown on the left and CH* signal is shown on the left. The electrodes and the bluff-body are shown in white. The laser sheet location and width are indicated. The black area indicates the region outside of the laser sheet, where no OH-PLIF signal was measured.

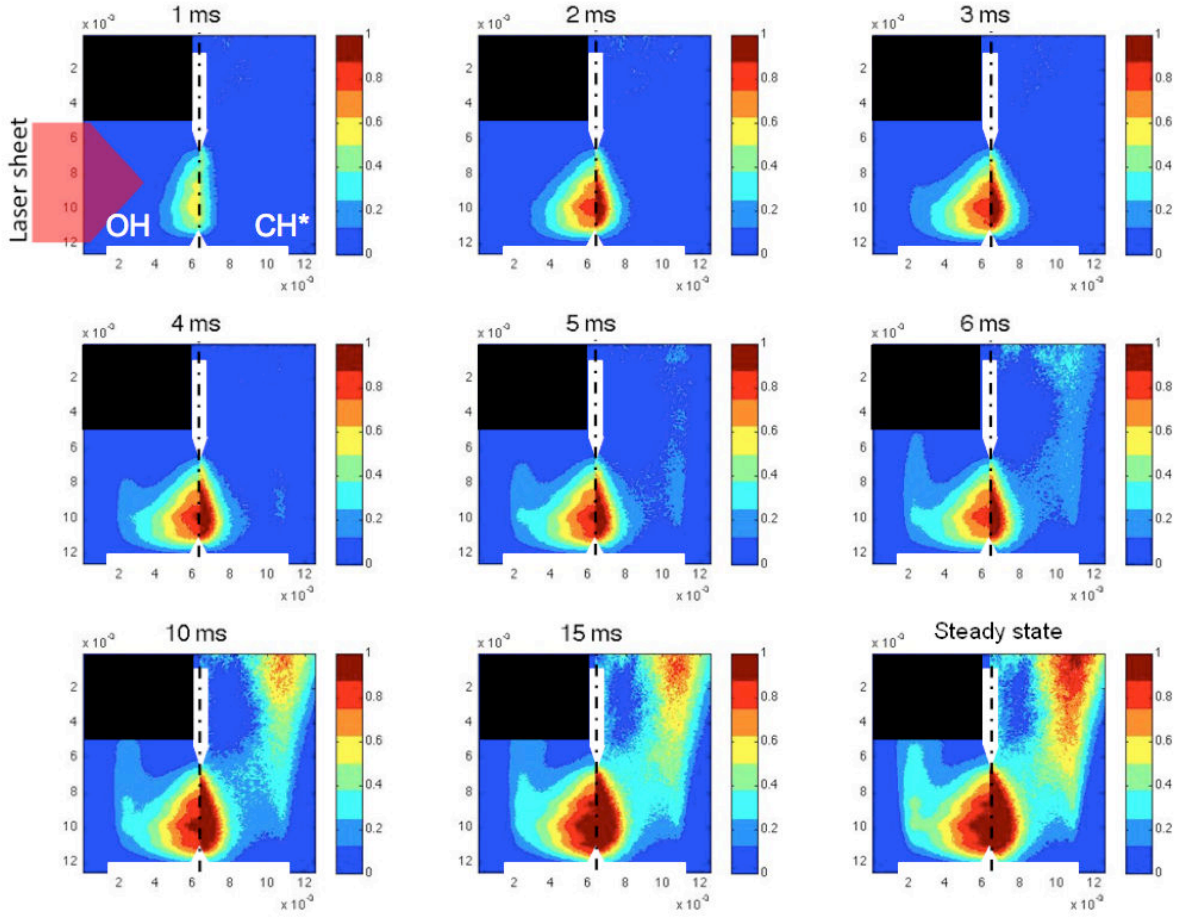

Figure 6.12 Image contours of normalized relative OH-PLIF (left) and normalized relative CH* signals (right) on each side of the centerline. All images presented here have been treated in the way demonstrated in Figure 6.11. The time above each image represents the elapsed time after discharge initiation.

The CH* emission in the discharge region is also observed. In Section 3.7.2, we have shown that the temperature in the recirculation zone without plasma was measured to be about 1500 K, whereas the adiabatic flame temperature for a propane-air mixture with an equivalence ratio of 0.8 is 2025 K. It was seen also from single-shot spontaneous OH-PLIF images (Figure 6.10) in the recirculation zone that due to the turbulent nature of the flow, some fresh gases could enter into the recirculation zone, where they mix with the burned gas. This explains that the temperature in the recirculation zone is lower than the adiabatic flame temperature and CH* can be observed in this zone probably due to propane decomposition [103] by the discharges.

Evolution of total OH radicals at the bottom of the recirculation zone

The total increase of the OH-PLIF signal after discharge initiation relative to the OH-PLIF signal of the flame without plasma is shown in Figure 6.13. Also shown in this graph is the electric energy per pulse determined from the voltage and current waveforms. It can be seen from the energy-per-pulse evolution that about 50 pulses (1.6 ms) are needed for the NRP discharges to achieve a nearly stabilized regime. The OH concentration increases as a function of time, as the OH radicals produced by the discharges advect towards the outer edge of the bluff-body. In the first 1.6 ms, the OH production increases more rapidly than afterwards, due to the rapid increase of pulse energy in the same time period. After 50 pulses (1.6 ms), it changes in slope when OH column diameter becomes wider than laser sheet.

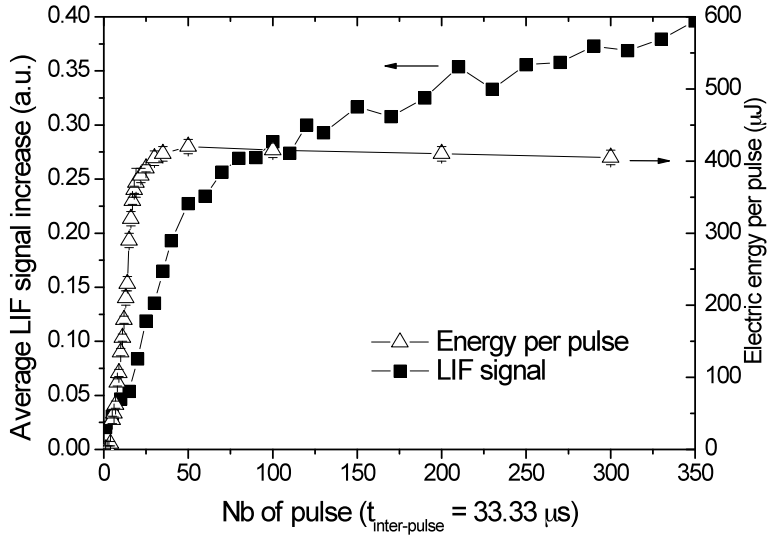

Figure 6.13 Evolution of the OH-PLIF signal increase relative to the OH-PLIF signal of the flame in the case without plasma, and evolution of electric energy per pulse.

Evolution of OH radicals in the shear layer

According to other numerous studies [104-106], the shear layer for such bluff-body stabilized premixed flames is crucial for flame ignition/extinction. The shear

layer is defined as the hydrodynamically active zone where the recirculation flow and the fresh mixture are in contact (see Figure 6.14). Chaudhuri et al. [107] found that when approaching the blow-off limit, the flame shifts into the shear layer region. Near blow-off, local flame extinction occurs along the shear layers. The flame kernel within the recirculation zone can reignite the shear layer, leading then to re-ignition of the flame. Otherwise, the flame kernel fails to reignite, and blow-off occurs.

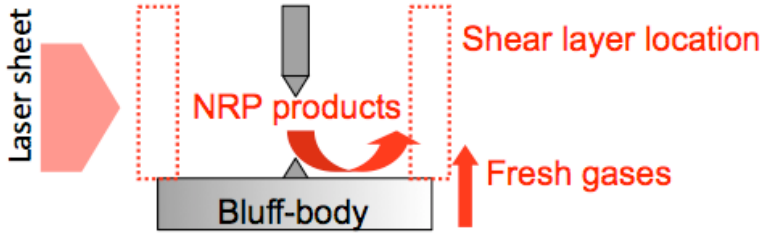

Figure 6.14 Schematics of the shear layer location

Figure 6.15 shows the OH fluorescence and CH* emission profiles at the radial location corresponding to the bluff-body outer edge (i.e. location of the shear layer) at times 3, 6 and 15 ms after discharge initiation. It can be seen that the OH radicals accumulate in the bottom part of the shear layer prior to the reactivation of the flame. As the OH concentration continues to increase, the enhancement of the flame in the shear layer is seen firstly in the bottom part where the OH radicals enter in contact with the fresh mixture, and then this high CH* concentration zone quickly extends upwards. At 15 ms, the increase of CH* signal at 12 mm above the bluff-body is about 3 times higher than that at 3 mm above the bluff-body.

These observed phenomena show that the key mechanism of flame enhancement by NRP discharges in our setup is the continuous ignition of the fresh combustible mixture in the shear layer. The physical processes anchoring a premixed flame behind a bluff-body are the mixing of the hot combustion products in the recirculation zone with the fresh mixture in the shear layer. When the contact time exceeds the chemical ignition time, the ignition of the fresh mixture occurs [104]. After applying the NRP discharges, active species, notably OH radicals, are produced in the inter-electrode region and are advected by both the expansion of the plasma zone [78] and the recirculation flow [2] to the shear layer above the bluff-body edge, where they are mixed up with the incoming fresh combustible mixture. The fresh combustible mixture is ignited almost immediately after being in contact with those active species and then the entire flame is enhanced. An alternate view is that the chemical ignition time for the fresh mixture in the shear layer can be reduced in the presence of active species produced by NRP discharges.

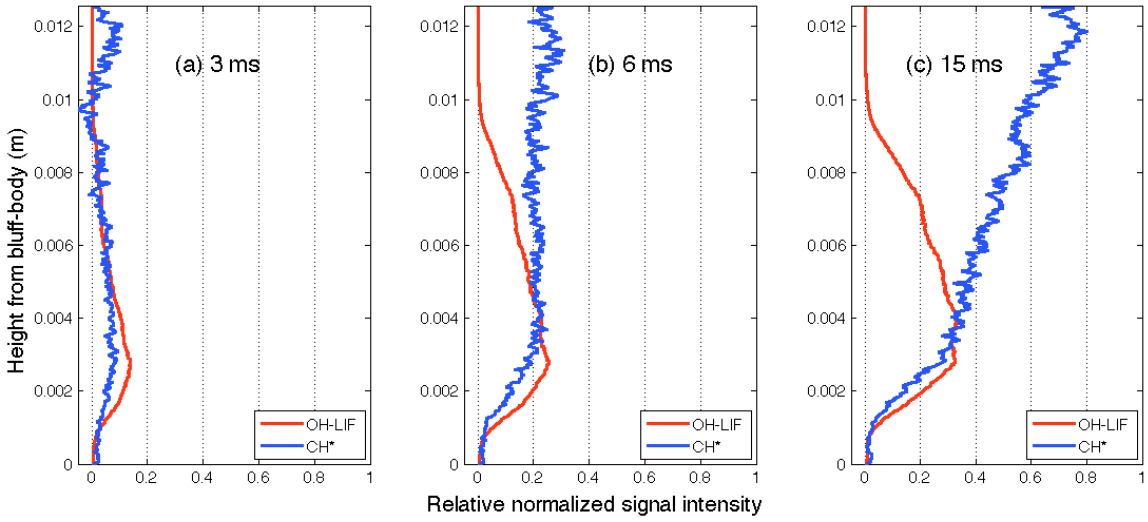

Figure 6.15 OH-PLIF and CH* profiles at radial location of bluff-body edge (i.e. central location of shear layers).

6.5 Interpretation of the flame enhancement process

In this experimental work we identified that applying NRP discharges in the recirculation zone downstream of a bluff-body can reattach a lifted flame. We have determined that NRP discharges heat the gas in the interelectrode region (by about 500 K for a discharge power of 12 W), and produce excited electronic states of N_2, which can be directly correlated with the production of atomic oxygen through the mechanism of dissociative quenching of O_2 by excited N_2. We have also shown by PLIF measurements that NRP discharges increase the OH density in the lower part of the recirculation zone. Thus, the reduction in lift-off height can be explained as follows.

During the electrical pulse, various chemical mechanisms could be involved, for example direct electron-impact dissociation or the two-step mechanism [29, 31, 68]. During this time, the volume of the discharge can be considered constant and, due to dissociation and heating of the gas, the pressure inside the plasma channel increases.

The next step, which is detailed in Chapter 4, is an expansion of the hot gases during the first µs after the pulse until they reach atmospheric pressure. The heated channel radius doubles in radius at the end of this process. This expansion starts to transport the chemical products of the plasma towards the flame. Next, these species are advected by the flow over the bluff body, i.e. to the domain where the flame is expected to be stabilized, with an average radial velocity of about 1 m/s [2]. This brings active species from the inter-electrode region to the combustion zone. We can therefore estimate that the time to cross the 5-mm radius of the bluff body should be about 4 ms, which corresponds to the fastest temporal response of the flame we observed in the present work.

Considering the lifetime of O atoms, which was determined to be about 25 µs by Two-photon Absorption Laser-Induced Fluorescence (TALIF) in air [6], atomic oxygen cannot be directly responsible for chemical enhancement of the flame. But the oxygen

atoms can produce longer-lived species such as OH via reactions such as:

$C_3H_8 + O \rightarrow C_3H_7 + OH$

$H_2O + O \rightarrow 2\ OH$

OH radicals are known for their beneficial effects for flame enhancement [5, 7, 56]. Thus, the OH radicals produced in this manner are likely one of the key species responsible for the observed flame enhancement effects in the present experiments.

In conclusion, we have shown that active species, notably OH radicals produced in the inter-electrode region are produced by the discharge and are advected by both the expansion of the plasma zone [78] and the recirculation flow [2] to the shear layer above the bluff-body edge, where they mix with the incoming fresh combustible mixture. The fresh combustible mixture is ignited almost immediately after being in contact with those active species and then the entire flame is enhanced.

6.6 Conclusion

In this chapter, we first investigated the temporal response of a weakly turbulent, bluff-body stabilized, lean-premixed flame subjected to NRP. CH* emission images were used to determine the reduction in lift-off height induced by the plasma. The N_2(C-B) (0, 2) band peak emission was measured by OES. The temperature of the gas in the discharge region was inferred by comparing simulations and measured spectra of N_2(C-B). The temporal and spatial development of OH concentration was investigated to determine the role of OH radicals in the enhancement of the flame. The temporal CH* emission images are also recorded to indicate the heat release rate of the flame.

We found that NRP discharges have a significant influence on the anchoring of a lean propane–air flame.

The temporal response of the flame to NRP discharges was found to depend on the average power deposited by the discharge. For a plasma power of about 1% of the thermal power of the flame, the response time lag is 4 ms. Based on the explanation above, this characteristic time can be expected to be strongly dependent on the burner geometry and the flow field.

For a constant average power of the NRP discharges, the response of the flame is independent of the PRF. Temperature and N_2(C) density measurements have shown that the discharges have both a thermal and a chemical effect, but that in the current study we could not identify which effect has the most significant impact.

The results also show that the key mechanism of the reduction of flame lift-off height by NRP discharges is the continuous ignition of the fresh combustible mixture in the shear layer at a more upstream zone, so that the lifted flame appears to be re-attached to the bluff-body. It is shown that active species, notably OH radicals produced by NRP discharges, are advected by the recirculation flow to the shear layer above the bluff-body edge, where they mix with the upcoming fresh combustible mixture. The fresh combustible mixture is continuously ignited almost immediately

after being in contact with these active species and the entire flame is enhanced

The results indicate that NRP discharges are well suited for applications in combustion instability control. As we have shown, it is possible to affect the flame dynamically, and this can be used to counteract the oscillations induced by acoustic perturbations. Preliminary experiments have been conducted that confirm this expected effect [108]. In [108], the effect of NRP discharges on combustion oscillations in a swirl-stabilized combustor was investigated. It was shown that a significant reduction of the oscillation amplitude can be obtained under NRP discharges' actuation. Nevertheless, additional experiments will be necessary to confirm these results for higher Reynolds number flow and high-pressure combustion, conditions generally encountered in real gas turbines or aero engines. Indeed, processes of flame stabilization can be different depending on the type of burner and the operating conditions.

Chapter 7 Conclusion

7.1 Contributions of this thesis

In this thesis, we quantified the thermal and hydrodynamic effects of NRP discharges in air. We also applied NRP discharges to lean mixture ignition and lean flame actuation.

Our findings are summarized as follows:

Thermal and hydrodynamic effects of NRP discharges

Following the NRP spark, the heat release from the dissociative quenching of electronic states of N_2 by molecular oxygen forms a heated gas channel. Hydrodynamic expansion is then caused by the fast pressure rise that accompanies the fast temperature increase in the heated channel. Because of this pressure increase, pressure waves emerge from the heated channel and propagate through the surrounding air.

At 300 K, the heated gas channel grows from an initial radius of about 0.2 mm at 50 ns and increases to about 0.4 mm at 1 μs. It finally dissipates into the surrounding air. The shock wave emerges from the heated gas channel at a later time, between 0.5-0.75 μs, due to the inertia of air. At about 3 μs, its shape changes from a cylindrical to a spherical wave of radius comparable to the gap distance. In air preheated at 1000 K, similar phenomena are observed, except that the initial radius of the heated channel is greater. The shock-wave propagation speed is also greater at high temperature.

Using a comparison of the contrast profiles obtained from experimental and numerical schlieren images, we determined the initial gas temperature and the fraction of energy transferred into fast gas heating. Additional basic parameters, i.e. the density, temperature and pressure evolutions following an NRP discharge, can then be calculated.

It was found that the fraction of energy transferred into ultrafast heating strongly depends on the E/N value. At high E/N values (270 Td), 75±25% of the energy is transferred into heating in 50 ns. At lower E/N values (164 Td), this fraction is about 25±10%.

Before each pulse, the gas temperature in the gap increased due to heating by the previous pulses. This increase is proportional to the average power per unit volume deposited by the discharges, and varies from 100 to 1000 K in the cases studied. In NRP discharges, heating by previous pulses must be carefully accounted for because it leads to an increased value of E/N, which in turn produces high heating and oxygen dissociation through dissociative quenching within a few 100 ns. It is this synergy effect that distinguishes NRP discharges from single nanosecond discharges. In the cases we

reported, over the range 164 to 270 Td, the measured and predicted temperature produced by the ultrafast heating mechanism varied from 500 to 4000 K in a channel of about 1-2 mm diameter.

The present measurements thus provide a quantification of the thermal and hydrodynamic effects of nanosecond repetitively pulsed discharges in air. In particular, they confirm the measured ultrafast temperature increase that was observed by emission spectroscopy of the first and second positive spectra of nitrogen [29]. They also provide a significant improvement over previous methods to quantitatively measure the initial temperature and the fraction of energy deposition into heating.

Ignition by NRP discharges

A train of NRP discharges was used to ignite a lean propane/air mixture of equivalence ratio 0.7 and pressure up to 10 bar.

We studied the initial spark radius of NRP discharges. It was shown that the initial spark radius decreases with increasing pressure, and increases with increasing nanosecond spark energy. After breakdown by the first pulse, the development of the ignition kernel is dominated by the energy input of the subsequent discharges. The expansion of the ignition kernel slows down at high pressures.

Regarding the ignition efficiency, we showed through parametric studies that high Pulse Repetition Frequencies (PRF) and high Number of Pulses (NoP) reduce the minimum ignition energy (MIE) and the pressure delay time, but have no effect on the pressure rise time. The effect of the PRF can be explained by the synergy of multiples pulses: when the discharge is fired in a channel heated by previous pulses, the gas density is lower and the resulting higher E/N produces higher heating and oxygen dissociation through dissociative quenching.

In terms of flame propagation speed, a comparison was made of the equivalent flame radii obtained with NRP discharges and with a conventional igniter with the same average power and total energy level. The laminar flame speeds were measured to be the same for the two ignition systems, indicating that the localized NRP discharges do not affect the intrinsic burning rate of the mixture in the chamber. We also found the interesting result that the flames ignited by NRP discharges propagate at a greater speed, especially at high pressures, due to increased wrinkling of the flame surface induced by NRP discharges.

Combustion dynamic control by NRP discharges

NRP discharges have a significant influence on the anchoring of a lean propane–air flame stabilized on a bluff-body. For our experimental conditions, the flame lift-off height decreased by 90% in less than 5 ms after the discharge initiation.

The temporal response of the flame to NRP discharges was found to depend on the average power deposited by the discharge. For a plasma power of about 1% of the thermal power of the flame, the response time lag was 4 ms. This characteristic time

can be expected to be strongly dependent on the burner geometry and the flow field.

For a given average power of the NRP discharges, the response of the flame is independent of the PRF. Temperature and $N_2(C)$ density measurements have shown that the discharges have both a thermal and a chemical effect. In the current study we could not identify which effect has the most significant impact.

It was shown that active species, notably OH radicals produced by NRP discharges likely through the oxidation of fuel radicals by O atoms, are advected by the recirculation flow present behind the bluff-body to the shear layer above the bluff-body edge, where they mix with the incoming fresh combustible mixture. The fresh combustible mixture is continuously ignited almost immediately after being in contact with these active species and the entire flame is enhanced. Thus, the present work showed that the key mechanism of the reduction of flame lift-off height by NRP discharges is the continuous ignition of the fresh combustible mixture in the shear layer at a more upstream zone, which induces a re-attachment of the lifted flame to the bluff-body.

7.2 Perspectives and future work

Thermal and hydrodynamic effects of NRP discharges

The quantitative schlieren images could be improved by modifying the experimental procedure. Indeed, in the current quantitative schlieren configuration, the accuracy largely depends on the quality of the calibration. This calibration could be greatly improved by using a spatially static, temporally stable light source (e.g. a powerful white LED).

The model could also be improved, for example by taking into account the dissociation of nitrogen, which not only changes the kinetics, but also influences the Gladstone-Dale coefficient which is smaller for N_2 than for N (by a factor of 0.78). Taking into account chemical kinetics is also recommended.

Ignition by NRP discharges

In the NRP ignition experiments, we obtained global parameters, i.e. flame kernel development, MIE, and pressure evolution. For detailed comparisons with kinetic simulations, it would be desirable to also determine the temperature and the absolute densities of active species such as atomic oxygen or OH. This would provide important information about the evolution of these quantities both during and after a train of NRP discharges.

The present work was performed in quiescent environment. It would be important to quantify the effects of the flow field, because there is always the presence of an aerodynamic flow field in real engine conditions.

Kinetic simulations are a key way to understand the plasma-assisted ignition mechanisms. Kinetics coupled with multi-dimensional fluid dynamics would be of great

interest to identify the key enhancing mechanisms of NRP discharges, which can be of chemical, thermal or hydrodynamic nature.

Finally, the application of NRP discharges in real engine conditions would be desirable to estimate the extent to which NRP discharges improve the combustion process.

Combustion dynamic control by NRP discharges

Since the control of combustion dynamics depend on the type of burner and operating conditions, the next step will be to confirm these results for higher Reynolds number flow and high-pressure combustion.

In order to understand the actuation mechanisms in the current configuration, measurements of the temperature and absolute densities of key species such as O and OH, in the recirculation zone must be obtained, although it seems complicated. Other simple experimental configurations could be considered in the future in order to separate the thermal and hydrodynamic effects from chemical activation, for instance, using a DBD configuration, which produces limited heat.

References

[1] Lefebvre A H 1999 *Gas turbine combustion* (Taylor and Francis)

[2] Pilla G 2008 Etude experimentale de la stablisation de flammes propane-air de premelange par decharges nanosecondes impulsionnelles repetitives (Ph.D. thesis, Ecole Centrale Paris, France)

[3] Pancheshnyi S, Lacoste D A, Bourdon A and Laux C O 2006 Ignition of propane-air mixture by a repetitively pulsed nanosecond discharge *IEEE Trans. Plasma Sci.* **34** 2478-87

[4] Williams S, Midey A J, Arnold S T, Miller T, Bench P M, Dressler R A, Chiu Y H, Levandier D J, Viggiano A A, Morris R A, Berman M R, Maurice L Q and Carter C D 2001 Progress on the investigation of the effects of ionization on hydrocarbon/air combustion chemistry - kinetics and thermodynamics of c6-c10 hydrocarbon ions *AIAA Paper 2001-2873, 32nd AIAA Plasmadynamics and Lasers Conference and 4th Weekly Ionized Gases Workshop,* (Anaheim, CA)

[5] Ombrello T, Won S H, Ju Y and Williams S 2010 Flame propagation enhancement by plasma excitation of oxygen *Combustion and Flame* **157** 1906-28

[6] Stancu G D, Kaddouri F, Lacoste D A and Laux C O 2010 Atmospheric pressure plasma diagnostics by oes, crds and talif *Journal of Physics D: Applied Physics* **43**

[7] Sun W T, Uddi M, Won S H, Ombrello T, Carter C and Ju Y G 2012 Kinetic effects of non-equilibrium plasma-assisted methane oxidation on diffusion flame extinction limits *Combustion and Flame* **159** 221-9

[8] Uddi M, Jiang N B, Mintusov E, Adamovich I K and Lempert W R 2009 Atomic oxygen measurements in air and air/fuel nano second-pulse. Discharges by two photon laser induced fluorescence *Proceedings of the Combustion Institute* **32** 929-36

[9] Maly R and Vogel M Initiation and propagation of flame fronts in lean ch4-air mixtures by the three modes of the ignition spark *Symposium (International) on Combustion* **17** 821-31

[10] Ziegler G, Wagner E and Maly R 1985 Ignition of lean methane-air mixtures by high pressure glow and arc discharges *Symposium (International) on Combustion* **20** 1817-24

[11] Modien R, Checkel M and Dale J 1991 The effect of enhanced ignition systems on early flame development in quiescent and turbulent conditions *SAE Technical Paper 910564*

[12] Starikovskiy A and Aleksandrov N 2013 Plasma-assisted ignition and combustion *Prog Energ Combust* **39** 61-110

[13] Machala Z, Pai D Z, Janda M and Laux C O 2014 *Atmospheric pressure nanosecond pulsed discharge plasmas in Low temperature plasma technology: Methods and applications,* ed P Chu and X Lu (New York: Tayler&Francis Group)

[14] Aleksandrov N L, Vysikailo F I, Islamov R S, Kochetov I V, Napartovich A P and Pevgov V G 1981 Electron-distribution function in 4-1 n-2-o-2 mixture *High Temperature (Teplofizika Vysokikh Temperatur)* **19** 17-21

[15] Nighan W L 1970 Electron energy distributions and collision rates in electrically excited n2, co, and co2 *Phys Rev A* **2** 1989-2000

[16] Macheret S, Shneider M and Miles R 2005 Energy efficiency of plasma-assisted combustion in ram/scramjet engines *AIAA 2005-5371, 36th AIAA Plasmadynamics and Lasers Conference* (Toronto, Ontario, Canada)

[17] Pai D Z, Lacoste D A and Laux C O 2010 Transitions between corona, glow,

and spark regimes of nanosecond repetitively pulsed discharges in air at atmospheric pressure *Journal of Applied Physics* **107**

[18] Pai D 2008 Nanosecond repetitively pulsed plasmas in preheated air at atmospheric pressure (Ph.D. thesis, Ecole Centrale Paris, France)

[19] Rusterholtz D L 2012 Nanosecond repetitively pulsed discharges in atmospheric pressure air (Ph.D. thesis, Ecole Centrale Paris, France)

[20] Starikovskaia S M 2006 Plasma assisted ignition and combustion *J Phys D Appl Phys* **39** R265-R99

[21] Pai D Z 2011 Nanomaterials synthesis at atmospheric pressure using nanosecond discharges *J. Phys. D: Appl. Phys.* **44**

[22] Wang D, Namihira T and Akiyama H 2010 *Pulsed discharge plasma for pollution control in Air pollution,* ed V Villanyi (Online: Sciyo)

[23] Beebe S and Schoenbach K 2005 Nanosecond pulsed electric fields: A new stimulus to activate intracellular signaling *J. Biomed. Biotechnol.* **2005** 297-300

[24] Vernier P T, Sun Y H, Marcu L, Salemi S, Craft C M and Gundersen M A 2003 Calcium bursts induced by nanosecond electric pulses *Biochem Bioph Res Co* **310** 286-95

[25] Adamovich I V, Choi I, Jiang N, Kim J H, Keshav S, Lempert W R, Mintusov E, Nishihara M, Samimy M and Uddi M 2009 Plasma assisted ignition and high-speed flow control: Non thermal and thermal effects *Plasma Sources Science and Technology* **18**

[26] Korolev Y D and Mesyats G A 1998 *Physics pulsed breakdown in gases* (URO Press)

[27] Naidis G V 2008 Simulation of spark discharges in high-pressure air sustained by repetitive high-voltage nanosecond pulses *J Phys D Appl Phys* **41**

[28] Tholin F 2012 Numerical simulaiton of nanosecond repetitively pulsed discharges in air at atmospheric pressure: Application to plasma assisted combustion (Ph.D. thesis, Ecole Centrale Paris, France)

[29] Rusterholtz D L, Lacoste D A, Stancu G D, Pai D Z and Laux C O 2013 Ultrafast heating and oxygen dissociation in atmospheric pressure air by nanosecond repetitively pulsed discharges *J. Phys. D: Appl. Phys.* **46** 464010

[30] Popov N A 2013 Fast gas heating initiated by pulsed nanosecond discharge in atmospheric pressure air *AIAA 2013-1052, 51st AIAA Aerospace Sciences Meeting* (Grapevine TX)

[31] Popov N A 2001 Investigation of the mechanism for rapid heating of nitrogen and air in gas discharges *Plasma Phys. Rep.* **27** 886-96

[32]Lo A, Cleon G, Vervisch P and Cessou A 2012 Spontaneous raman scattering: A useful tool for investigating the afterglow of nanosecond scale discharges in air *Appl Phys B-Lasers O* **107** 229-42

[33] Aleksandrov N, Kindysheva S, Nudnova M and Starikovskiy A 2010 Mechanism of ultra-fast heating in a non-equilibrium weakly ionized air discharge plasma in high electric fields *J. Phys. D: Appl. Phys.* **43**

[34] Haley R and Smy P 1989 Electrically induced turbulence - the short duration spark. 22: 258-265 *Journal of Physics D: Applied Physics* **22** 258-65

[35] Kono M, Niu K, Tsukamoto T and Ujiie Y 1989 Mechanism of flame kernel formation produced by short duration sparks *Symposium (International) on Combustion* **22** 1643-9

[36] Ko Y, Anderson R and Arpaci V 1991 Spark ignition of propane-air mixtures near the minimum ignition energy: Part i. An experimental study *Combustion and*

Flame **83** 75-87

[37] Lim M, Anderson R and Arpaci V 1987 Prediction of spark kernel development in constant volume combustion *Combustion and Flame* **69** 303-16

[38] Freeman R and Craggs J 1969 Shock waves from spark discharges *Journal of Physics. D: Applied. Physics* **2** 421-7

[39] Reinmann R and Akram M 1997 Temporal investigation of a fast spark discharge in chemically inert gases *Journal of Physics. D: Applied Physics* **30**

[40] Sedov L 1959 *Similarity and dimensional methods in mechanics* (Infosearch Ltd.)

[41] Zel'dovich Y and Raizer Y 2002 *Physics of shock waves and high-temperature hydrodynamic phenomena* (Dover Publications Inc.)

[42] Arpaci V S, Ko Y, Lim M T and Lee H S 2003 Spark kernel development in constant volume combustion *Combustion and Flame* **135** 315-22

[43] Kogelschatz U and Schneider W R 1972 Quantitative schlieren techniques applied to high current arc investigations *Appl. Optics* **11** 1882-32

[44] Ono R and Oda T 2004 Visualization of streamer channels and shock waves generated by positive pulsed corona discharge using laser schlieren method *Jpn J Appl Phys 1* **43** 321-7

[45] Decker G, Deutsch R, Kies W and Rybach J 1985 Computer-simulated schlieren optics *Applied Optics* **24** 823-8

[46] Noll R, Haas C R, Weikl B and Herziger G 1986 Computer-simulation of schlieren images of rotationally symmetrical plasma systems - a simple method *Applied Optics* **25** 769-74

[47] Turnbull S M, Macgregor S J, Tuema F A and Farish O 1993 A quantitative laser schlieren method for measurement of neutral gas-density in high-pressure gas switches *Meas Sci Technol* **4** 1154-9

[48] Tajalli H, Lamb D W and Woolsey G A 1989 Energy-transfer in positive streamers *J Phys D Appl Phys* **22** 1497-503

[49] Cuenot B 2013 Advanced simulation of combustion phenomena: From spark discharges to stable combustion *Invited lecture in Aerospace Thematic Workshop 2013* (Aussois, France)

[50] Westbrook C K 2000 Chemical kinetics of hydrocarbon ignition in practical combustion systems *Proceedings of the Combustion Institute* **28** 1563-77

[51] Kosarev I N, Aleksandrov N L, Kindysheva S V, Starikovskaia S M and Starikovskii A Y 2009 Kinetics of ignition of saturated hydrocarbons by nonequilibrium plasma: C(2)h(6)- to c(5)h(12)-containing mixtures *Combustion and Flame* **156** 221-33

[52] Yin Z, Adamovich I V and Lempert W R 2013 Oh radical and temperature measurements during ignition of h-2-air mixtures excited by a repetitively pulsed nanosecond discharge *Proceedings of the Combustion Institute* **34** 3249-58

[53] Leonov S B and Yarantsev D A 2007 Plasma-induced ignition and plasma-assisted combustion in high-speed flow *Plasma Sources Sci T* **16** 132-8

[54] Criner K, Cessou A, Louiche J and Vervisch P 2006 Stabilization of turbulent lifted jet flames assisted by pulsed high voltage discharge *Combustion and Flame* **144** 422-5

[55] Kim W, Do H, Mungal M G and Cappelli M A 2006 Plasma-discharge stabilization of jet diffusion flames *Ieee Transactions on Plasma Science* **34** 2545-51

[56] Pilla G, Galley D, Lacoste D A, Lacas F, Veynante D and Laux C O 2006 Stabilization of a turbulent premixed flame using a nanosecond repetitively pulsed

plasma *IEEE Trans. Plasma Sci.* **34** 2471-77

[57] Bak M S, Do H, Mungal M G and Cappelli M A 2012 Plasma-assisted stabilization of laminar premixed methane/air flames around the lean flammability limit *Combustion and Flame* **159** 3128-37

[58] Barbosa S, Pilla G, Lacoste D A, Scouflaire P, Ducruix S, Laux C O and Veynante D 2009 Influence of a repetitively pulsed plasma on the flame stability domain of a labscale gas turbine combustor *4th European Combustion Meeting* (Vienna)

[59] Heid G, Pilla G, Lecourt R, Lacoste D A and Laux C O 2009 *ISABE*

[60] Candel S 2002 Combustion dynamics and control: Progress and challenges *Proceedings of the Combustion Institute* **29** 1-28

[61] Lieuwen T C 1999 Investigation of combustion instability mechanisms in premixed gas turbinesGeorgia Institute of Technology)

[62] Mcmanus K R, Poinsot T and Candel S M 1993 A review of active control of combustion instabilities *Prog Energ Combust* **19** 1-29

[63] Dowling A P and Morgans A S 2005 Feedback control of combustion oscillations *Annu Rev Fluid Mech* **37** 151-82

[64] How to select a current monitor (Pearson Electronics, Inc.) http://www.pearsonelectronics.com/how-to-select-a-current-monitor

[65] Settles G S 2001 *Schlieren and shadowgraph techniques: Visualizing phenomena in transparent media* (Springer-Verlag)

[66] Laux C O 2002 *Radiation and nonequilibrium collisional-radiative models in Special course on physico-chemical modeling of high enthalpy and plasma flows,* ed T M D. Fletcher, S. Sharma (Rhode-Saint-Genèse, Belgium: von Karman Institute)

[67] Stritzke P, Sander I and Raether H 1977 Spatial and temporal spectroscopy of a streamer discharge in nitrogen *J. Phys. D: Appl. Phys.* **10** 2285-300

[68] Pai D Z, Lacoste D A and Laux C O 2010 Nanosecond repetitively pulsed discharges in air at atmospheric pressure - the spark regime *Plasma Sources Sci. Technol.* **19** 065015-25

[69] Rusterholtz D L, Pai D Z, Stancu G D, Lacoste D A and Laux C O 2012 Ultrafast heating in nanosecond discharges in atmospheric pressure air *AIAA 2012-0509, 50th AIAA Aerospace Sciences Meeting* (Nashville, TN)

[70] Brode H L 1955 Numerical solutions of spherical blast waves *J. Appl. Phys.* **26**

[71] Plooster M N 1970 Shock waves from line sources. Numerical solutions and experimental measurements *Phys. Fluids* **13** 2665-75

[72] Akram M 1996 The evolution of spark discharges in gases: 2. Numerical solution of one-dimensional models *J. Phys. D: Appl. Phys.* **29** 2137

[73] Shneider M N 2006 Turbulent decay of after-spark channels *Phys. Plasmas* **13**

[74] Phuoc T X 2005 An experimental and numerical study of laser-induced spark in air *Opt. Laser Eng.* **43** 113-29

[75] Park C 1989 *Nonequilibrium hypersonic aerothermodynamics* (Wiley)

[76] Messina D, Attal-Tretout B and Grisch F 2007 Study of a non-equilibrium pulsed nanosecond discharge at atmospheric pressure using coherent anti-stokes raman scattering *Proceedings of the Combustion Institute* **31** 825-32

[77] Yin Z Y, Montello A, Carter C D, Lempert W R and Adamovich I V 2013 Measurements of temperature and hydroxyl radical generation/decay in lean fuel-air mixtures excited by a repetitively pulsed nanosecond discharge *Combustion and Flame*

160 1594-608

[78] Xu D A, Lacoste D A, Rusterholtz D L, Elias P-Q, Stancu G D and Laux C O 2011 Experimental study of the hydrodynamic expansion following a nanosecond repetitively pulsed discharge in air *Appl. Phys. Lett.* **99**

[79] Morgan database 2013 http://www.lxcat.laplace.univ-tlse.fr

[80] Eisazadeh-Far K, Parsinejad F, Metghalchi H and Keck J C 2010 On flame kernel formation and propagation in premixed gases *Combustion and Flame* **157** 2211-21

[81] Chen Z, Burke M P and Ju Y G 2009 Effects of lewis number and ignition energy on the determination of laminar flame speed using propagating spherical flames *Proceedings of the Combustion Institute* **32** 1253-60

[82] Pancheshnyi S, Nudnova M and Starikovskii A 2005 Development of a cathode-directed streamer discharge in air at different pressures: Experiment and comparison with direct numerical simulation *Phys Rev E* **71**

[83] Morrow R 1988 A parameter study of streamer propagation in sf6 *Journal of Applied Physics* **63** 5171-4

[84] Guo J M and Wu C H J 1996 Streamer radius model and its assessment using two-dimensional models *Ieee Transactions on Plasma Science* **24** 1348-58

[85] Cussler E L 2009 *Diffusion: Mass transfer in fluid systems* (Cambridge University Press)

[86] Sher E, Benyaish J and Kravchik T 1992 On the birth of spark channels *Combustion and Flame* **89** 186-94

[87] Lewis B and von Elbe G 1961 *Combustion, flames and explosions of gases* (Acdemic Press)

[88] Moorhous J, Williams A and Maddison T E 1974 Investigation of minimum ignition energies of some c1 to c7 hydrocarbons *Combustion and Flame* **23** 203-13

[89] Moffett S P, Bhanderi S G, Shepherd F E and Kwon E 2007 Investigation of statistical nature of spark ignition *2007 Fall Meeting of the Western States Section of the Combustion Institute* (Sandia National Laboratories, Livermore, CA)

[90] Tse S D, Zhu D L and Law C K 2000 Morphology and burning rates of expanding spherical flames in h-2/o-2/inert mixtures up to 60 atmospheres *Proceedings of the Combustion Institute* **28** 1793-800

[91] Gu X J, Haq M Z, Lawes M and Woolley R 2000 Laminar burning velocity and markstein lengths of methane-air mixtures *Combustion and Flame* **121** 41-58

[92] Markstein G H 1964 *Nonsteady flame propagation* (Pergamon Press)

[93] Tseng L K, Ismail M A and Faeth G M 1993 Laminar burning velocities and markstein numbers of hydrocarbon/air flames *Combustion and Flame* **95** 410-26

[94] Akindele O O, Bradley D, Mak P W and Mcmahon M 1982 Spark-ignition of turbulent gases *Combustion and Flame* **47** 129-55

[95] Razus D, Oancea D, Brinzea V, Mitu M and Movileanu C 2010 Experimental and computed burning velocities of propane-air mixtures *Energ Convers Manage* **51** 2979-84

[96] Starikovskii A Y 2005 Plasma supported combustion *Proceedings of the Combustion Institute* **30** 2405-17

[97] Zuzeek Y, Bowman S, Choi I, Adamovich I V and Lempert W R 2011 Pure rotational cars studies of thermal energy release and ignition in nanosecond repetitively pulsed hydrogen-air plasmas *Proceedings of the Combustion Institute* **33** 3225-32

[98] Do H, Im S K, Cappelli M A and Mungal M G 2010 Plasma assisted flame ignition of supersonic flows over a flat wall *Combustion and Flame* **157** 2298-305

[99] Bak M S, Kim W and Cappelli M 2011 On the quenching of excited electronic states of molecular nitrogen in nanosecond pulsed discharges in atmospheric pressure air *Applied Physics Letters* **98**

[100] Singleton D, Pendleton S J and Gundersen M A 2011 The role of non-thermal transient plasma for enhanced flame ignition in c2h4-air *J Phys D Appl Phys* **44**

[101] Starikovskii A Y, Anikin N B, Kosarev I N, Mintoussov E I, Nudnova M M, Rakitin A E, Roupassov D V, Starikovskaia S M and Zhukov V P 2008 Nanosecond-pulsed discharges for plasma-assisted combustion and aerodynamics *J Propul Power* **24** 1182-97

[102] Grisch F, Grandin G A, Messina D and Attal-Tretout B 2009 Laser-based measurements of gas-phase chemistry in non-equilibrium pulsed nanosecond discharges *Cr Mecanique* **337** 504-16

[103] Oehlschlaeger M A, Davidson D F and Hanson R K 2005 High-temperature ethane and propane decomposition *Proceedings of the Combustion Institute* **30** 1119-27

[104] Zukoski E E 1954 Flame stabilization on bluff bodies at low and intermediate reynolds numbersCalifornia Institute of Technology)

[105] Williams G C, Hottel H C and Scurlock A C 1949 Flame stabilization and propagation in high velocity gas streams *Symposium on Combustion and Flame, and Explosion Phenomena, Volume 3, Issue 1, 1949, Pages 21-40* **3** 21-40

[106] Longwell J P 1953 Flame stabilization by bluff bodies and turbulent flames in ducts *Symposium (International) on Combustion* **4** 90-7

[107] Chaudhuri S, Kostka S, Renfro M W and Cetegen B M 2010 Blowoff dynamics of bluff body stabilized turbulent premixed flames *Combustion and Flame* **157** 790-802

[108] Moeck J P, Lacoste D A, Laux C O and Paschereit C O 2013 Control of combustion dynamics in a swirl-stabilized combustor with nanosecond repetitively pulsed discharges *AIAA 20132-0565, 51th AIAA Aerospace Sciences Meeting* (Grapevine, TX)